BLANK PAGE

WT-1102

This document consists of 116 pages

No. 209 of 215 copies, Series A

AD611253

Operation TEAPOT

NEVADA TEST SITE

February – May 1955

Project 1.2

SHOCK WAVE PHOTOGRAPHY

Issuance Date: May 15, 1958

HEADQUARTERS FIELD COMMAND, ARMED FORCES SPECIAL WEAPONS PROJECT
SANDIA BASE, ALBUQUERQUE, NEW MEXICO

BLANK PAGE

UNCLASSIFIED

~~CONFIDENTIAL~~

WT—1102

OPERATION TEAPOT—PROJECT 1.2

Report to the Test Director

SHOCK WAVE PHOTOGRAPHY

J. F. Moulton, Jr.
E. R. Walthall

U. S. Naval Ordnance Laboratory
White Oak, Silver Spring, Maryland

THIS REPORT HAS BEEN APPROVED FOR OPEN PUBLICATION

UNCLASSIFIED

FORMERLY RESTRICTED DATA

Handle as Restricted Data in foreign dissemination. Section 144b, Atomic Energy Act 1954.

UNCLASSIFIED

This material contains information affecting the national defense of the United States within the meaning of the espionage laws, Title 18, U.S.C., Secs. 793 and 794, the transmission or revelation of which in any manner to an unauthorized person is prohibited by law.

UNCLASSIFIED

~~CONFIDENTIAL~~

SUMMARY OF SHOT DATA, OPERATION TEAPOT

Shot	Code Name	Date	Time*	Area	Type	Latitude And Longitude of Zero Point
1	Wasp	18 February	1200	T-7-4†	762-ft Air	37° 05' 11.0856" 116° 01' 18.7366"
2	Moth	22 February	0545	T-3	300-ft Tower	37° 02' 52.2654" 116° 01' 15.6967"
3	Tesla	1 March	0530	T-9b	300-ft Tower	37° 07' 31.8737" 116° 02' 51.0077"
4	Turk	7 March	0520	T-2	500-ft Tower	37° 08' 18.6944" 116° 07' 03.1879"
5	Hornet	12 March	0520	T-3a	300-ft Tower	37° 02' 25.4043" 116° 01' 31.2674"
6	Bee	22 March	0505	T-7-1a	500-ft Tower	37° 05' 41.3880" 116° 01' 25.6474"
7	ESS	23 March	1230	T-10a	67-ft Underground	37° 10' 06.1283" 116° 02' 37.7010"
8	Apple	29 March	0455	T-4	500-ft Tower	37° 05' 43.5200" 116° 06' 09.9646"
9	Wasp'	29 March	1000	T-7-4‡	740-ft Air	37° 05' 11.0856" 116° 01' 18.7366"
10	HA	6 April	1000	T-5§	36,620-ft MSL Air	37° 01' 43.3642" 116° 03' 28.2824"
11	Post	9 April	0430	T-9c	300-ft Tower	37° 07' 19.6968" 116° 02' 03.8840"
12	MET	15 April	1115	FF	400-ft Tower	36° 47' 52.0887" 115° 56' 44.1006"
13	Apple 2	5 May	0510	T-1	500-ft Tower	36° 03' 11.1096" 116° 06' 09.4037"
14	Zucchini	15 May	0500	T-7-1a	500-ft Tower	37° 05' 41.3880" 116° 01' 25.6474"

* Approximate local time, PST prior to 24 April, PDT after 24 April.
† Actual zero point 36 feet north, 426 feet west of T-7-4.
‡ Actual zero point 94 feet north, 62 feet west of T-7-4.
§ Actual zero point 36 feet south, 397 feet west of T-5.

[redacted]

ABSTRACT

Project 1.2 was responsible for (1) determining the peak shock overpressure as a function of distance on Shot 10, the high-altitude shot; (2) studying the effects of the surface and the heating of the air near the surface on precursor formation, growth, and shock interaction for a number of yields and heights of burst over natural and artificial surfaces; and (3) ascertaining, prior to Shot 12, whether coalescence of the incident and reflected shocks could be expected to occur directly above the burst and, if so, determining the peak overpressures at given distances on that shot.

The military importance of the first two objectives is obvious. The last objective was directed toward providing basic information on shock phenomena from a tower burst in support of the drone aircraft project (Project 5.1, Damaging Loads on Aircraft in Flight) which was given major emphasis in the Military Effects Test Program. Both smoke-grid photography and direct-shock photography, techniques similar to those used on previous tests, were employed in the successful accomplishment of these major objectives.

On Shot 10, pressures of from 800 to 8 psi were determined, covering a range of from 200 to 1,100 ft from the burst. (Taken together with the overlapping data of Project 1.1, the pressure-distance curve for this shot extends from 800 psi down to 0.14 psi over a range of approximately 11,300 ft from the burst.) These data, combined with the yield results, seem to indicate that Sachs scaling techniques for pressure, distance, and time may be applied up to altitudes of the order of 40,000 ft; however, some reservations are mentioned in the text.

The AFSWP-NOL precursor-prediction criteria were found to be more reliable than other existing prediction methods. However, as a result of the information gained during Operation TEAPOT, the AFSWP-NOL criteria have been modified to take into account the different thermal absorptivities of various surfaces. It is believed by the authors that precursors will not form over a water surface, however, natural water surfaces should not be considered as "ideal" in this regard because water-loading of the blast wave along the surface can occur and can lead to nonideal values of blast parameters, such as "excessive" dynamic pressures, for example.

Further evidence was obtained which indicates that thermal layers affect the rate of growth of the thermal Mach wave at close-in distances; but in spite of this, the triple point follows a reasonably predictable (± 10 percent) course beyond the point where it would be normally expected to rise above the upper level of the thermal layer.

A modification of the theory for calculating temperatures in the thermal layer from the angle made by the precursor with the ground is

proposed in the text, but cannot yet be fully verified. Use of the theory tends to bring the calculated temperatures in closer agreement with measured values obtained by both direct and indirect methods.

Coalescence of the incident and reflected shock waves vertically above the burst was observed on Shots 4 and 12 at 2,550 ft (12 psi level) and 2,600 ft (7 psi level) from the burst points, respectively. On Shot 4, the measurements indicated that the peak pressure is enhanced slightly following coalescence. Observed pressures were approximately equivalent to those that would have been obtained from a weapon yield 1.2 times larger than that fired. The predictions desired by Project 5.1 for Shot 12 were based on this result. On Shot 12, however, no such enhancement in pressure was observed after coalescence. Some possible explanations for this behavior are presented in the text.

[redacted]

FOREWORD

This report presents the final results of one of the 56 projects comprising the Military Effects Program of Operation Teapot, which included 14 test detonations at the Nevada Test Site in 1955.

For overall Teapot military-effects information, the reader is referred to "Summary Report of the Technical Director, Military Effects Program," WT-1153, which includes the following: (1) a description of each detonation including yield, zero-point environment, type of device, ambient atmospheric conditions, etc.; (2) a discussion of project results; (3) a summary of the objectives and results of each project; and (4) a listing of project reports for the Military Effects Program.

PREFACE

Project planning at the Naval Ordnance Laboratory was completed with the assistance of G. K. Hartmann, Paul M. Fye, J. E. Ablard, W. E. Morris, J. F. Moulton, Jr., J. Petes, E. R. Walthall, and C. J. Aronson.

For administrative and logistic support the Naval Ordnance Laboratory is indebted to the Bureau of Ordnance, the Armed Forces Special Weapons Project and in particular to E. B. Doll, Technical Director, to his staff, and to Cdr. W. M. McLellon, USN, and Maj. H. T. Bingham, USAF, Director and Assistant Director of Programs 1 and 3, respectively.

Sincere appreciation is expressed to the firm of Edgerton, Germeshausen, and Grier, Inc. for obtaining the excellent motion-picture records, without which Project 1.2 could not have met its objectives successfully. Appreciation is also expressed for the development and establishment of jet aircraft smoke trails by the 4925th Test Group (Atomic) of the Special Weapons Center, Kirtland Air Force Base.

Those who served in the field operations at the Nevada Test Site were: J. F. Moulton, Jr., Project Officer; E. R. Walthall, Deputy Project Officer; C. L. Karmel, Administration and Analysis; B. M. Loring; E. G. Nacke; R. L. Varwig; J. A. Martin, A/2c USAF; and W. R. Rogers, A/2c USAF. G. S. Rielley served as supply officer at the home station and in the field.

This WT report also carries the Naval Ordnance Laboratory number NOLR 1210.

CONTENTS

[redacted]

FIGURES

[redacted]

[redacted]

BLANK PAGE

Chapter 1
INTRODUCTION

1.1 METHODS AND OBJECTIVES

Shock-wave photography, as it has come to be known in connection with atomic tests, includes two closely related techniques designed to detect and locate in space and time the various shock phenomena associated with nuclear bursts. The simpler and slightly less accurate of the two has been termed "direct shock photography" for it involves only the use of high-speed, high-resolution cameras. "Rocket-smoke-grid photography", the more-accurate technique, requires the establishment of a grid of smoke trails situated behind the burst. Shock waves which are otherwise unobservable can be detected when photographed against such a grid. Both of these techniques are described in more detail in Chapter 2.

On many previous atomic tests, shock-wave photography has produced a wealth of reliable data (References 1 through 7). These have been used to establish the standard curve of free-air pressure versus distance down to the 10 psi level for atomic weapons (Reference 6) and they provide the basis for detailed knowledge of the development and growth of the Mach shock and triple point, the precursor phenomenon, and many other blast effects of atomic bursts.

During Operation TEAPOT, Project 1.2 was called upon to employ these techniques to determine: (1) free-air peak pressure versus distance on the high-altitude shot; (2) the position of the incident and reflected shocks as a function of time vertically above the burst position on Shots 4, 8, and 12, and if coalescence occurred, the peak pressure of the coalesced shocks as a function of distance above the burst; and (3) the effects of the surface and the heating of the air near the surface on precursor formation, growth, and shock wave interaction on Shots 1, 3, 4, 6, 8, 9, and 12.

In addition to the above, photographic records were obtained on Shot 7, the underground shot, to study the growth of the base-surge cloud and to determine its role in the spread of radioactive contaminants. The project was concerned with this task only to the extent of assuring procurement of the desired records. The analysis and results will be published under an AFSWP-sponsored task at the Naval Ordnance Laboratory (Reference 8).

These objectives were established for the purposes of (1) providing blast attenuation data and determining the amount of energy that goes into blast when a nuclear device is burst under rarified atmospheric conditions; (2) determining whether the incident and reflected shocks coalesce at some distance above a tower burst and, if so, what the resultant pressure is as a function of distance; and (3) gathering precursor data for a number of shots varying in yield and height of burst over or near various surfaces, so improved methods can be formulated for predicting precursor effects on ideal blast and on diffraction- and drag-type targets.

1.2 BACKGROUND AND THEORY

While Objectives 1 and 3 were aimed toward increasing the knowledge of the military effects to be expected from weapons burst under previously untested environmental conditions, Objective 2 was directed toward providing basic information on shock phenomena from a tower burst in support of the drone-aircraft program, which was established to determine the damaging effects of gust loading on aircraft in flight. To facilitate this study, it was desired that the drone aircraft, to be tested on Shot 12, be subjected to but one shock. Promising, though inconclusive, data obtained by shock photography during Operation UPSHOT-KNOTHOLE (Shots 1 and 11) indicated that in the region directly above the burst the reflected wave might overtake the incident wave, provided the explosion were big enough and low enough. If such were the case, the coalesced shocks should thereafter proceed as one. Thus, it was intended that sufficient data be obtained by Project 1.2 prior to Shot 12 to verify shock coalescence and determine the shock pressure as a function of distance beyond the point of coalescence. The position of the drones above the burst could then be established at the desired level of gust-loading input.

From photographic records, two basic quantities associated with the shock wave can be measured: relative distance and relative time. Absolute values of these parameters can be determined by correlating the relative measurements with highly accurate engineering survey data and early fireball measurements. To determine the peak pressure of the incident shock in free air from such data, the instantaneous shock velocity is determined first by fitting the arrival-time data with a smooth curve which is expressed in closed mathematical form. Differentiation of the empirical equation for this curve yields velocity as a function of distance. In the region just beyond the fireball and in the free-air region the fitting function for the arrival-time data is

$$t = \frac{R}{a} - \frac{1}{a}\int_{R_o}^{R} \frac{b^{1.5}}{b^{1.5} + R^{1.5}}\, dR + c \qquad (1.1)$$

where t = time
R = distance from burst zero
a, b, c = constants

Equation 1.1 is fitted to the data by the method of least squares on IBM computer equipment. Upon differentiation, the following equation

TABLE 1.1 - Summary Data for Teapot*

	Shot 1	Shot 2	Shot 3	Shot 4	Shot 5	Shot 6
Code Name	WASP	MOTH	TESLA	TURK	HORNET	BEE
Date	18 Feb	22 Feb	1 Mar	7 Mar	12 Mar	22 Mar
Location (Area)	T-7-4	T-3	T-9-b	T-2	T-3a	T-7-1a
Elevation of Ground Zero (ft)	4195	4026	4021	4491	4006	4245
Ground Zero - Relative to Aiming Point (ft)	426W 36N					
Yield $(KT)_{RC}$	1.16±0.03	2.39±0.1	6.85±0.34	43±2	3.61±0.1	7.76±0.2
Actual Height of Burst (ft) -H	761 Air	300 Tow	300 Tow	500 Tow	300 Tow	500 Tow
Atmospheric Pressure Ground Zero (mb) P_{oG} (psi) Burst Height (mb) P_{oH} (psi)	 880 12.77 846 12.28	 880 12.77 871 12.64	 876 12.71 868 12.60	 868 12.60 868.5 12.60	 881 12.78 872.8 12.67	 876 12.71 871 12.64
Air Temperature (Degree Cent.) Ground Zero - T_{oG} Burst Height - T_{oH}	 -3.0 -6.6	 -7.8 -4.2	 -3.9 3.3	 5.2 5.83	 -1.0 7.0	 1.0 5.0
Scaled Height of Burst - HS_d (1KT Sea Level)	683.0	213.4	150.1	135.5	186.2	240.2
Blast Scaling Factors Distance Scaling to 1 KT Sea Level $(S_d) = (P_{oH}/14.7W)^{1/3}$	0.8963	0.7112	0.5002	0.2711	0.6208	0.4804
Time Scaling to 1 KT Sea Level $(S_t) = S_d\left[(T_{oH} + 273)/293\right]^{1/2}$	0.8547	0.6812	0.4857	0.2645	0.6068	0.4678
Pressure Scaling to Sea Level $(S_p) = 14.7/P_{oH}$	1.197	1.163	1.167	1.166	1.160	1.163

	Shot 7	Shot 8	Shot 9	Shot 10	Shot 11	Shot 12
Code Name	ESS	APPLE	WASP'	HA	POST	MET
Date	23 Mar	29 Mar	29 Mar	6 Apr	6 Apr	15 Apr
Location (Area)	T-10a	T-4	T-7-4	T-5	T-9-c	FF
Elevation of Ground Zero (ft)	4288	4309	4194	4038	4235	3077
Ground Zero - Relative to Aiming Point (ft)			62W 95N	397±50W 36±50S		
Yield $(KT)_{RC}$	1.2	14.2±0.5	3.16±0.16	3.3±0.4	1.45±0.07	22.0±1
Actual Height of Burst (ft) -H	(-) 67	500 Tow	739 Air	32,582±100 Air	300 Tow	400 Tow
Atmospheric Pressure Ground Zero (mb) P_{oG} (psi) Burst Height (mb) P_{oH} (psi)	 870.9 12.64 - -	 867 12.58 854.1 12.39	 871 12.64 849 12.32	 882 12.80 222 3.22	 874 12.69 862.5 12.51	 908 13.18 895.1 12.98
Air Temperature (Degree Cent.) Ground Zero - T_{oG} Burst Height - T_{oH}	 16.3 -	 9.1 11.2	 13.4 12.6	 10.3 -47.7	 1.0 10.28	 19.5 18.9
Scaled Height of Burst - HS_d (1 KT Sea Level)	-	195.0	475.2	13,192	251.2	137.0
Blast Scaling Factors Distance Scaling to 1 KT	-	0.3901	0.6430	0.4049	0.8373	0.3424
Time Scaling to 1 KT Sea Level $(S_t) = S_d\left[(T_{oH}+ 273)/293\right]^{1/2}$	-	0.3842	0.6348	0.3550	0.8233	0.3417
Pressure Scaling to Sea Level $(S_p) = 14.7/P_{oH}$	-	1.186	1.193	4.563	1.174	1.132

*The yields given are the final radiochemistry values taken from the Report of the Test Director LA-1966, October 1955.

is obtained for the instantaneous shock velocity, U:

$$U = a \left[1 + \left(\frac{b}{R} \right)^{1.5} \right] \tag{1.2}$$

A complete explanation of the equation and method of fitting may be found in Reference 5.

The peak pressure of the shock wave can be calculated for values of the instantaneous shock velocity by using the Rankine-Hugoniot relation:

$$P_s = \frac{2 \gamma P_o}{\gamma + 1} \left[\left(\frac{U}{c_o} \right)^2 - 1 \right] \tag{1.3}$$

where P_s = peak shock overpressure, psi

P_o = ambient pressure ahead of the shock, psi

γ = ratio of specific heats for air = 1.40

U = shock velocity, ft/sec

c_o = speed of sound ahead of the shock = $1089 \sqrt{1 + T_o/273}$, ft/sec

T_o = ambient air temperature ahead of the shock, °C.

For those regions where shock pressures exceed 100 psi the Rankine-Hugoniot relation, Equation 1.3, becomes less reliable because of a gradual change in the applicable equation of state for air from which the relation is derived. In the pressure region from 100 to 500 psi, peak pressures are obtained by use of the Hirschfelder-Curtiss tables (Reference 9), which are based on the thermodynamic properties of air under these more extreme conditions. The tables give $(P_s + P_o)/P_o$ as a function of U/c_o with all the necessary corrections for the change in state accounted for (Reference 10).

1.3 TEST CHARACTERISTICS

A detailed list of test characteristics required for the various analyses is given in Table 1.1. Yields, meteorological data, scaling factors, and other pertinent data are presented.

Chapter 2

INSTRUMENTATION

2.1 ROCKET-SMOKE-GRID PHOTOGRAPHY

The experimental technique consists of establishing a smoke-trail grid behind the burst and taking relatively high-speed (100 to 500 frames/sec), high-resolution, timed motion-picture photographs of the burst. The film records show the locus of the shock front as a function of time. Reflected light from the smoke trails is refracted when the shock front intersects the light path from the grid to the camera, causing that portion of the trail behind the shock to appear displaced from its original position. Each smoke trail in the grid thus affected has the appearance of being broken or hooked. The only purpose of the smoke grid is to make the detection of the shock front easier and the measurement of the shock radius more accurate; therefore, knowledge of the exact location of the grid is not required.

The smoke trails which formed the background grid on Shots 4, 8, and 12 were generated by firing sixteen 5-inch spin-stabilized rockets on Shot 4 and 20 rockets on Shots 8 and 12. Plan views of the rocket-line layouts for the smoke-grid experiments on these shots are shown in Figs. 2.1 and 2.2. Each rocket consisted of a 5-inch Mark 3 Mod 4 electric-firing rocket motor and a modified 5-inch Mark 10 rocket head loaded with 10 pounds of FS chemical smoke mix. The heads were modified by drilling thru-holes 120° apart, located a few inches above the base, through the wall into the cavity. An insert, called a scoop, was welded into each hole. As soon as the rocket motor was ignited, the entire missile was caused to spin and the external nipples of the inserts were sheared off by the rails in the launcher tube, allowing the FS to escape into the air to form a dense, white smoke.

The launcher used on this operation consisted of a 5-inch Mark 50 launching tube mounted on a rugged base made of 2-inch steel pipe. The tube was suspended from the pipe framework by means of a pillow block bolted to a plate which was welded to the tube at the center of gravity (when loaded). With this type of construction the tube was easily elevated to any desired angle.

Power was supplied to each rocket launcher by a step-down transformer (110 volts primary to 6.3 volts secondary) located at each rocket station. The primary of each transformer was connected in parallel to the main power line, which extended from a centrally located power station to each end of the rocket line. Firing of the rockets was completed automatically from the central power station by a delay timer at approximately H-8 seconds. The delay timer was initiated by a -15-second hard-wire timing signal provided by Edgerton, Germeshausen and Grier, Inc. (EG&G). After

TABLE 2.1 - Camera Coverage for Smoke Rocket and Dire[illegible]ock Photography

Shot	Camera Station	Type of Camera	Effective Focal Length (mm)	Total Horiz. Coverage (ft)	Vertical Coverage Above Ground (ft)	Camera Speed (fps)	Angle of Elevation (Degrees)	Aiming Point	Camera Location	Remarks
1	7-357	Mitchell	100.1	2,500		100	3°25'	GZ	853,124N 678,000E	
	7-360	"	100.3	3,400		100	0°00'	2°00'RGZ	845,216N 701,169E	Direct Photo.
	7-360	"	99.97	3,400		100	0°00'	2°00'LGZ	"	
3	7-357	Mitchell	100.1	3,000		100	4°00'	GZ	853,124N 678,000E	
	7-357	"	152.2	2,000		100	2°45'	2°20'RGZ		Direct Photo.
	7-357	"	152.3	2,000		100	2°45'	2°20'LGZ	"	
4	4-357	Mitchell	34.46	12,500	5,500	100	1°30'	GZ	853,306N 651,033E	
	4-357	"	50.04	8,800	5,500	100	5°40'	GZ		Rockets
	4-357	"	50.19	8,800	4,500	100	2°45'	GZ	"	
	4-357	"	74.83	5,800	3,500	100	3°15'	GZ	"	
6	7-357	Mitchell	100.3	2,300		100	0°00'	GZ	853,124N 678,000E	
	7-357	"	74.83	3,050		100	0°00'	GZ		Direct Photo.
	7-357	"	74.90	3,050		100	0°00'	7°50'RGZ	"	
	7-357	"	75.26	3,050		100	0°00'	7°50'LGZ	"	
8	4-357	Mitchell	34.46	9,600	5,500	100	5°50'	GZ	853,306N 651,033E	
	4-357	"	50.22	6,700	5,200	100	9°00'	GZ		Rockets
	4-357	"	50.19	6,700	4,500	100	7°30'	GZ	"	
	4-357	"	74.83	4,500	3,500	100	5°20'	GZ	"	
9	7-357	Mitchell	74.90	3,300		100	5°10'	GZ	853,124N 678,000E	Direct Photo.
	7-357	"	100.3	2,450		100	4°00'	GZ		
	7-357	"	100.0	2,450		100	3°25'	GZ	"	
10 and 10 dry run	1-355	Fastax	251.6	3,500	2,400	500	81°08'	Bomb Zero	831,635N 672,338E	
	1-355	Mitchell	152.3	5,200	4,100	100	81°08'	"		Smoke Grid
	372	Mitchell	151.9	7,300	5,800	100	42°25'	"	795,962N 674,980E	
	372	Mitchell	583.4	1,900	1,500	100	42°25'	"		
12	372	Mitchell	151.9		5,700	100	00°00'	GZ	795,962N 674,980E	Rockets
	372	Mitchell	249.6		4,100	100	00°00'	GZ		
	372	"	583.4		3,300	100	00°00'	GZ	"	
	F-362	Fastax	152.1	1,900		500	00°00'	GZ	745,844N 703,951E	
	F-362	Mitchell	100.1	2,900		100	00°00'	GZ		
	F-360	"	99.1	1,900		100	00°00'	20°45'LGZ	738,343N 713,027E	
	9.1EZ	"	99.31	2,400		100	00°00'	11°20'RGZ	744,262N 705,980E	Direct Photo.
	9.1EZ	"	152.3	1,600		100	00°00'	17°00'RGZ	"	
	9.1E1	"	100.0	2,400		100	00°00'	11°20'LGZ	748,250N 705,997E	
	9.1E1	"	152.3	1,600		100	00°00'	17°00'LGZ		
	F9.1E3	"	99.2	1,900		100	00°00'	5°45'LGZ	736,257N 715,999E	

a delay of approximately 7 seconds, the delay timer completed the circuit to the main power line, causing 110 volts to be applied to the primary of each transformer. The rockets were fired simultaneously in this manner. Fig. 2.3 shows the rocket-line firing circuit.

The principal region of interest on Shots 4, 8, and 12 was the free-air region directly above the burst point. For this reason the smoke grid was concentrated in that vicinity. This was accomplished by firing the smoke rockets in a criss-cross pattern, such that the trails appeared to intersect in a vertical plane directly above the burst point (see Fig. 2.4). The camera stations were installed and operated by EG&G according to NOL specifications. Table 2.1 lists the photographic details for all shots in which Project 1.2 participated.

The photographic records obtained in conjunction with the smoke grids were enlarged on a direct projection Recordak. Breaks or hooks in the smoke trails indicated the position of the shock front on each frame. Knowing the effective focal length of the camera lens and the distance to the plane of measurement, the distance scaling factor was determined. Also recorded on the film was a 200-cycle timing signal, so the time for each frame was determined. (Table 2.2 lists the calibration constants for all films from which data were obtained.) Shock-wave time-of-arrival data were then measured for each frame; from these data the instantaneous shock velocities were determined and peak overpressures calculated as a function of distance (see Section 1.2).

TABLE 2.2 - Film Calibration Constants

Shot No.	Film No.	Distance to Place of Measurement (ft)	Distance Scaling on Tracing (Image Magnified 19 Times)	Speed of Camera (fps)	Time Per Frame (sec)	Establishment of Absolute Time
1	28881	9,846	1mm - 6.874 ft	100	---	---
4	28183	18,690	1mm = 13.104 ft	101.03	0.009898	1st Frame - 2.58 ms
	28184	18,690	1mm = 19.492 ft	99.01	0.010100	1st Frame - 9.95 ms
6	28081	9,572	1mm = 6.689 ft	100.91	0.00991	1st Frame - 8.40 ms
	28084	9,572	1mm = 5.006 ft	99.70	0.01003	1st Frame - 8.00 ms
8	28282	13,216	1mm = 13.774 ft	100.81	0.00992	2nd Frame - 10.70 ms
	28284	13,320	1mm = 9.313 ft	101.11	0.00989	2nd Frame - 11.25 ms
9	29384	10,228	1mm = 5 312 ft	101.32	0.00987	1st Frame - 9.32 ms
10	28980	32,934	1mm = 6.856 ft	650	**	1st Frame - 1.55 ms
12	28381	12,056	1mm = 5.797 ft	101.95	0.00980	1st Frame - 7.32 ms
	28382	7,914	1mm = 4.154 ft	103.09	0.00970	***
	28283	10,020	1mm = 5.228 ft	102.88	0.00972	1st Frame - 1.00 ms
	28387	9,943	1mm = 5.178 ft	92.76	0.01078	1st Frame - 5.15 ms
	28389	64,451	1mm = 13.236 ft	101.42	0.00986	1st Frame - 7.42 ms
	28390	64,451	1mm = 5.797 ft	101.01	0.00990	*

* Absolute Time Obtained by Comparison with Film 28389.
** Time between Frames varied over Region of Interest.
*** Absolute Time Obtained by Comparison with Film 28387.

Instrumentation for the smoke-rocket experiments on Shots 4, 8, and 12 operated successfully. Of a total number of 72 expected trails, only three failures were encountered. (The 72 expected trails include a premature firing of all 16 rockets on Shot 4 as a result of a spurious signal delivered to the rocket line firing circuit at approximately 2 hours before zero time. However, the shot was postponed, because of adverse weather conditions, and the rocket line was reloaded and fired again on shot day at the proper time.) One of the failures was attributed

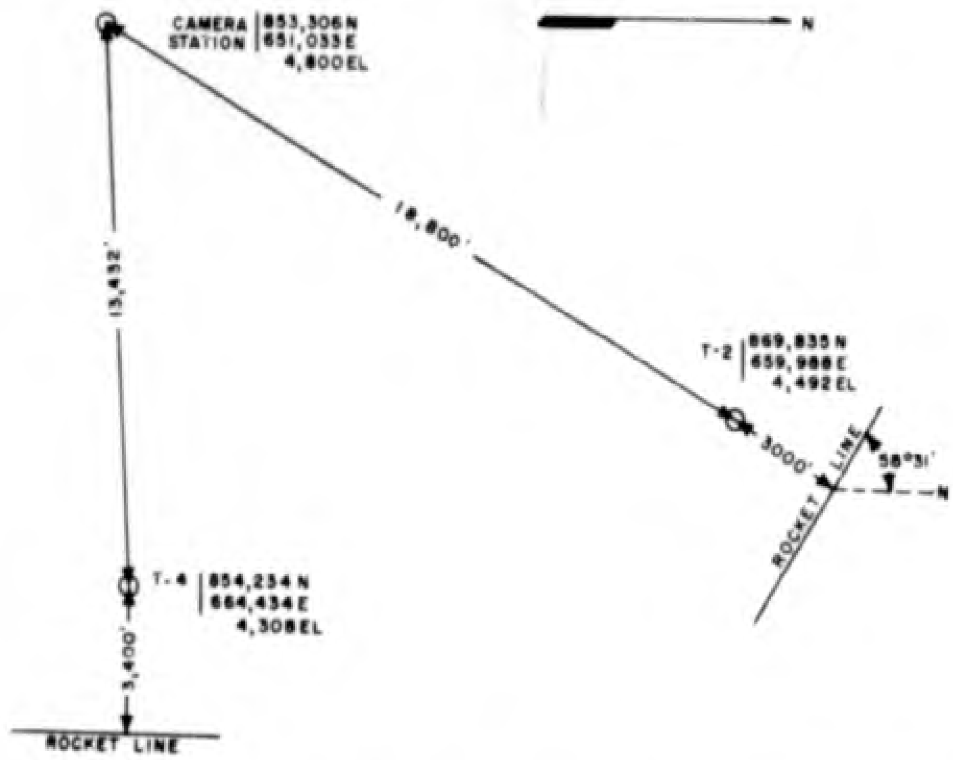

Figure 2.1 Rocket photography layout, Shots 4 (T-2) and 8 (T-4).

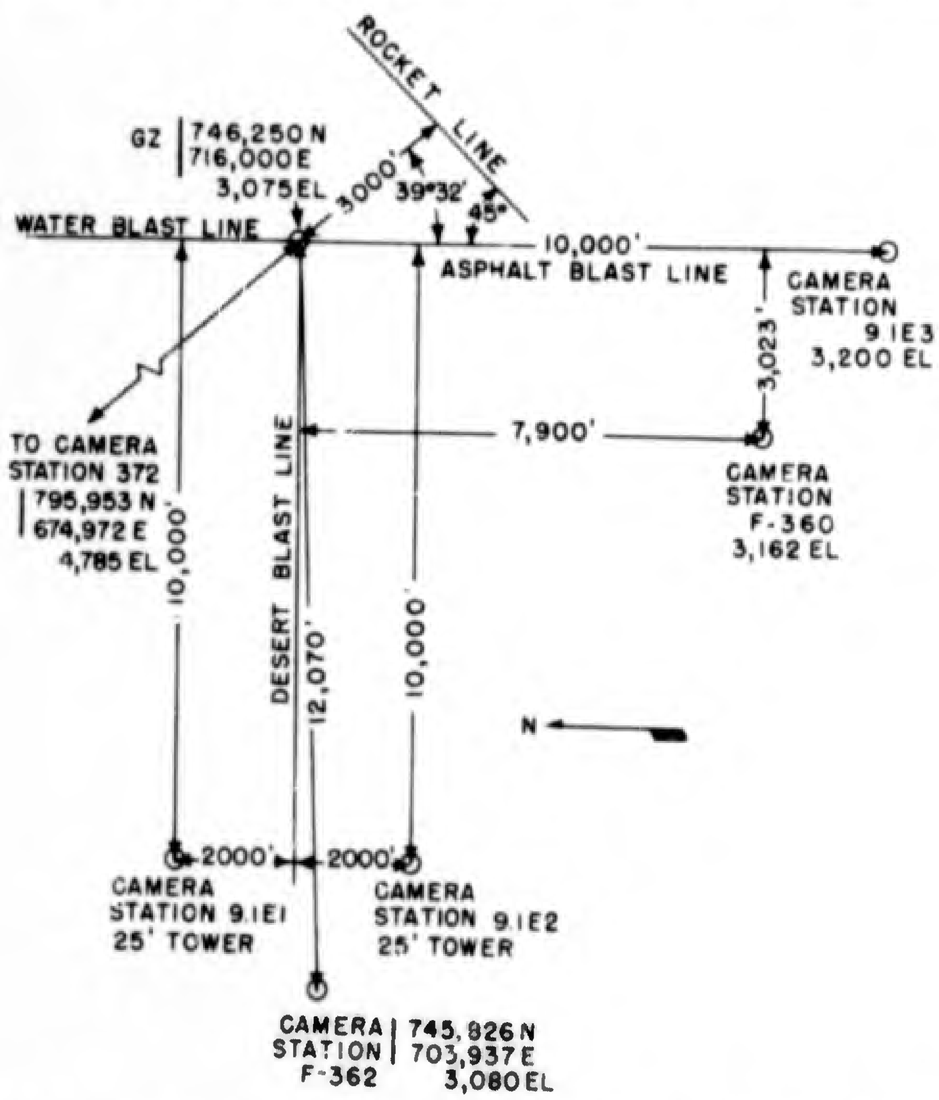

Figure 2.2 Rocket and direct shock photography layout for Shot 12.

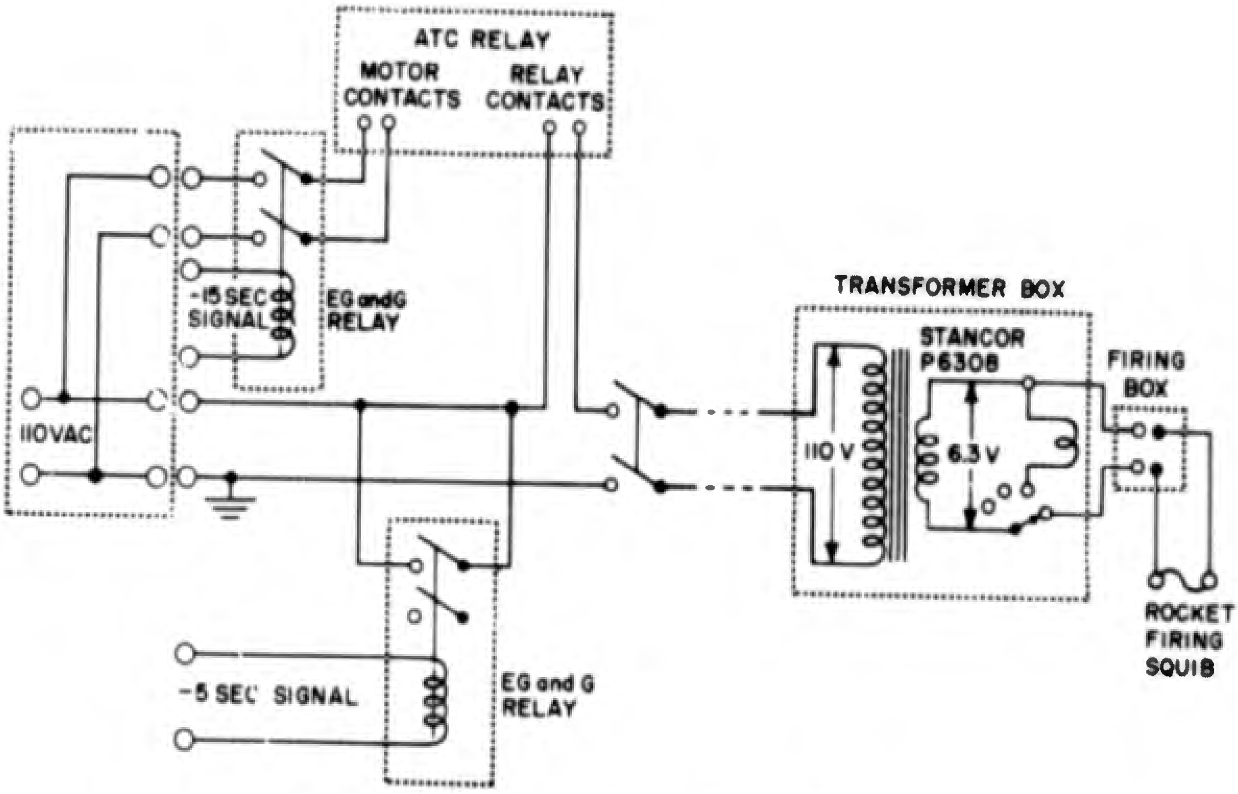

Figure 2.3 Rocket line firing circuit.

ROCKET NO.	ANGLE OF ELEVATION	FIRING TIME
1	60°	H-7.5SEC
2	60°	"
3	60°	"
4	60°	"
5	60°	"
6	60°	"
7	70°	"
8	70°	"
* 9	70°	"
* 10	70°	"
* 11	70°	H-8 SEC
* 12	70°	"
13	70°	"
14	70°	"
15	60°	"
16	60°	"
17	60°	"
18	60°	"
19	60°	"
20	60°	"

* TRAILS 9, 10, 11, AND 12 ARE NOT PRESENT ON SHOT 4

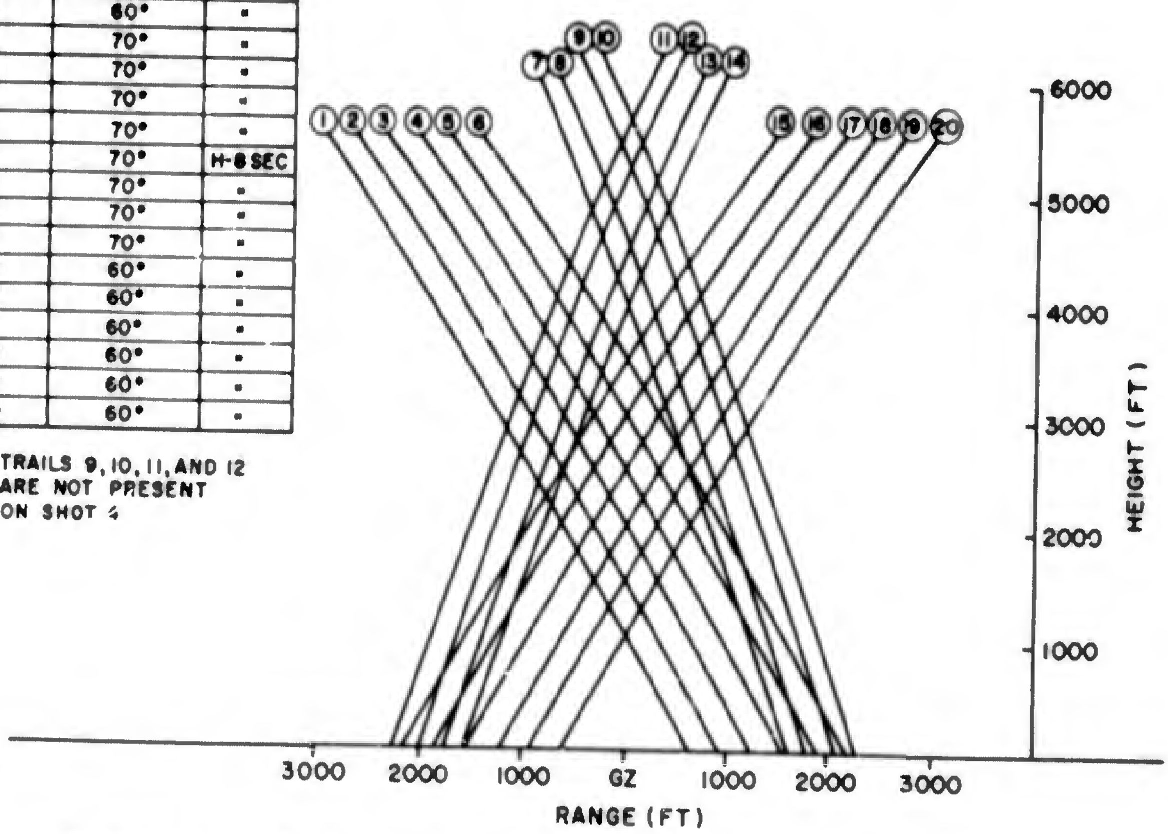

Figure 2.4 Smoke rocket grid for Shots 4, 8, and 12.

[redacted]

to a defective rocket motor, which failed to fire. The other two rockets fired but failed to smoke, probably because the launcher rails did not shear off the external nipples. Two of the three failures occurred on Shot 4; the other on Shot 12. However, the grids produced on these shots were adequate. All of the cameras operated, and excellent photographs were obtained on all three shots.

2.2 HIGH-ALTITUDE SMOKE GRID

The high altitude shot, Shot 10, introduced the problem of how to form a background smoke grid for the free air shock photography experi-

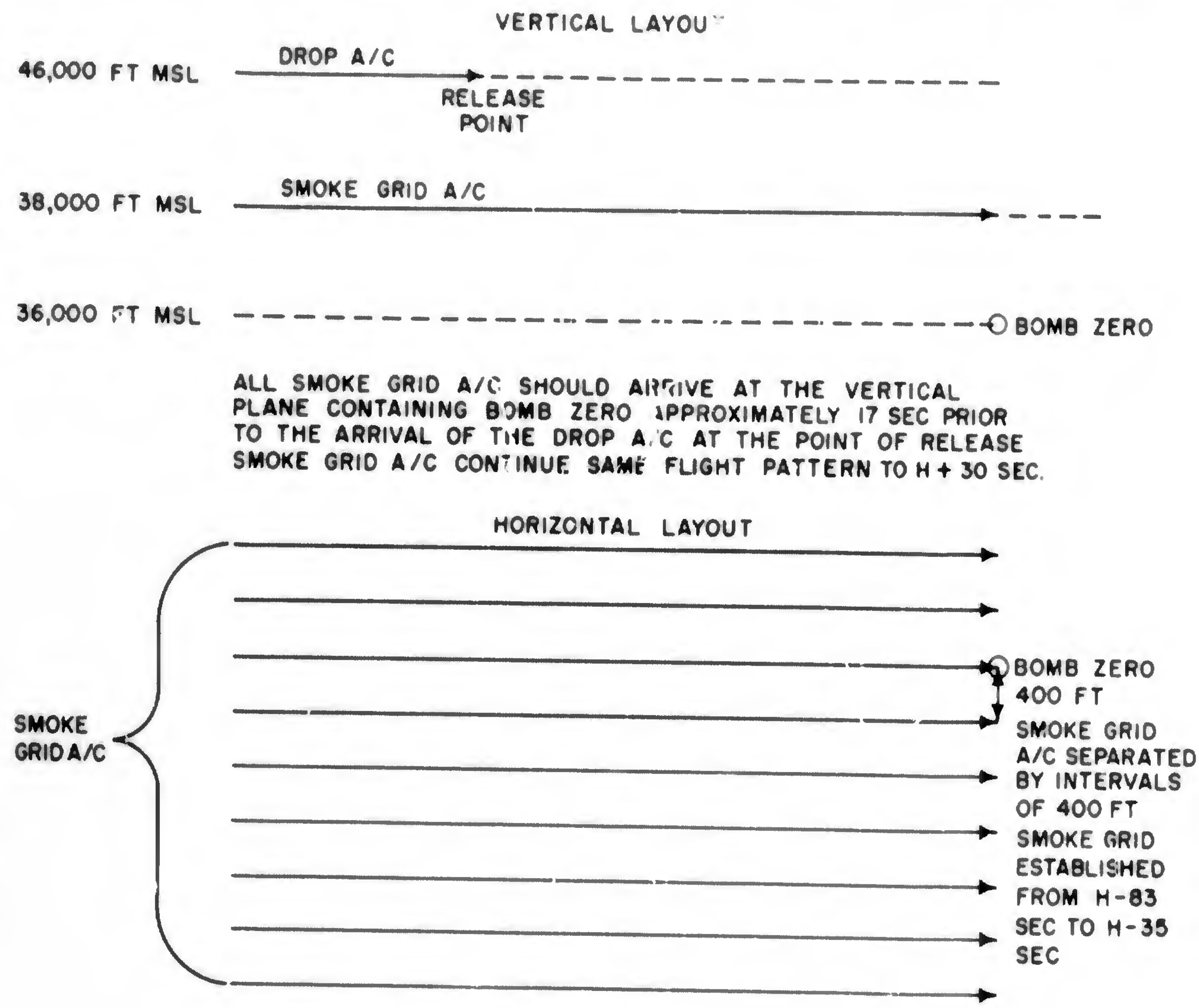

Figure 2.5 Deployment of smoke grid A/C, Shot 10.

ment. Since the standard smoke rockets normally used could not reach the desired altitude, it was necessary to employ some other means to produce the grid. A review of the problem indicated that two types of grids could be used. Either the grid could be vertical, in which case the smoke trails could be formed by dropping smoking missiles from aircraft at a higher altitude than the burst, or it could be horizontal, as formed by horizontally-flying aircraft releasing a smoke-producing agent (similar to skywriting techniques) to make a horizontal grid above the bomb burst. The latter method was decided to be the most reliable from the technical standpoint in view of the uncertainty of burst position.

The grid was to be similar in form to those generated by smoke rockets on past atomic tests, i.e., a straight line grid. The proposed grid lines were to be spaced at 400-ft intervals. To establish the grid, the aircraft were to fly into the wind (wind expected from 290° ± 15°) at an altitude that was fixed 8,000 ft below the "drop" aircraft. (The bomb was to be burst at an altitude 10,000 ft below the drop altitude, thus fixing the smoke grid 2,000 ft above the burst.) Each smoke aircraft was to generate a smoke trail along a horizontal line of

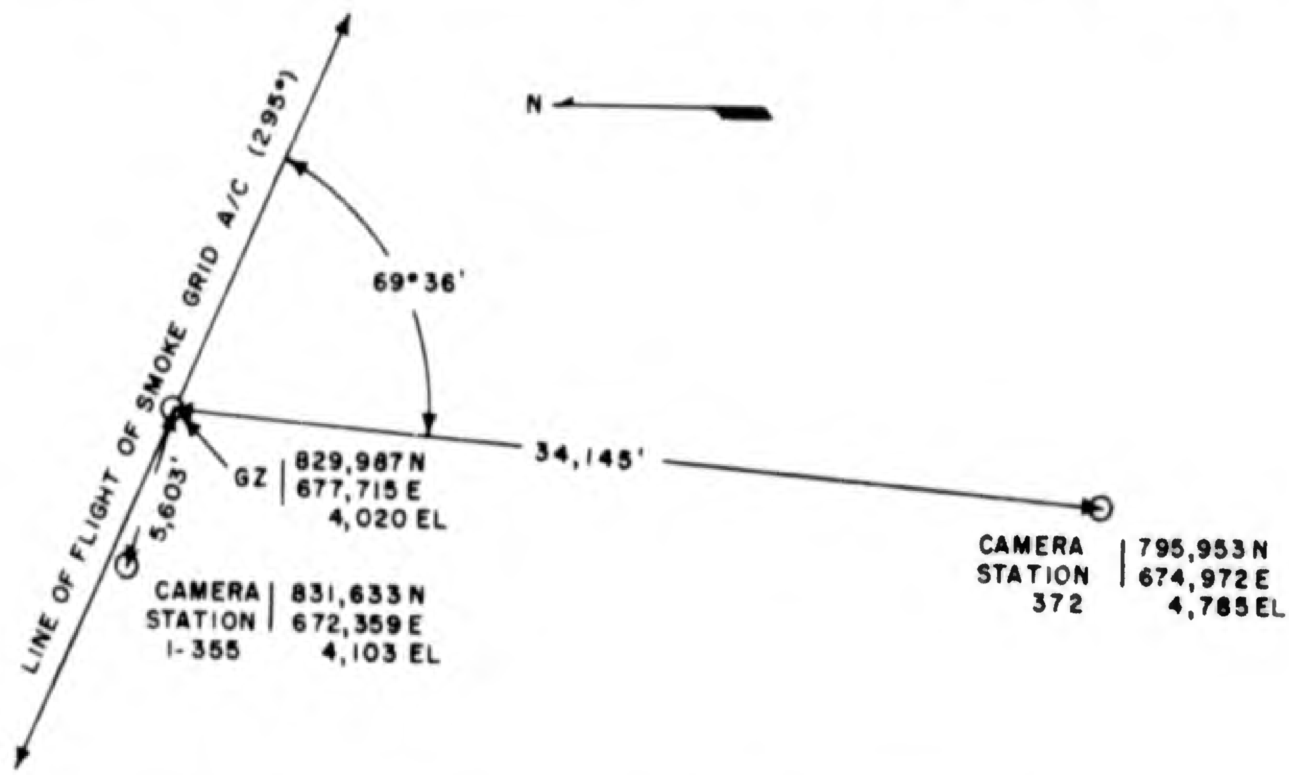

Figure 2.6 Smoke grid photography layout, Shots 10 and 10 dry run (Area 5).

flight for approximately 50 sec, beginning at H-83 sec and continuing to about H-35 sec. The smoke trails would then extend about 10,000 ft to each side of air zero. Fig. 2.5 shows the intended position of the smoke grid at bomb-release time. Cameras located on the ground were to be aimed vertically upward, and high-speed motion pictures of the burst were to be taken. (Fig. 2.6 shows the camera plan layout for Shot 10 and the Shot 10 dry run.)

The responsibility for developing and testing suitable smoke generators, installing them in suitable aircraft, training personnel for the Operation, and establishing the desired smoke grid during the Operation was assigned to the 4925th Test Group (Atomic) of the Air Force Special Weapons Center, Kirtland Air Force Base, New Mexico. Specifications as to length, density, and persistency of the smoke

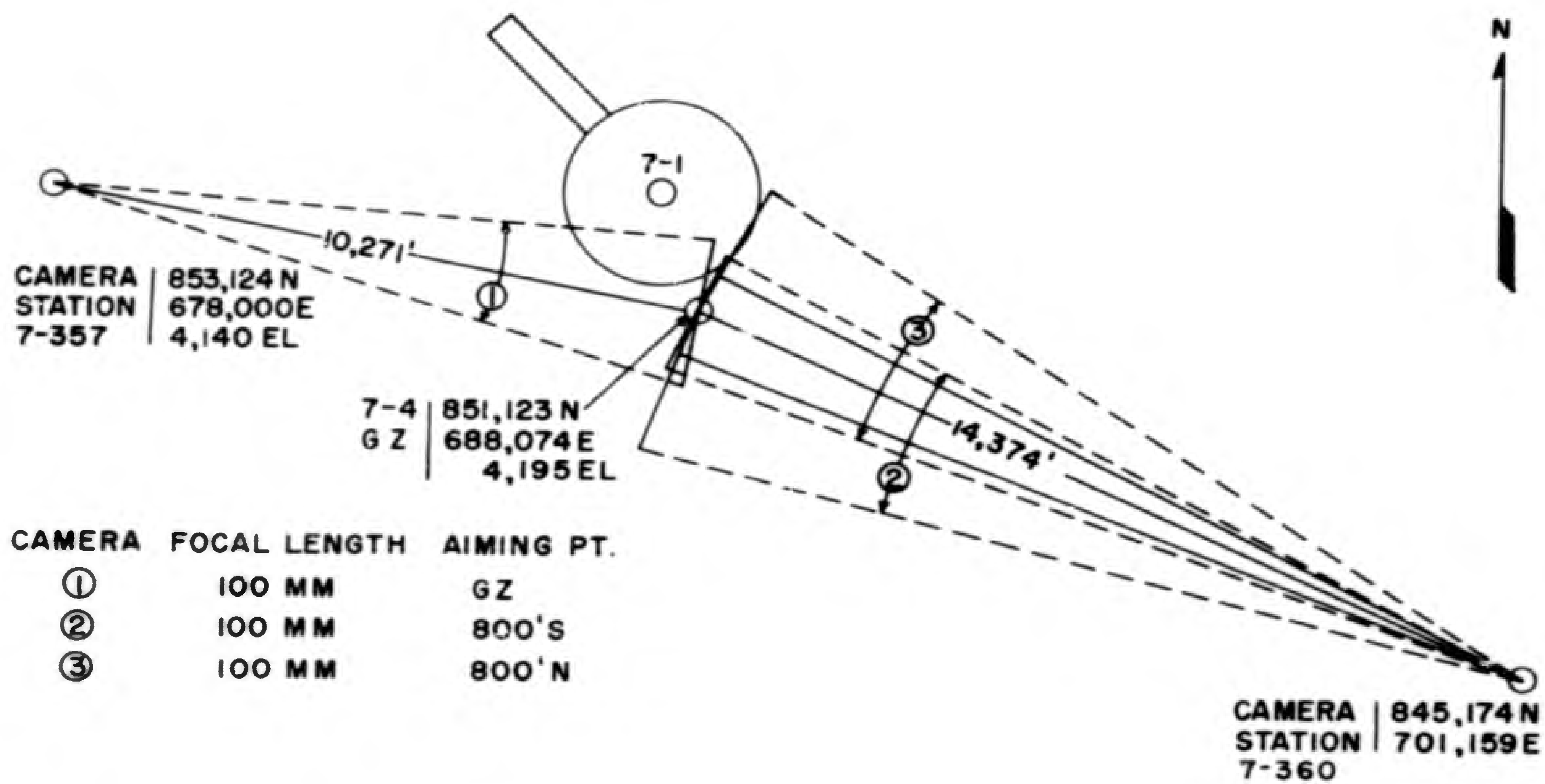

Figure 2.7 Shot 1, direct shock photography layout.

trails were supplied to the 4925th Test Group by the Naval Ordnance Laboratory.

Two systems for producing smoke were developed, tested, and made available for use during the Operation. (Reference 22 is a detailed report of these developments.) In one, atomized Corvis oil is injected into the jet exhaust of each aircraft to produce the trail. (The oil, first vaporized by the hot gases in the jet, freezes shortly thereafter to form a bluish-white smoke.) This technique was to be used whether condensation trails were being formed naturally or not to assure a positive, durable trail. As a back-up to the oil-injection apparatus, each aircraft was equipped with a commercial smoke generator produced by the Del Mar Corporation of San Francisco. These generators used charges of titanium tetrachloride in capsule form, each capsule capable of generating smoke for 6 sec. Enough charges could be inserted to generate a continuous trail for 30 sec.

During the Operation, eight aircraft were used to produce the smoke grid. One B-47 was used as a master guide or reference point upon which the remaining seven aircraft (F-84's and F-86's) based their position.

On the Shot 10 dry run, condensation trails were very evident and a good set of persistent trails was produced. However, an error in the judgment of the aircraft pilots spaced the trails at too wide intervals (from 2000 to 3000 ft).

On Shot 10 the spacing between grid trails was considerably better, ranging from 200 to 600 ft, but in most cases was excessive. The ambient conditions at the altitude of the smoke grid were such that good condensation trails were not produced. The grid was not satisfactory and was of essentially no use in the analysis of the films. The smoke trails made by the aircraft appeared as a series of very light, discontinuous puffs of smoke (see Fig. 3.32). No hooks, breaks or discontinuities, such as those observed when the shock front propagates in front of a rocket smoke grid could be distinguished from the natural breaks in the trail. Undoubtedly these natural breaks occurred because of the method used to deploy the smoke.

Most of the analysis of Shot 10 records was done by direct shock photography, and because of the lack of contrast on the films, it was extremely difficult to detect the shock front. A slight modification in the method normally used for the analysis of the films was necessary. Instead of observing the projected images of the film (magnified approximately 20 times) by use of the Recordak and tracing the shock front frame by frame, projection prints were made of each frame of the film, the magnification being approximately six times. By varying the amount of light and the exposure times, it was possible to obtain better contrast than could be obtained in the Recordak. On those frames where the shock front was detectable outside of the fireball region, the diameter of the shock was measured and the growth of the shock front as a function of

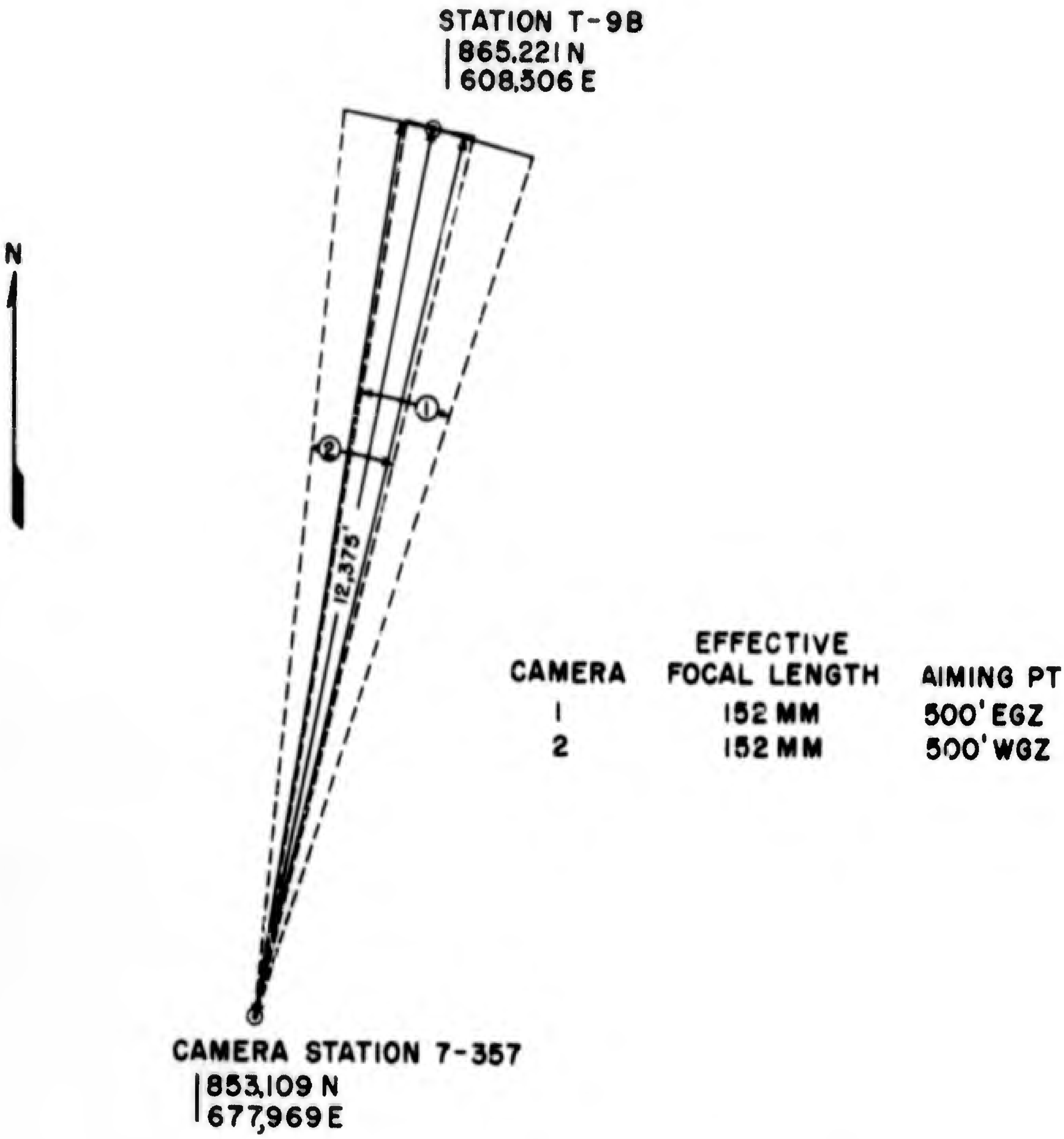

Figure 2.8 Shot 3, camera plan layout for direct shock photography.

time was obtained. The rest of the analysis followed the procedure outlined in Section 1.2.

2.3 DIRECT SHOCK PHOTOGRAPHY

This project also instrumented five shots with direct shock photography, including Shots 1, 3, 6, 9, and 12. The instrumentation for the direct shock photography included a number of high-speed 35-mm Mitchell cameras operating at 100 frames/sec and a few 35-mm Fastax cameras operating at approximately 500 frames/sec. Each camera was equipped

[redacted]

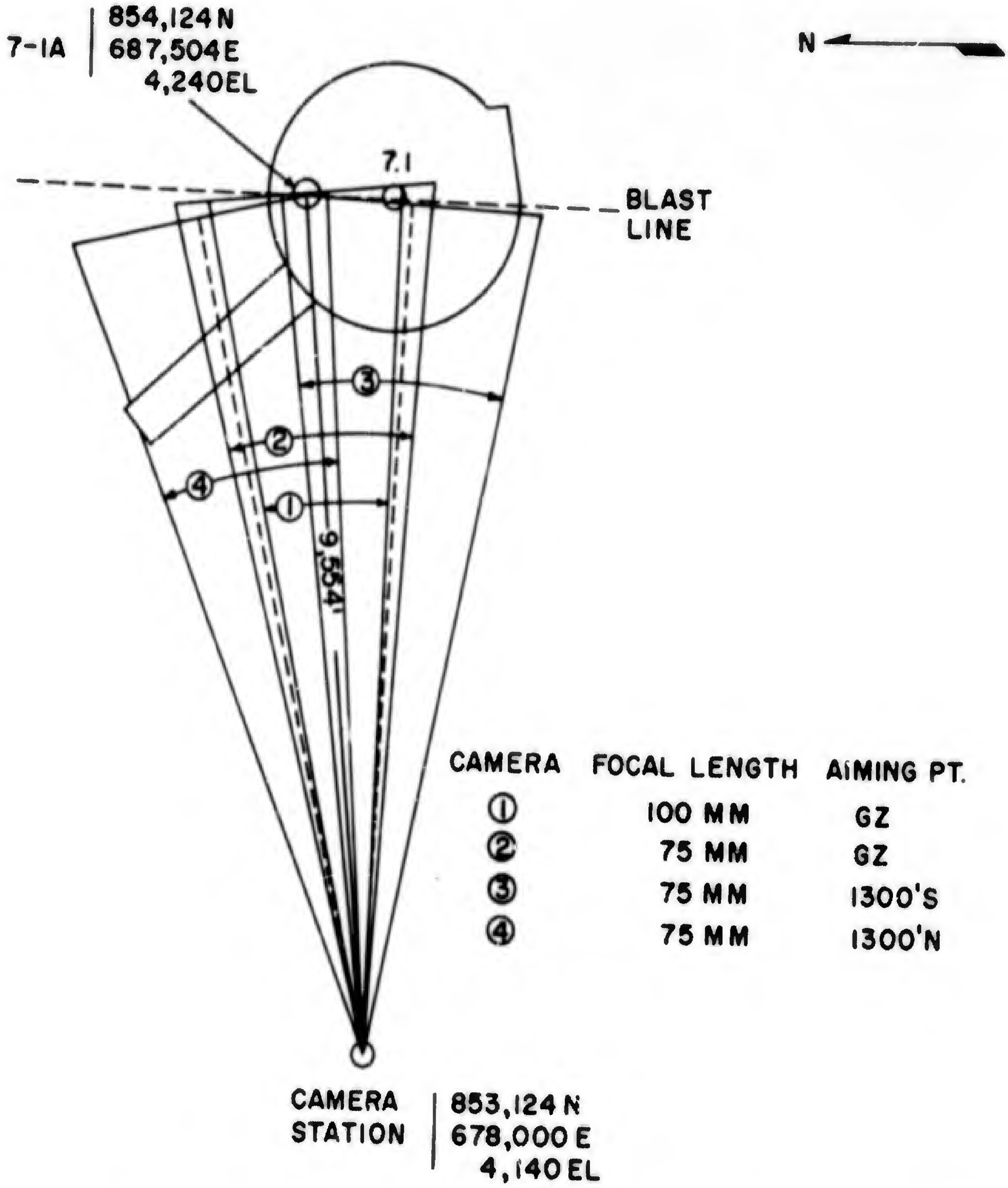

Figure 2.9 Shot 6, direct shock photography layout.

with the necessary apparatus to provide timing marks on the film. The cameras were located and aimed so that full coverage over the regions of greatest interest was obtained. The camera stations again were installed and operated by EG&G according to NOL specifications. Figures 2.2, 2.7, 2.8, 2.9, and 2.10 show the plan layout for the direct photographic coverage for the various shots. Photographic details for each shot are given in Table 2.1.

Tracings of the shock contours near the surface were made by direct projection in the Recordak. With timing and distance scales obtained

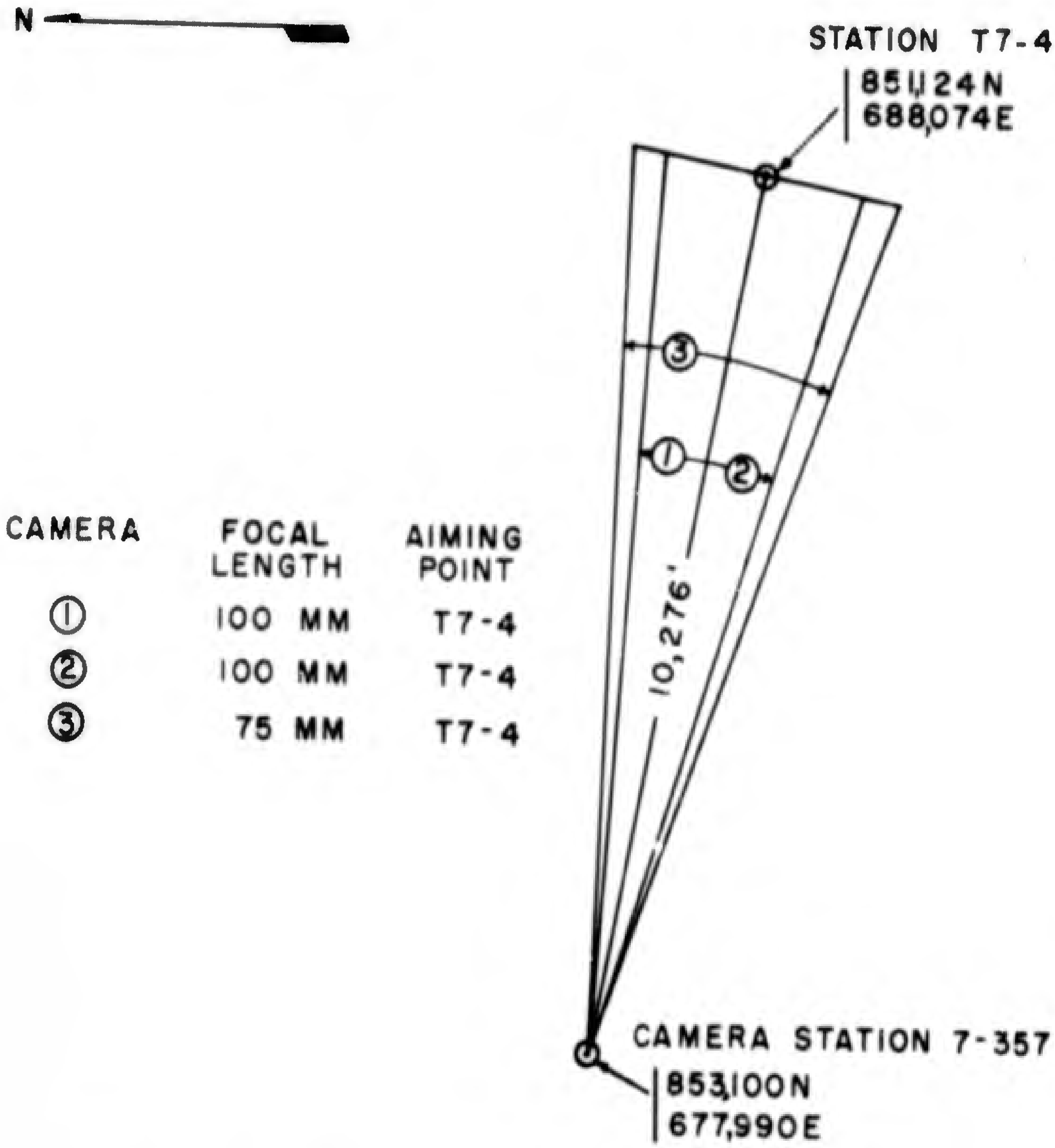

CAMERA	FOCAL LENGTH	AIMING POINT
①	100 MM	T7-4
②	100 MM	T7-4
③	75 MM	T7-4

Figure 2.10 Shot 9, camera plan layout for direct shock photography.

from the films, measurements of the space-time history of the incident, reflected, and Mach shocks were made directly from the tracings. The path of the triple point and precursor formation and growth were also measured in the same manner.

Some of the photographic records were lost or partially impaired either because of overexposure of the film, as on Shots 3 and 12, or because of the failure of the timing apparatus on the cameras, as on Shot 1. Much useful information was obtained, however, and in the opinion of the authors, the objectives were met successfully.

Chapter 3
RESULTS

The photographic results obtained by this project are reported shot by shot. In general, excellent results, both in the free-air region and along the surface, were realized on most shots. Those cases in which cameras or timing instrumentation failed were at a minimum and the successful accomplishment of the experimental objectives was not impaired. Table 3.29 lists the films obtained on each shot and gives an indication of the data extracted from each.

3.1 SHOT 1

Excellent direct shock photography along the ground was obtained on this shot. However, failure of the timing equipment resulted in the loss of all timing data on the films and all other data can only be given with corresponding approximate relative times.

Arrival-time data of the incident shock along the ground northeast and southwest of ground zero were measured on Film 28881. Figure 3.1 shows the plane of measurement for this film. A comparison of these arrival-time data to both sides of ground zero is shown in Fig. 3.2. The distance data plotted in this graph are listed in Table 3.1 and are given as a function of frame number instead of time. Since the speed of the camera was approximately 100 frames/sec, the time between frames was approximately 10 msec. Thus an approximate time for each frame was obtained by multiplying the frame number by the factor 10. The accuracy of the time measured in this manner is difficult to determine but is probably better than ± 5 percent.

It is apparent from Fig. 3.2 that the arrival of the initial disturbance at a given distance to the northeast of ground zero was earlier than to the southwest of ground zero over a ground range from 400 to 1,000 ft. This is attributed to a slight thermal effect observed to occur to the northeast of ground zero (see Fig. 3.3 for an actual photograph of the shock taken from Film 28881). This thermal effect, observed on one side of ground zero but not the other, was probably caused by the presence of a sufficiently heated layer of air over an extensive surface of asphalt in the T-7 area to the northeast side of ground zero. The more-highly reflective area to the other side of ground zero was apparently incapable of causing the air above it to heat up sufficiently to produce the effect.

3.2 SHOT 3

Because of the unexpected high yield of the Shot 3 device, all of the direct shock photography films were heavily overexposed, and few

[redacted]

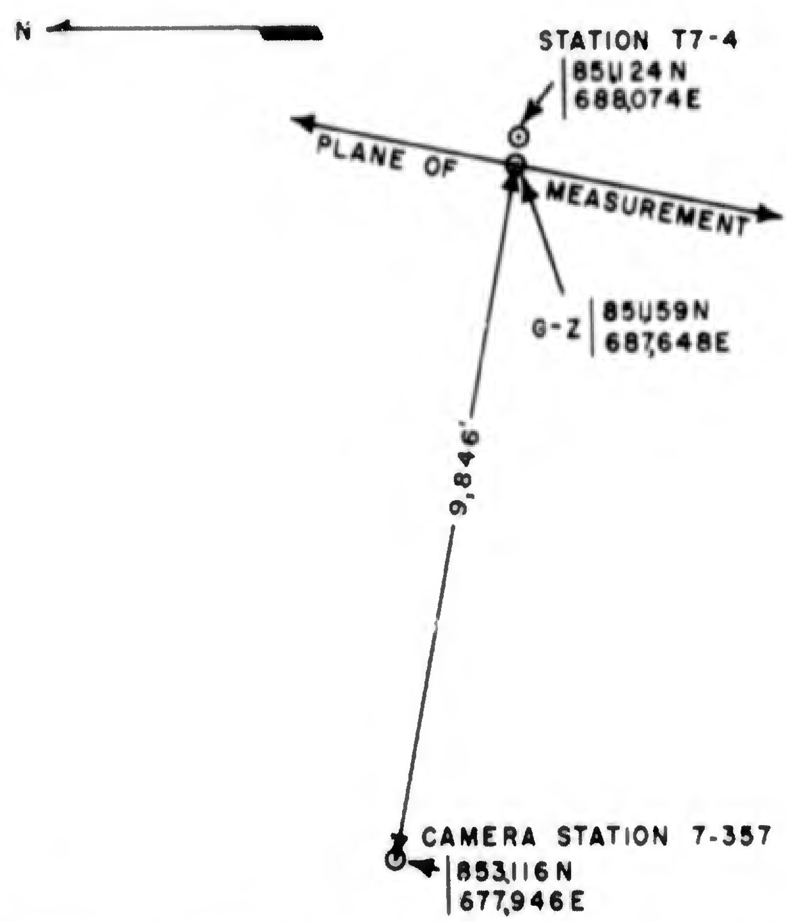

Figure 3.1 Shot 1, Plane of Measurement for Direct Shock Photography, Film 28881.

TABLE 3.1 - Shot 1 - Time of Arrival of the Initial Disturbance Along the Ground

Frame No.	Northeast Distance From GZ (ft)	Southwest Distance From GZ (ft)	Frame No.	Northeast Distance From GZ (ft)	Southwest Distance From GZ (ft)
		Film 28881			
30	250.9	264.0	58	968.5	965.8
31	316.2	301.1	59	983.7	982.3
32	356.1	370.5	60	1,005.0	998.8
33	393.9	394.6	61	1,025.6	1,014.0
34	426.2	439.9	62	1,041.4	1,038.0
35	459.2	473.6	63	1,055.2	1,055.2
36	484.6	492.6	64	1,071.7	1,073.7
37	516.9	522.4	65	1,090.2	1,087.5
38	534.0	543.0	66	1,108.1	1,103.3
39	569.2	586.4	67	1,124.6	1,118.4
40	591.9	611.8	68	1,146.6	1,132.8
41	618.7	631.7	69	1,152.8	
42	643.4	657.2	70	1,177.5	
43	666.8	678.5	71	1,194.0	1,175.5
44	687.4	708.0	72	1,213.3	1,203.0
45	701.8	729.3	73	1,221.5	
46	728.6	752.0	74	1,243.5	
47	752.7	767.1	75	1,269.6	
48	776.8	787.1	76	1,276.5	1,251.2
49	791.9	818.0	77	1,297.1	
50	813.2	835.9	78	1,308.1	
51	835.2	849.6	79	1,321.2	
52	855.1	870.0	80	1,345.9	
53	875.7	880.0	81	1,361.1	
54	892.2	907.4	82	1,363.1	
55	908.7	923.2	83	1,386.5	
56	931.4	930.1	84	1,411.9	
57	952.0	952.0	85	1,428.4	
			86	1,440.1	

[redacted]

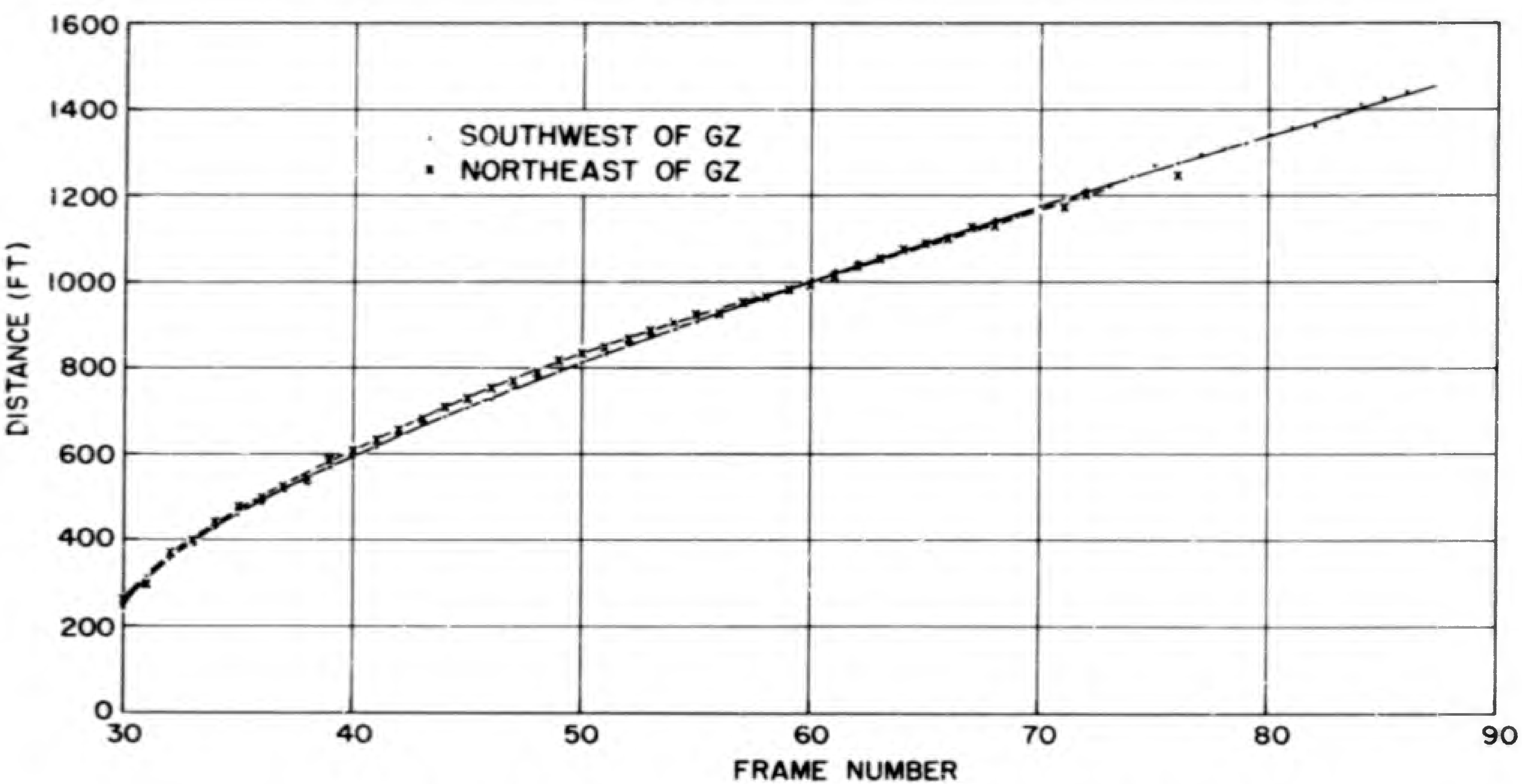

Figure 3.2 Shot 1, Comparison of Arrival of Incident Shock Along the Ground Northeast and Southwest of GZ.

[redacted]

data could be obtained, because of the lack of contrast and resolution. As a result, only qualitative statements can be made concerning the shock-wave phenomena on this shot.

Figure 3.4 shows a frame taken from Film 28681. The fireball was asymmetrical, and there was a thermal disturbance of the shock along the ground on both sides of ground zero.

3.3 SHOT 4

The arrival-time data for the free-air incident shock were measured on Films 28183 and 28184 (see Fig. 3.5 for the planes of measurement) over

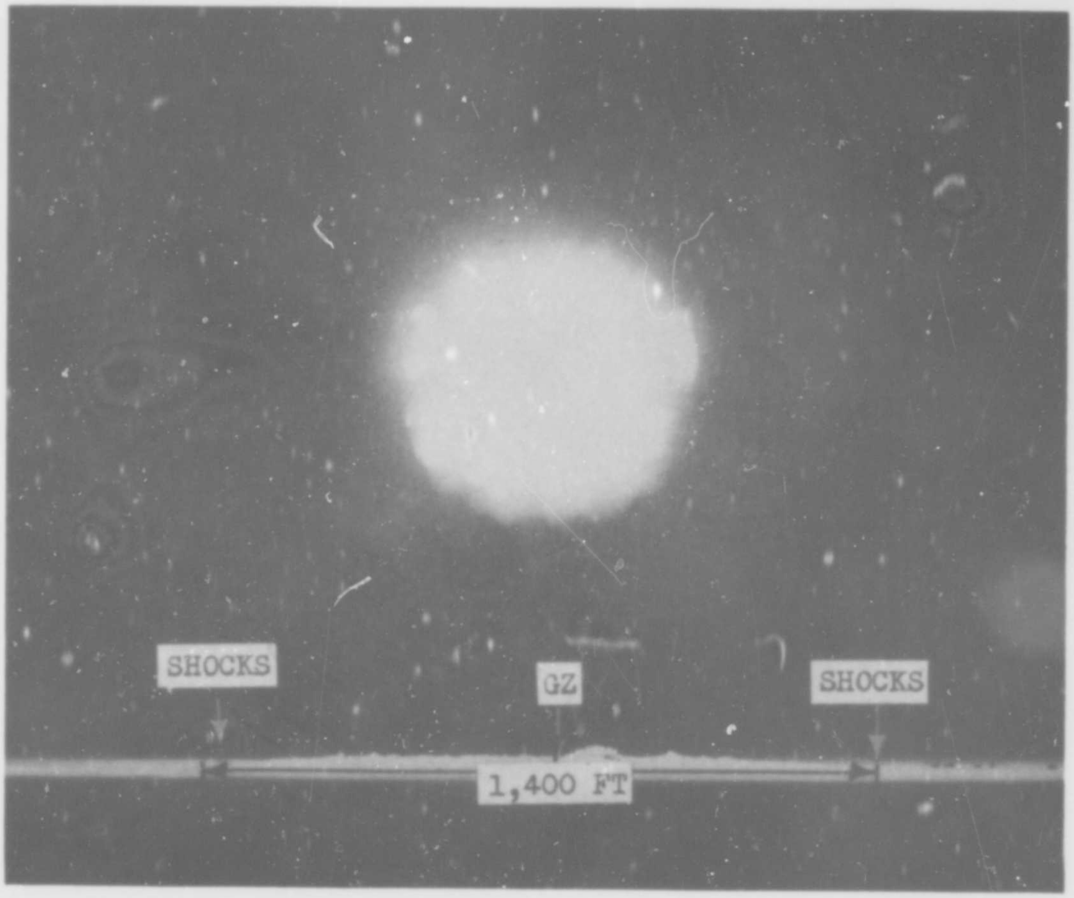

Figure 3.3 Shot 1, Shock Photography taken from Film 28881, Frame 44.

a range of from 200 to 3,000 ft directly above the burst point. These data are given in Table 3.2 and plotted in Fig. 3.6. The absolute time for each film was determined by plotting the earliest data point from NOL films on the curve representing fireball-growth data supplied by EG&G (see Fig. 3.7). These arrival-time data were fitted to Equation 1.1,

Continued on Page 39

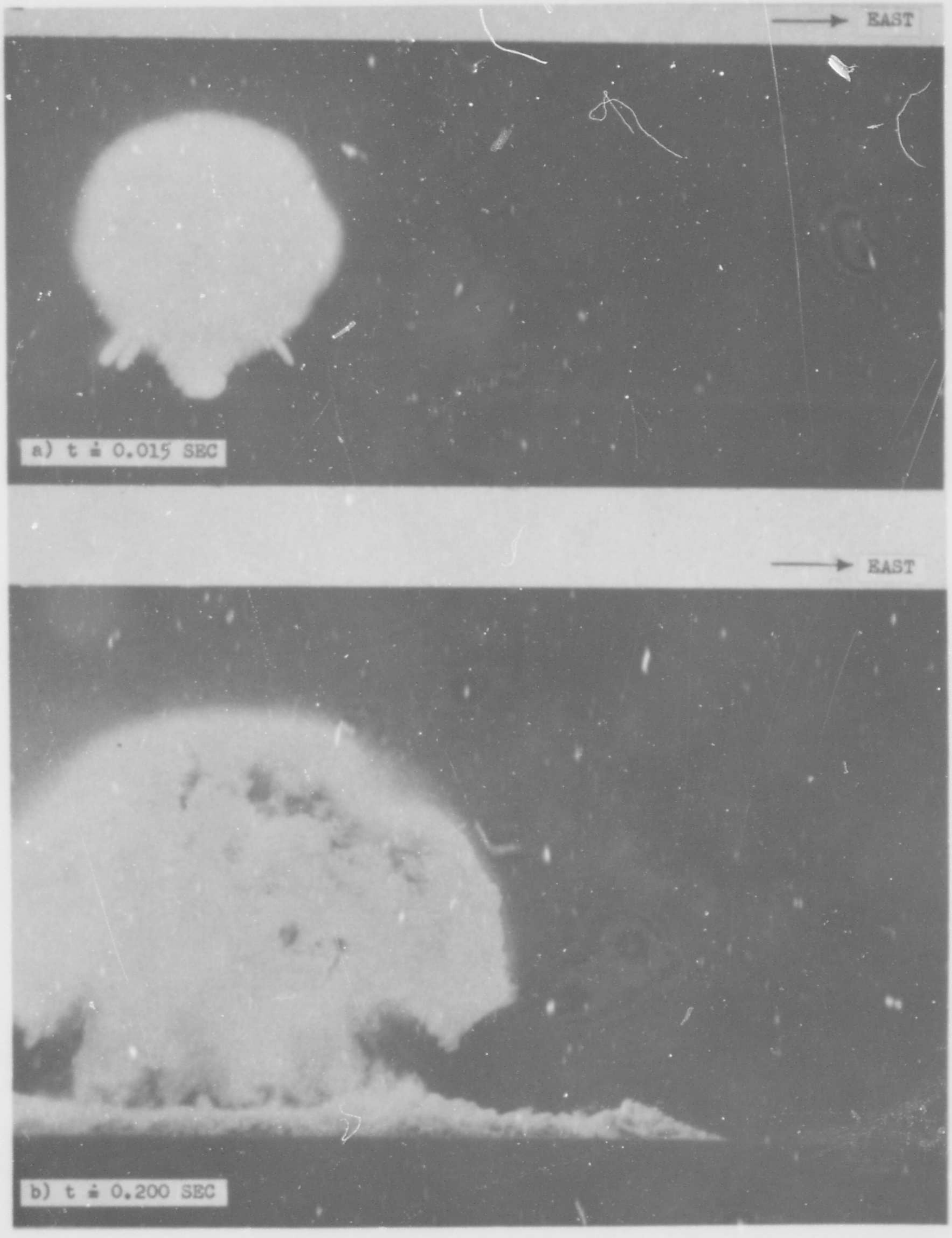

Figure 3.4 Shot 3, Photographs taken from Film 28681.

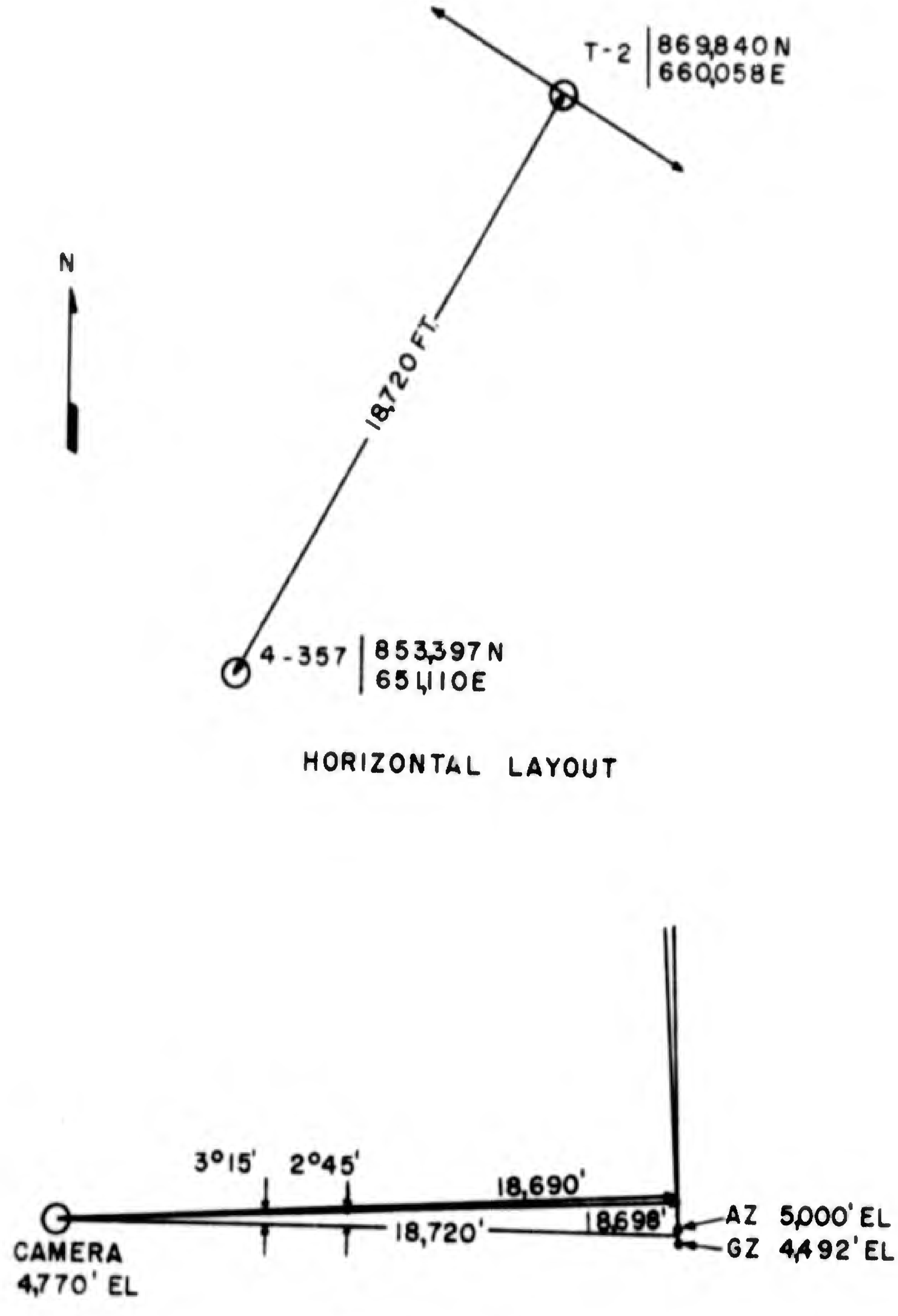

Figure 3.5 Shot 4, Planes of Measurement for Smoke Rocket Photography.

[redacted]

TABLE 3.2 Shot 4 - Absolute Time of Arrival of Incident Shock in Free Air

Distance From Burst (ft)	Time (Sec)	Distance From Burst (ft)	Time (Sec)	Distance From Burst (ft)	Time (Sec)
		Film 28183			
188.698	.002580	1357.574	.279780	1926.288	.556980
347.256	.012480	1379.851	.289680	1944.634	.566880
441.605	.022380	1400.818	.299580	1956.427	.576780
511.056	.032280	1427.026	.309480	1976.083	.586680
581.818	.042180	1451.923	.319380	1994.429	.596580
632.973	.052080	1474.200	.329280	2014.085	.606480
677.477	.061980	1489.925	.339180	2031.120	.616380
724.651	.071880	1512.202	.349080	2052.086	.626280
770.515	.081780	1533.168	.358980	2067.811	.636180
808.517	.091680	1556.755	.368880	2083.536	.646080
851.760	.101580	1576.411	.378780	2103.192	.655980
889.762	.111480	1596.067	.388680	2120.227	.665880
914.659	.121380	1614.413	.398580	2139.883	.675780
951.350	.131280	1634.069	.408480	2154.298	.685680
986.731	.141180	1655.035	.418380	2195.747	.705480
1016.870	.151080	1674.691	.428280	2217.197	.725280
1048.320	.160980	1695.658	.438180	2251.267	.745080
1078.459	.170880	1711.382	.448080	2284.027	.764880
1109.909	.180780	1731.038	.457980	2318.098	.784680
1141.358	.190680	1752.005	.467880	2357.410	.804480
1166.256	.200580	1772.971	.477780	2380.997	.824280
1188.533	.210480	1793.938	.487680	2409.826	.844080
1213.430	.220380	1816.214	.497580	2441.275	.863880
1238.328	.230280	1829.318	.507480	2475.346	.883680
1259.294	.240180	1848.994	.517380	2509.416	.903480
1284.192	.250080	1869.942	.527280	2539.555	.923280
1302.538	.259980	1889.597	.537180	2567.074	.943080
1331.366	.269880	1906.632	.547080	2601.144	.962880
				2629.973	.982680

Distance From Burst (ft)	Time (Sec)	Distance From Burst (ft)	Time (Sec)	Distance From Burst (ft)	Time (Sec)
		Film 28184			
321.618	.009950	1760.130	.464450	2695.748	1.009850
426.875	.020050	1797.165	.484650	2726.935	1.030050
506.793	.030150	1838.098	.504850	2762.021	1.050250
688.069	.060450	1880.981	.525050	2793.208	1.070450
729.002	.070550	1919.965	.545250	2826.344	1.090650
783.580	.080650	1957.000	.565450	2847.786	1.110850
822.564	.090750	1988.187	.585650	2875.074	1.131050
851.801	.100850	2031.070	.605850	2904.312	1.151250
892.735	.110950	2062.257	.626050	2935.500	1.171450
935.617	.121050	2099.298	.646250	2962.789	1.191650
970.703	.131150	2138.276	.666450	2992.027	1.211850
1003.840	.141250	2169.463	.686650		
1036.976	.151350	2202.599	.706850		
1068.163	.161450	2237.685	.727050		
1122.741	.181650	2274.720	.747250		
1189.014	.201850	2300.060	.767450		
1233.845	.222050	2333.200	.787650		
1282.576	.242250	2364.383	.807850		
1339.102	.262450	2401.418	.828050		
1387.833	.282650	2436.504	.848250		
1430.715	.302850	2465.742	.868450		
1481.394	.323050	2483.285	.878550		
1520.378	.343250	2512.523	.898750		
1559.362	.363450	2532.015	.908850		
1600.296	.383650	2563.202	.929050		
1641.729	.403850	2596.338	.949250		
1682.162	.424050	2631.424	.969450		
1721.146	.444250	2668.459	.989650		

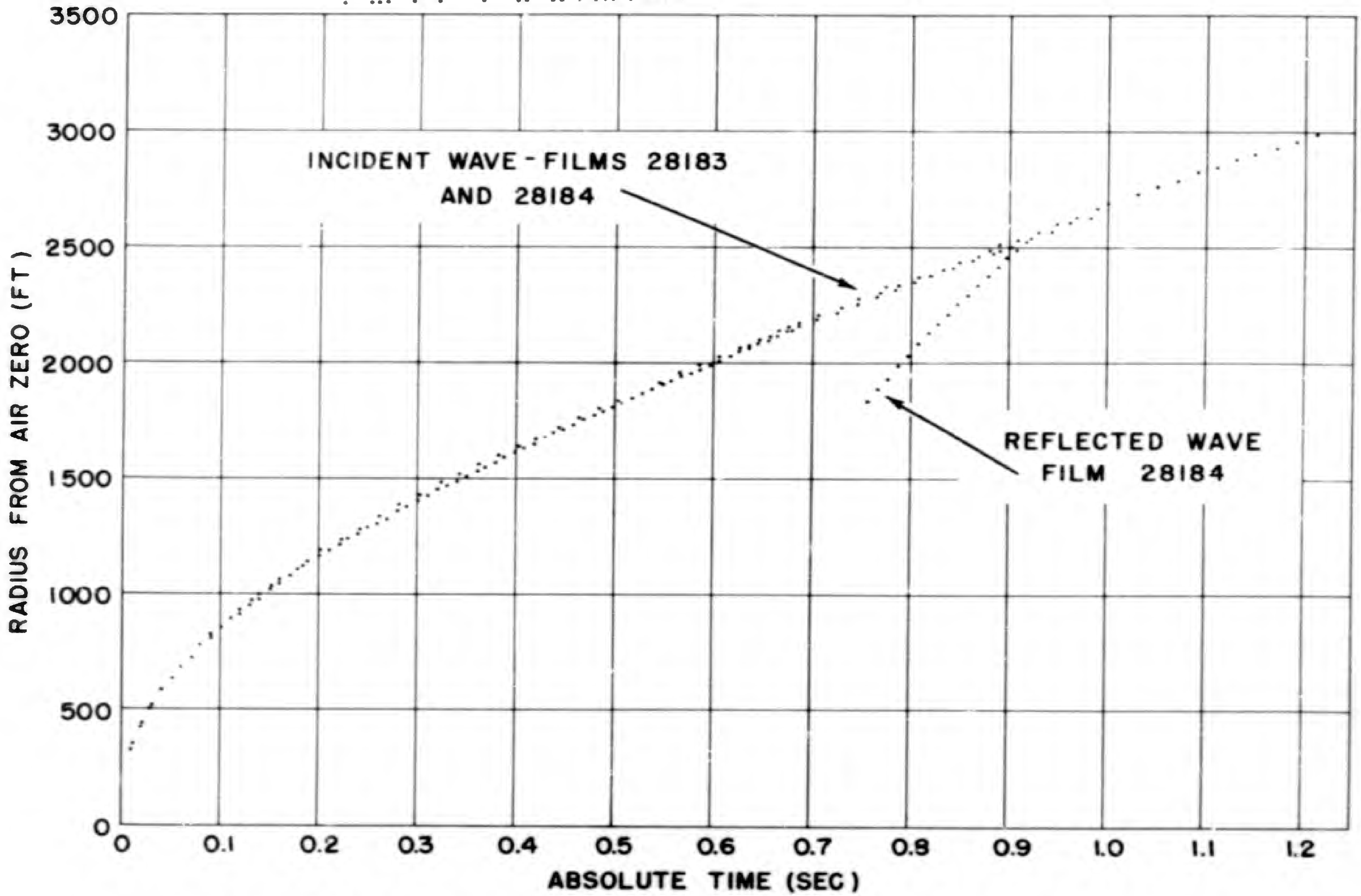

Figure 3.6 Shot 4, Time of Arrival of Free-Air Shock in Vertical Direction.

[redacted]

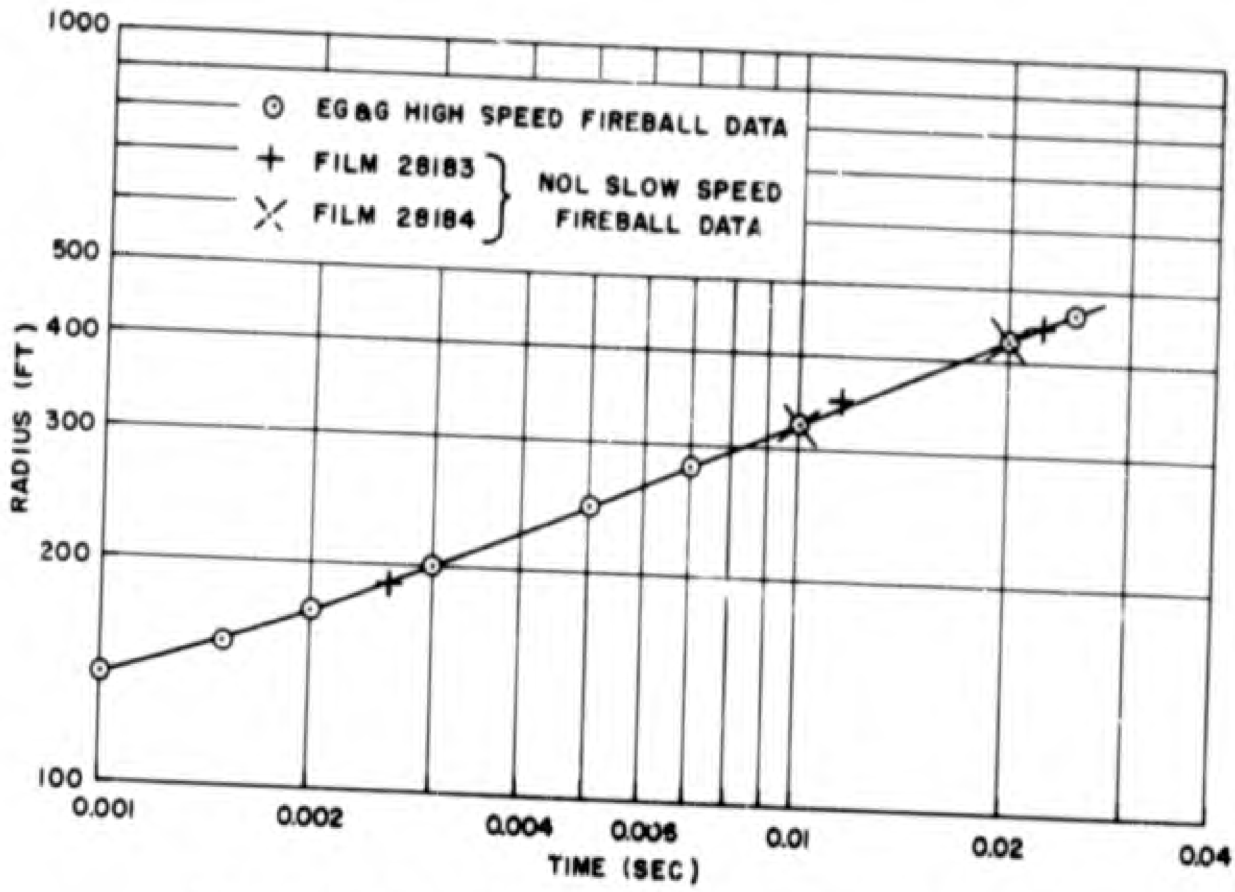

Figure 3.7 Shot 4, Fireball Radius versus Time.

and the resulting constants to be substituted into this equation were found to be as follows:

$a = 1{,}090.865$

$b = 1{,}507.918$

$c = 0.004585$

These constants are valid over the entire range of from 600 to 3,000 ft.

The instantaneous shock velocities were then obtained by substitution of the constants a and b into Equation 1.2 and the velocities were calculated from

$$U = 1090.9 \left[1 + \left(\frac{1507.9}{R} \right)^{1.5} \right] \tag{3.1}$$

where R is given in feet and U is given in ft/sec. Figure 3.8 is a plot of the velocities as a function of distance. By substitution of these velocities in the Rankine-Hugoniot equation, Equation 1.3, the peak shock overpressures were calculated as a function of distance.

Since the free-air arrival-time data were measured in the vertical direction only, it was necessary to use the varying ambient atmospheric conditions ahead of the shock for each radius at which pressures were calculated. Measurements of P_o and T_o (ambient pressure and temperature) were made at various altitudes. C_o, the sound velocity, was calculated by substituting the value of T_o in the equation for the sound velocity given in Section 1.2 following Equation 1.3. Fig. 3.9 is a plot of P_o and C_o as a function of altitude and the ambient conditions ahead of the shock were determined from this plot. The peak overpressures, instan-

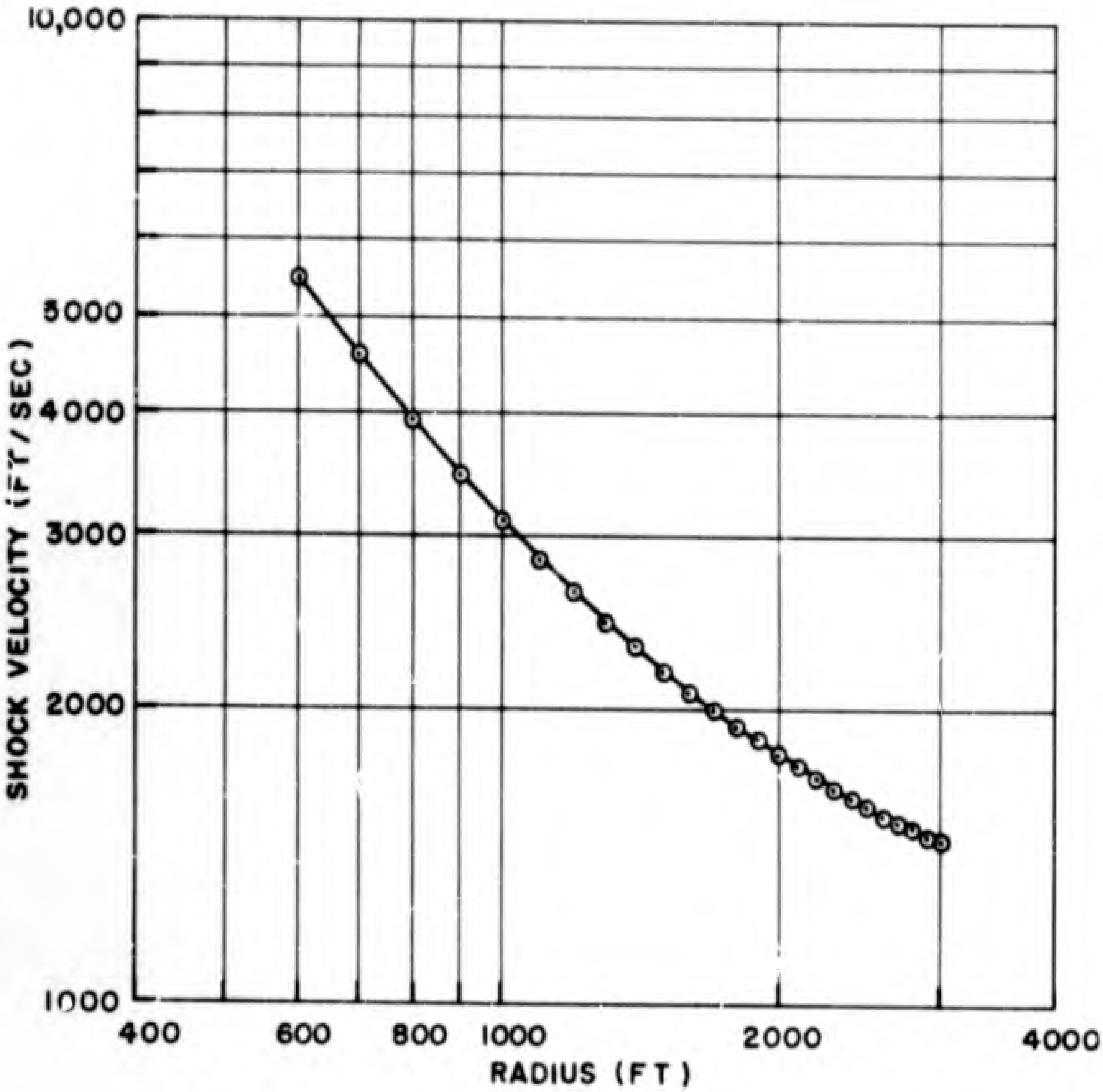

Figure 3.8 Shot 4, Free-Air Shock Velocity versus Distance.

taneous shock velocities, distances, and the ambient conditions (P_o and C_o), for Shot 4 are given in Table 3.3. Fig. 3.10 is a plot of the peak shock overpressures as a function of distance from the weapon.

One project objective on Shot 4, it will be recalled, was to determine whether the incident and reflected shock waves coalesced above the burst. While the records were being examined to obtain the incident

TABLE 3.3 Shot 4 - Pressure, Velocity, Distance Data in Free Air

Distance R (ft)	Shock Velocity U(ft/sec)	Sound Velocity C_o(ft/sec)	Ambient Pressure P_o(psi)	Shock Over-Pressure P_s(psi)
600	5,437.1	1,099.8	12.10	347.3
700	4,539.8	1,099.6	12.07	236.6
800	3,913.8	1,099.4	12.02	168.3
900	3,456.6	1,099.2	11.98	127.0
1,000	3,110.8	1,099.0	11.94	99.1
1,100	2,841.7	1,098.8	11.89	79.7
1,200	2,627.5	1,098.6	11.85	66.4
1,300	2,453.6	1,098.5	11.80	55.5
1,400	2,310.3	1,098.3	11.76	46.9
1,500	2,190.4	1,098.1	11.72	40.8
1,600	2,088.9	1,098.0	11.67	35.7
1,700	2,002.2	1,097.8	11.63	31.6
1,800	1,927.3	1,097.6	11.59	28.1
1,900	1,862.1	1,097.5	11.55	25.3
2,000	1,805.0	1,097.3	11.51	23.0
2,100	1,754.6	1,097.2	11.47	20.9
2,200	1,709.9	1,097.0	11.42	19.1
2,300	1,670.0	1,096.9	11.39	17.5
2,400	1,634.1	1,096.7	11.35	16.2
2,500	1,601.9	1,096.6	11.31	14.9
2,600	1,572.7	1,096.5	11.27	13.9
2,700	1,546.2	1,096.3	11.23	13.0
2,800	1,522.0	1,096.2	11.19	12.1
2,900	1,500.0	1,096.0	11.16	11.3
3,000	1,479.6	1,095.9	11.12	10.6

shock data, the position of the reflected wave was sought without success. Notice of a slight jog in the incident wave arrival-time curve at approximately 2,550 ft finally led to the detection of what is thought to have been the reflected wave. Arrival-time data for this wave were obtained over the range from 1,800 to 2,525 ft vertically

TABLE 3.4 - Shot 4 - Absolute Time of Arrival of Reflected Shock in Free Air

Distance From Burst (ft)	Time (sec)
Film 28184	
1,836.149	0.757350
1,882.930	0.767450
1,929.711	0.777550
1,988.187	0.787650
2,036.917	0.797750
2,087.596	0.807850
2,134.377	0.817950
2,173.361	0.828050
2,214.295	0.838150
2,259.126	0.848250
2,294.212	0.858350
2,333.196	0.868450
2,374.129	0.878550
2,424.809	0.888650
2,459.894	0.898750
2,491.081	0.908850
2,524.218	0.918950

above the burst. These data are given in Table 3.4 and are plotted in Fig. 3.6. Somewhere between 2,525 and 2,550 ft, the incident and reflected waves apparently coalesced over a horizontal range of approximately 750 ft to either side of the vertical through the burst point. Beyond the 2,525 ft distance, only one wave could be detected.

Although it was difficult to detect the reflected wave above the fireball, the lower portions in the vicinity of the triple point could be seen distinctly. It was found possible to trace nearly the entire outline of the reflected wave from the triple point on one side of the burst to that on the other. (The rocket smoke grid proved to be of little use in locating the wave in the region above the burst.) The contour of the reflected wave is shown in Fig. 3.11 as it appeared at

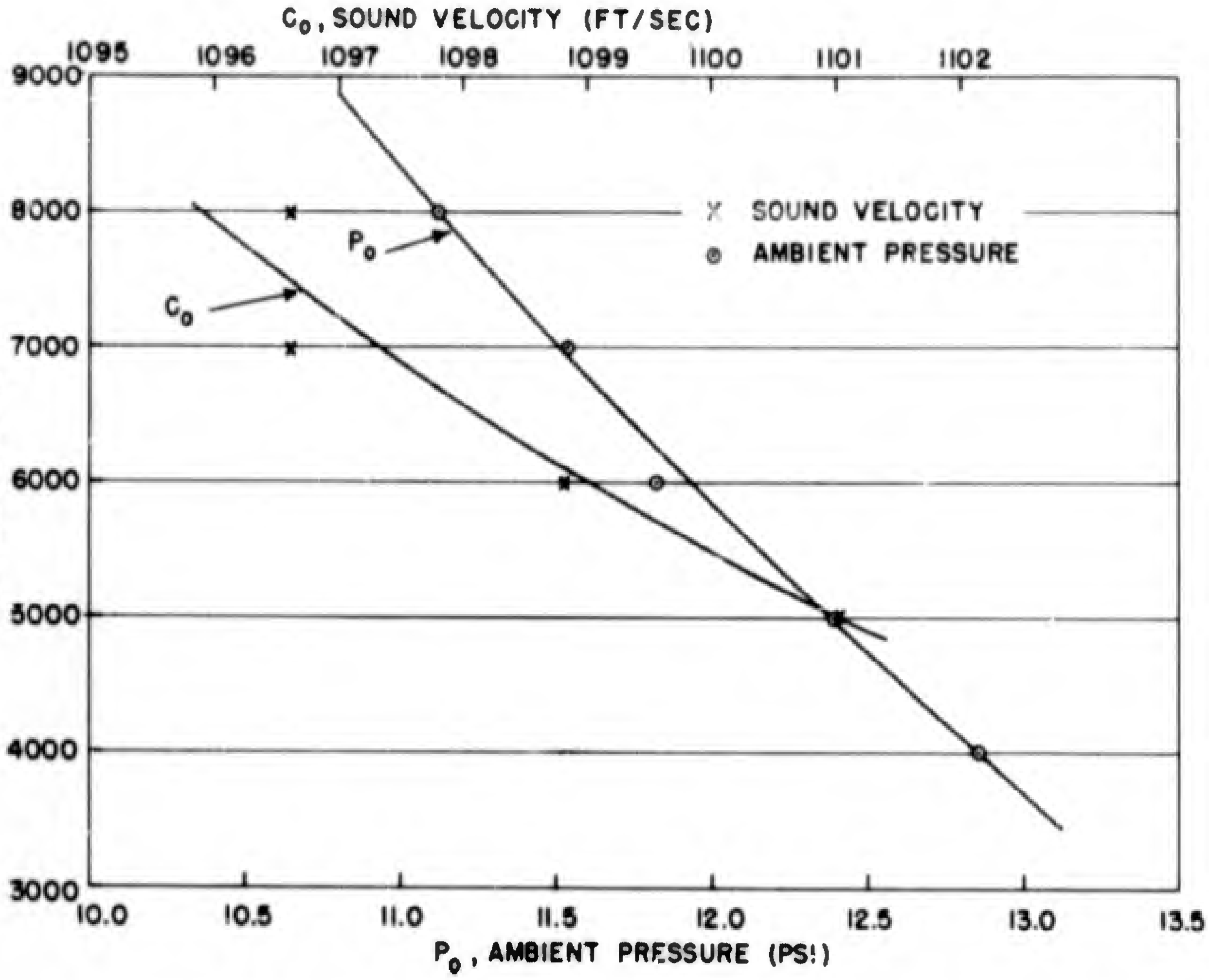

Figure 3.9 Shot 4, Sound Velocity and Ambient Pressure versus Altitude.

the time of coalescence. Fig. 3.12 shows a frame of the film record. Only the incident shock is outlined clearly by the smoke grid.

A perplexing observation that must be reported is that the reflected wave was found to travel with a velocity of from 3,500 to 4,000 ft/sec in overtaking the incident shock. A shock traveling with this velocity in the medium believed to exist behind the incident shock would be expected to have a peak overpressure in excess of 100 psi, according to theory. Yet all other evidence indicates that such a strong shock was not present. For example, no definite hooks or breaks were observed in the smoke grid other than those caused by the incident wave. Also, at the distance corresponding to that at which coalescence is indicated, the incident shock pressure was only about 12 psi. The

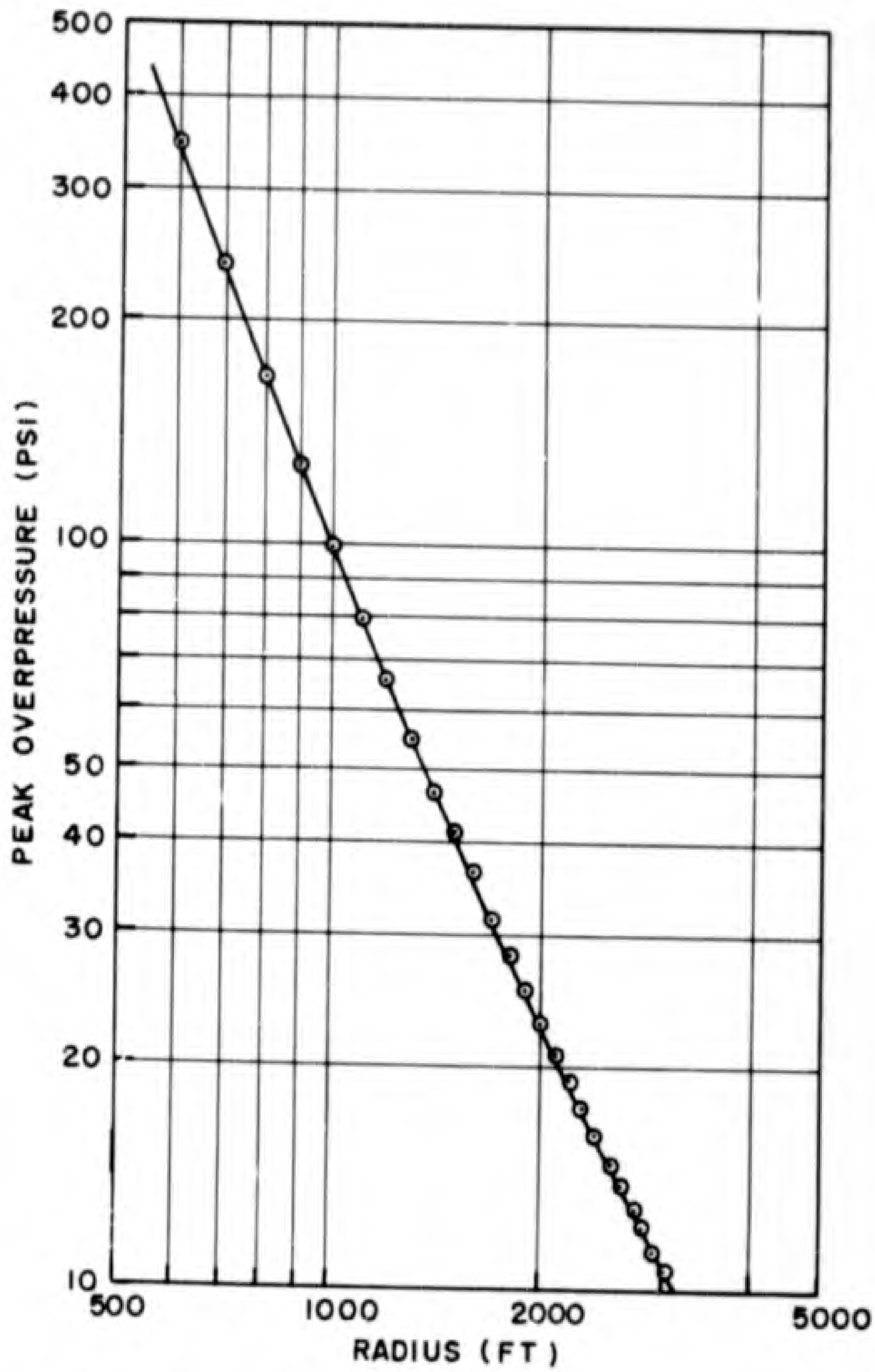

Figure 3.10 Shot 4, Free-Air Peak Shock Overpressure versus Distance.

overtaking of such a comparatively weak shock by one about eight times as strong would have resulted in a marked increase in the velocity of the coalesced front, but no such radical jump that would indicate a large velocity increase appeared in the arrival-time data. Finally, only weak reflected wave pressures were recorded by the canister gages of Project 1.1 (Air Force Cambridge Research Center). The fact that these measurements were made where the incident shock was of the order

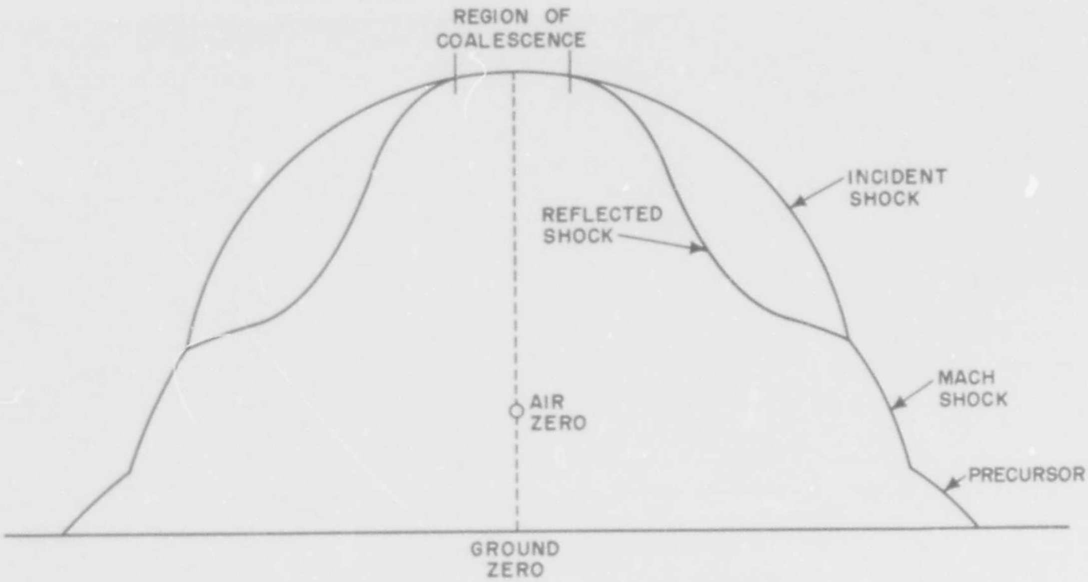

Figure 3.11 Incident and Reflected Wave Contours.

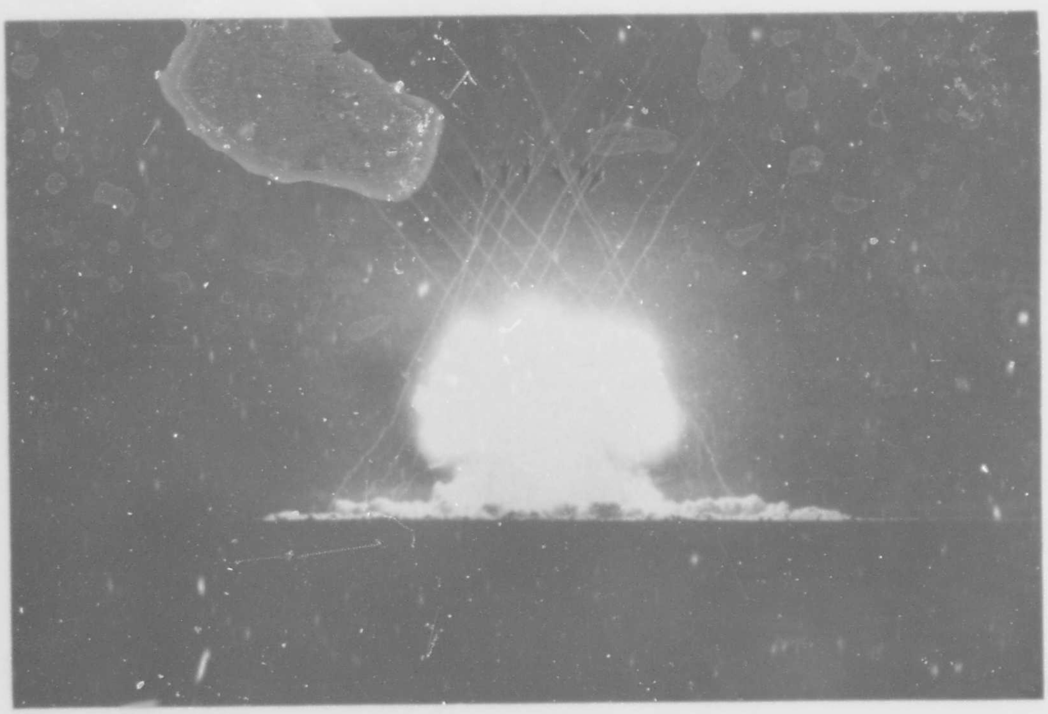

Figure 3.12 Shot 4, Photograph of Free-Air Incident Shock
2,290 ft from Air Zero at t = 0.757 sec (Film 28184).

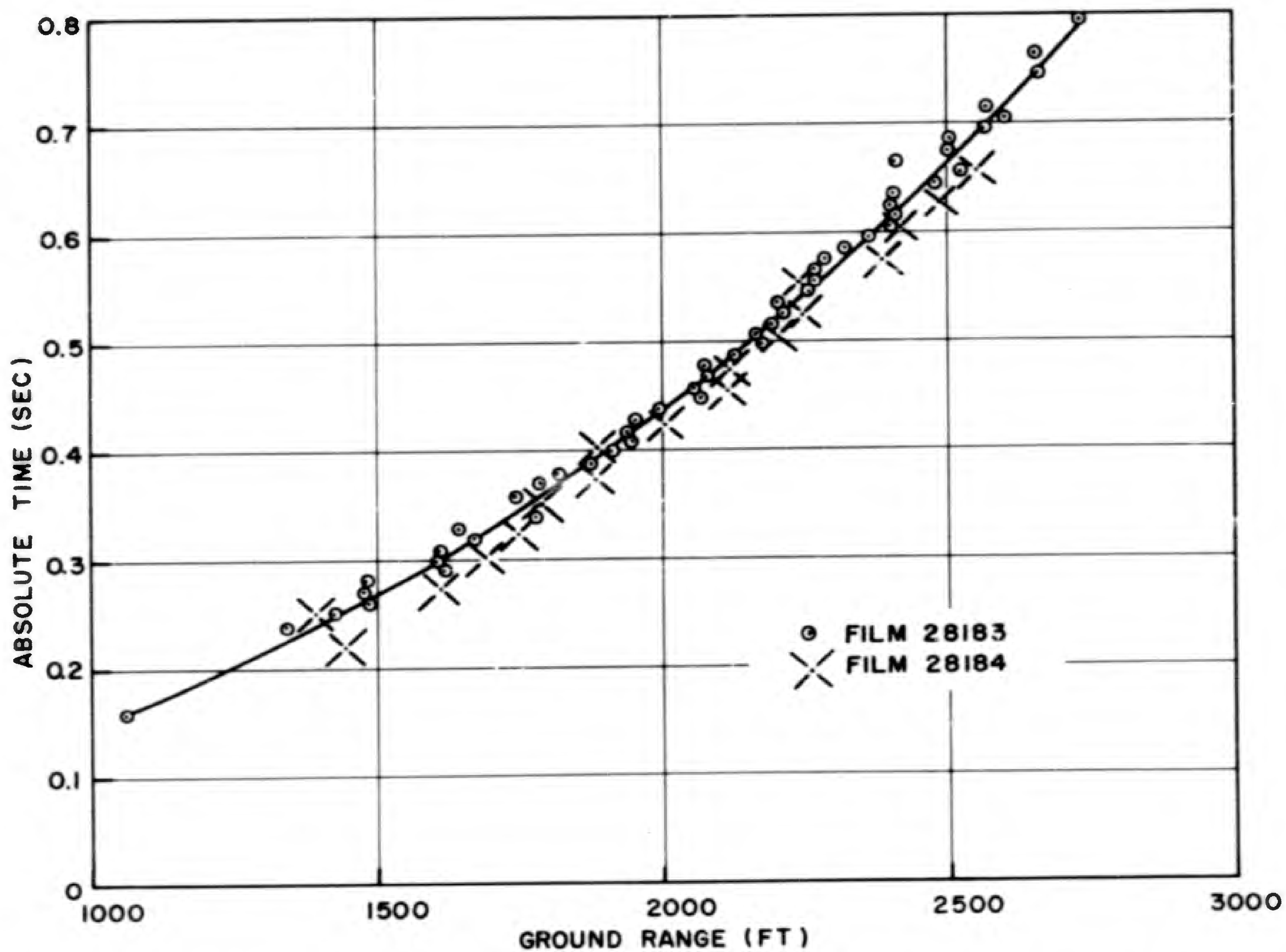

Figure 3.14 Shot 4, Time of Arrival of Precursor at Ground Level (Southeast of GZ).

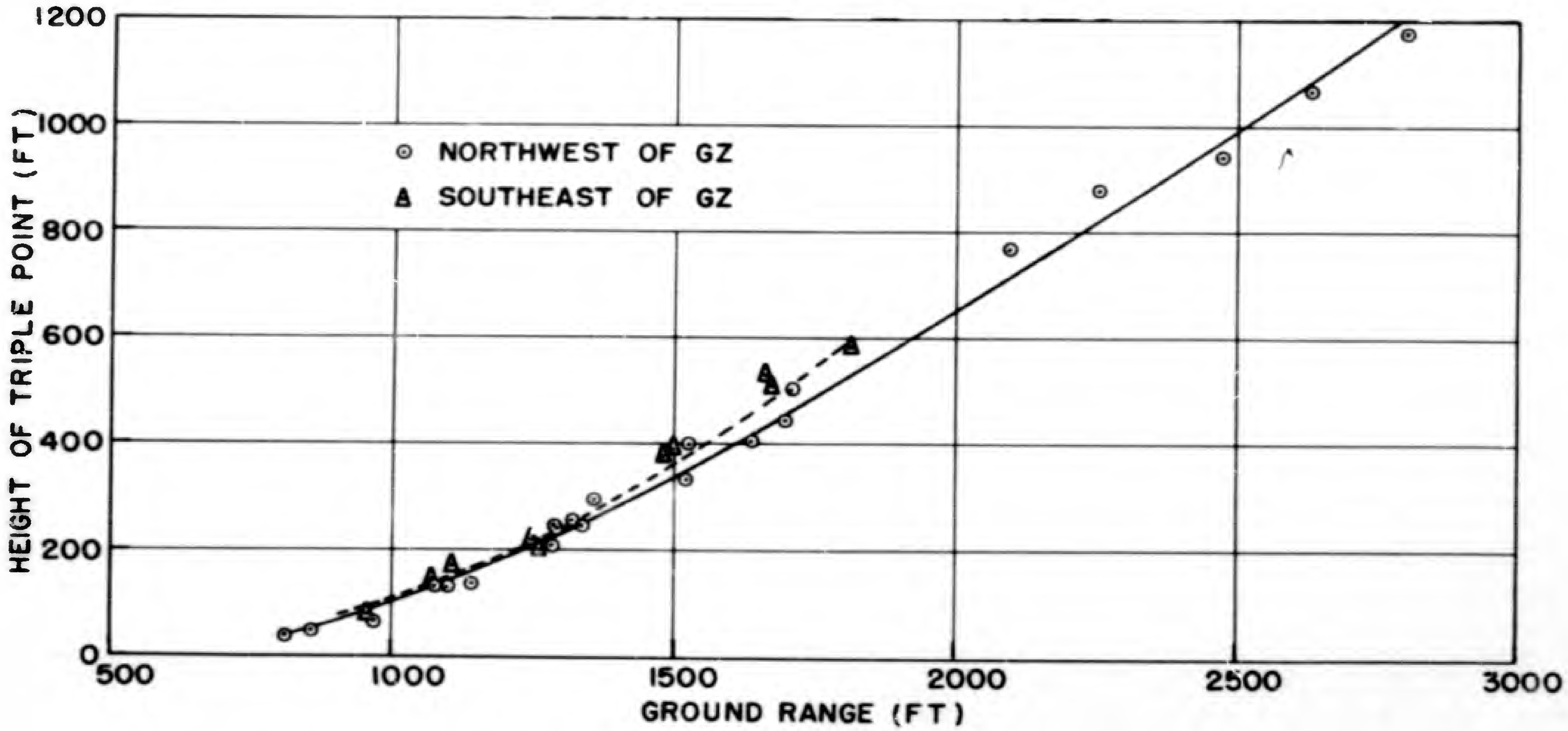

Figure 3.15 Shot 4, Height of the Triple Point as a Function of Ground Range (Northwest and Southeast of GZ).

of 9 psi and below, as well as being located off to the side of the burst rather than directly above it, has little bearing on the argument.

No solution to this apparent paradox has been found to date. All that can be said is that if the reflected wave front observed optically was real, for which the evidence is strong, then the assumptions made concerning the conditions believed to exist behind the incident shock were in error. There is no other source of error which would account for the difference between the calculations and the observations. For practical purposes it must be concluded that the calculated reflected wave pressures are in error.

The second purpose of the project was to determine the value of the peak overpressure in the coalesced wave; and further, to predict what the peak overpressure in the coalesced wave would be on the similarly oriented Shot 12. The incident shock pressures beyond the 2,550 ft distance, presented above, are to be considered as those for the coalesced wave.

To predict what pressures one might expect, following coalescence, for another energy yield, such as for that of Shot 12, it was decided to determine what increase in the yield of Shot 4 would have been required to give the same incident shock arrival times and pressures as those observed on Shot 4 after coalescence. An average value for this supposed yield was obtained by comparing the Shot 4 arrival-time and pressure-distance data point by point, with those of the corresponding composite free-air curves (Ref. 6) for a 1-KT device at sea level and averaging the results.

First, the Shot 4 arrival-time data were scaled down from assumed yields between 45 and 50 KT until the composite arrival-time data were bracketed. Then by extrapolation and a series of approximations, the apparent yield of the Shot 4 weapon was obtained for various distances from air zero. Table 3.5 lists the yields obtained in this manner.

The pressure-distance data were scaled to sea level and compared with the composite pressure-distance curve in a similar fashion. Distances for the same pressure level, from Shot 4 and the composite pressure-distance curve were found, and with the relation

$$\frac{W_2}{W_1} = \left(\frac{R_2}{R_1}\right)^3$$

where,

W_1 = 1 KT,

R_1 = distance read from composite curve for a given pressure

W_2 = yield for the Shot 4 weapon at that pressure level

R_2 = distance read from the Shot 4 pressure-distance curve, same pressure level

the apparent yield for Shot 4 was found. These data are also given in Table 3.5. Figure 3.13 is a plot of the yields obtained by both methods. From this analysis it was concluded that after coalescence occurred, the

TABLE 3.5 - Shot 4 - Weapon Yield Obtained From Free-Air Data

Yield Obtained From Pressure-Distance Data		Yield Obtained From Time-of-Arrival Data	
Distance From Burst (ft)	Weapon Yield (kt)	Distance From Burst (ft)	Weapon Yield (kt)
610	39.4	507	42
688	40.6	688	46
810	43.6	729	50
1,095	45.8	1,068	46
1,205	46.9	1,123	46
1,390	48.0	1,600	44
1,690	49.8	1,988	44
2,450	52.0	2,202	45
2,900	54.2	2,300	45
		2,512	46
		2,696	46
		2,793	46
		2,904	46
		2,992	45

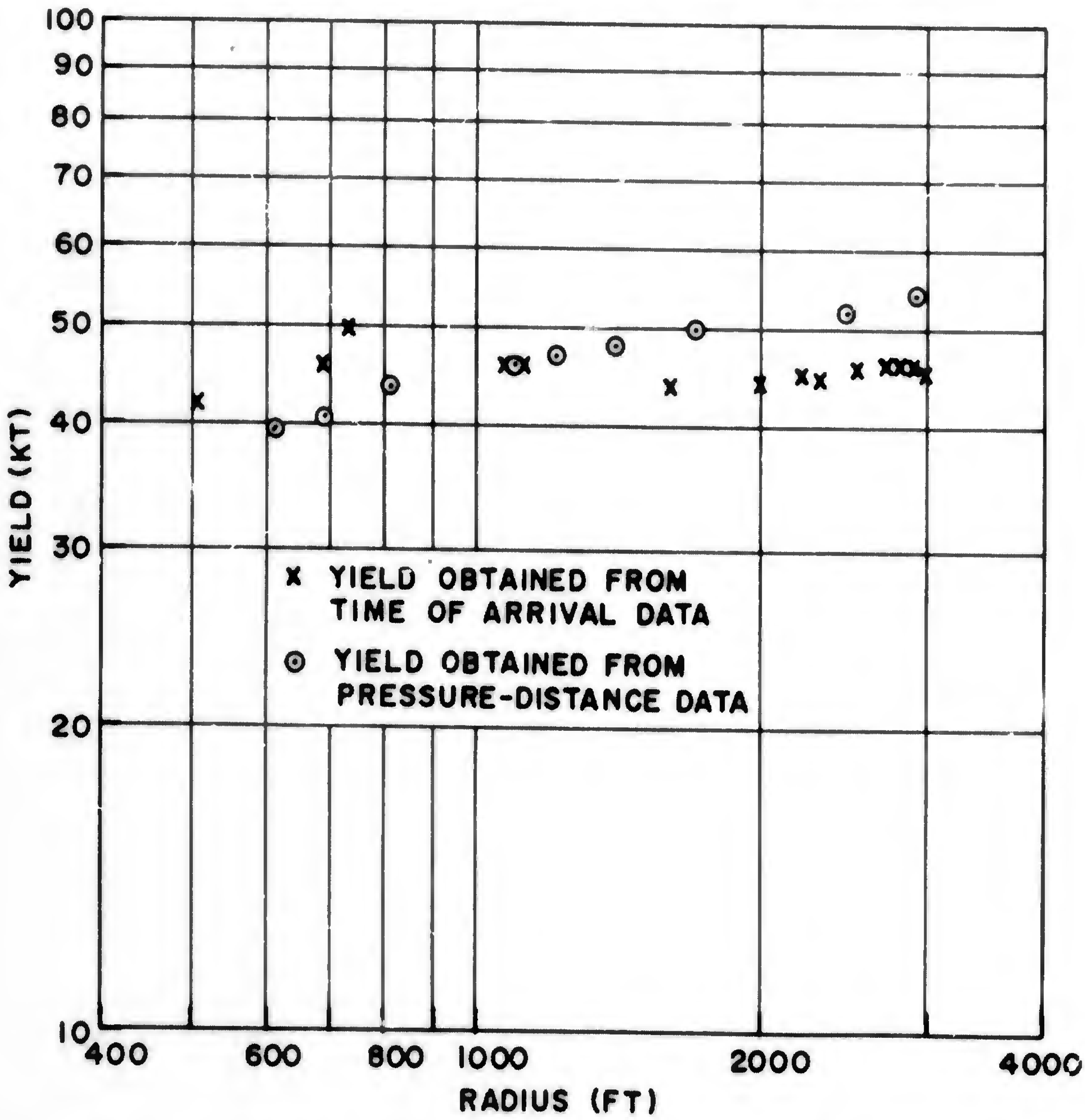

Figure 3.13 Shot 4, Weapon Yield as a Function of Distance from Burst Point.

[redacted]

coalesced wave corresponded to that which would have been produced normally at the same distance from a yield of 1.16 W, i.e., from a weapon yield of 1.16 x 43 = 49.9 KT, prior to coalescence.

Measurements of the shock phenomena occurring near the ground were also made to a limited extent. These data contained a much larger uncertainty than is generally realized when the photo-optical technique of direct shock photography is planned for in advance. On Shot 4 the experiment was designed primarily to obtain free-air data. Furthermore, a rise in the foreground between the camera and ground zero obstructed the view of the area in the vicinity of ground zero on both sides, particularly to the northwest side of ground zero (see Fig. 3.12). As a result, all measurements made at ground level had to be extrapolated to that surface.

The time of arrival of the precursor formed on Shot 4 was measured to the southeast of ground zero. These data are given in Table 3.6 and plotted in Fig. 3.14. Only fragmentary precursor data could be obtained on the northwest side of ground zero, because of the obstruction in the foreground.

The height of the triple point as a function of ground range is given in Table 3.7 and plotted in Fig. 3.15. Measurements were made on both sides of ground zero and extended out to a ground range of approximately 2,800 ft on the northwest side of ground zero and 1,800 ft on the southeast side. The smoke grid produced for the free-air measurements formed a background grid in the field of view of two cameras aimed from Station 372 and extended the useful field of view in which the triple point could be detected by approximately 1,000 ft on the northwest side of ground zero. All measurements of the triple point trajectory have been assigned an uncertainty of ± 5 percent.

3.4 SHOT 6

Excellent results were obtained from the direct shock photography films on this shot. Along with the shock phenomena occurring near the ground, a high-speed jet was observed to blow out of opposite sides of the fireball. Figure 3.17(a) shows this jet just after its appearance. The velocity of the jet was extremely high (faster than the shock just after breakaway) and ranged from approximately 12,000 to 5,000 ft/sec over a distance of from 500 to 900 ft from the center of burst. Figure 3.18 is a plot of the arrival time of the most-extended portion of the jet and the front of the immense cloud of gases, both of which were propagating faster than the free-air shock. Since the jet was symmetrical about the center of the Shot 6 detonation, it was attributed to the internal geometry and method of detonation of the weapon.

A precursor was formed over the desert and asphalt areas, and arrival-time data were measured from Films 28081 and 28084. Figure 3.16 shows the plane of measurement for both films. These data are given in Table 3.8 and plotted in Fig. 3.19. The precursor over the asphalt area was markedly different from that formed over the desert area. Figure

(Continued on Page 52)

[redacted]

TABLE 3.6 - Shot 4 - Time of Arrival of Precursor Along Ground Southeast of Ground Zero

Ground Range (ft)	Time (Sec)	Ground Range (ft)	Time (Sec)	Ground Range (ft)	Time (Sec)	Ground Range (ft)	Time (Sec)
		Film 28183				Film 28184	
1055	.16098	1943	.40848	2319	.58668	1442	.22205
1339	.24018	1935	.41838	2359	.59658	1388	.25235
1422	.25008	1952	.42828	2399	.60648	1608	.27255
1483	.25998	1993	.43818	2407	.61638	1686	.30285
1472	.26998	2064	.44808	2398	.62628	1742	.32305
1474	.27978	2052	.45798	2403	.63618	1784	.35335
1614	.28968	2076	.46788	2474	.64608	1881	.37355
1601	.29958	2072	.47778	2521	.65598	1885	.40385
1603	.30948	2123	.48768	2407	.66588	2066	.42405
1667	.31938	2169	.49758	2496	.67578	2113	.45435
1638	.32928	2162	.50748	2503	.68568	2154	.47455
1776	.33918	2188	.51738	2562	.69558	2202	.50485
1748	.34908	2208	.52728	2597	.70548	2244	.52505
1739	.35898	2201	.53718	2567	.71538	2339	.55535
1785	.36888	2254	.54708	2654	.74508	2382	.57555
1815	.37878	2267	.55698	2656	.75498	2417	.60585
1869	.38868	2268	.56688	2652	.76488	2485	.62605
1908	.39858	2284	.57688	2728	.79458	2557	.65635

TABLE 3.7 - Shot 4 - Height of the Triple Point as a Function of Ground Range Northwest and Southeast of Ground Zero

Ground Range (ft)	Height (ft)	Ground Range (ft)	Height (ft)
Northwest		Southeast	
805	43.6	951	80.4
852	53.1	1,068	138.5
961	76.5	1,104	176.2
1,071	132.9	1,246	224.2
1,097	131.8	1,[illegible]	201.7
1,140	140.9	1,[illegible]	386.4
1,280	211.0	1,498	397.5
1,283	244.7	1,659	528.9
1,288	246.7	1,672	505.2
1,317	259.0	1,811	581.6
1,334	248.0		
1,357	297.6		
1,522	336.3		
1,524	399.4		
1,635	406.3		
1,696	440.5		
1,708	503.2		
2,093	767.6		
2,252	877.7		
2,473	942.2		
2,633	1,066.5		
2,803	1,171.9		

[redacted]

Figure 3.16 Shot 6, Plane of Measurement for Direct Shock Photography Films 28081 and 28084.

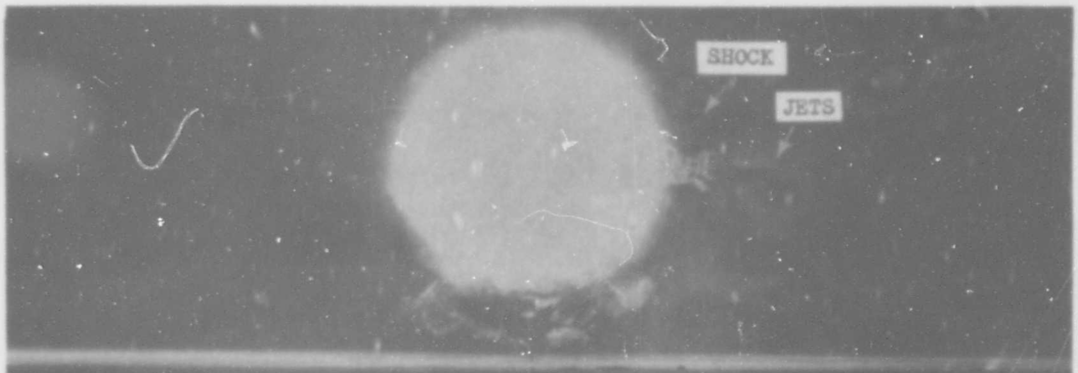

a) RADIUS OF FREE-AIR SHOCK = 486 FT; t = 0.058 SEC

b) t = 0.197 SEC

Figure 3.17 Shot 6, Photographs of Blast Phenomena (Film 28081).

[redacted]

3.17(b) shows the precursor formed over both areas. The angle which the front of the desert precursor made with the surface was greater and its velocity along the ground less than the corresponding values for the precursor over the asphalt. This difference in velocity of the precursor fronts is readily observable in the arrival-time curves shown in Fig.

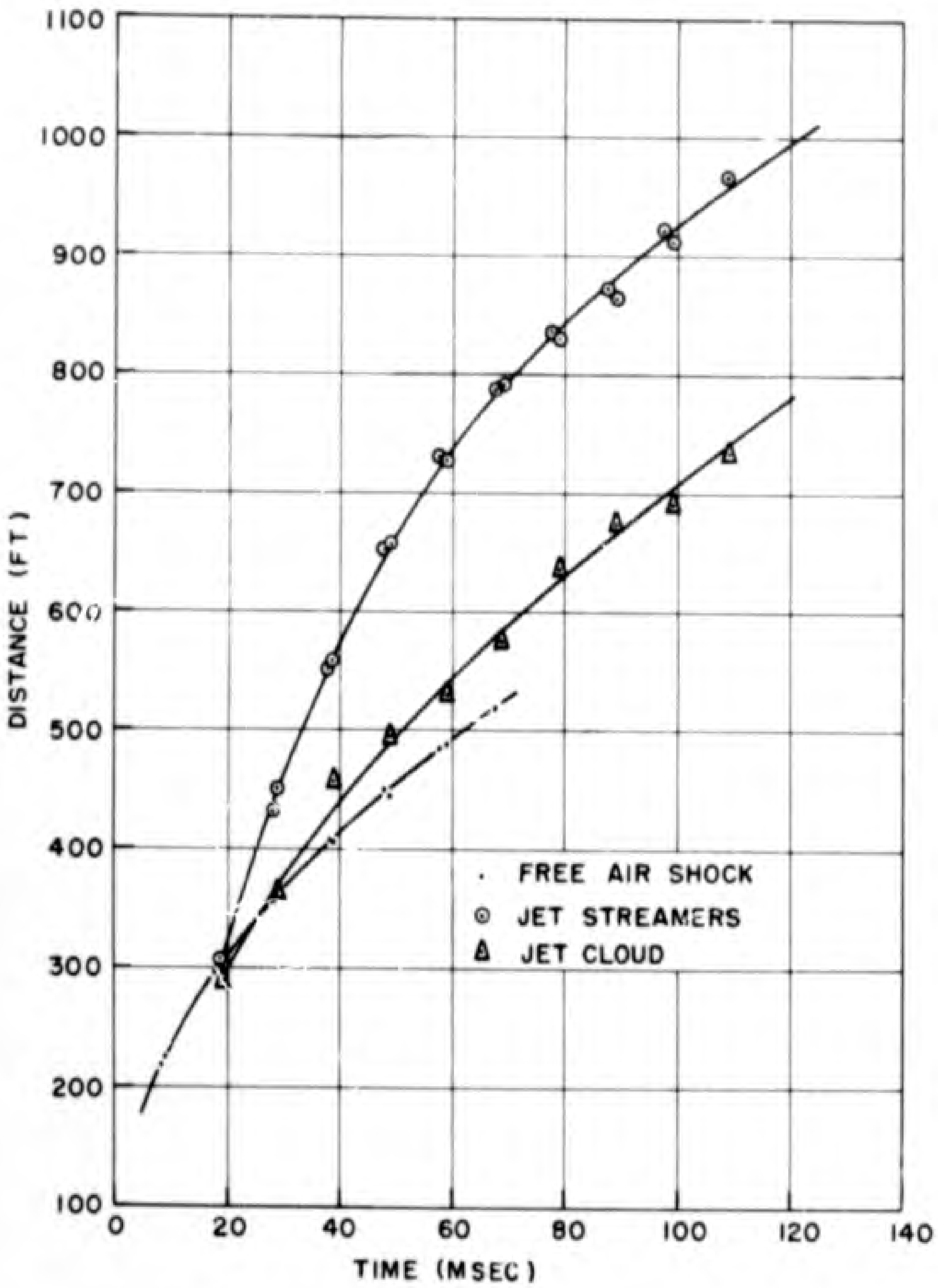

Figure 3.18 Shot 6, Time of Arrival of Fireball Jets.

3.19. The angle that the precursor front made with the surface over both areas was also measured and is plotted as a function of ground range in Fig. 3.20 and given in Table 3.9.

The triple-point trajectory could only be measured over the desert area to a height of 250 ft. The dust rising behind the precursor over

[redacted]

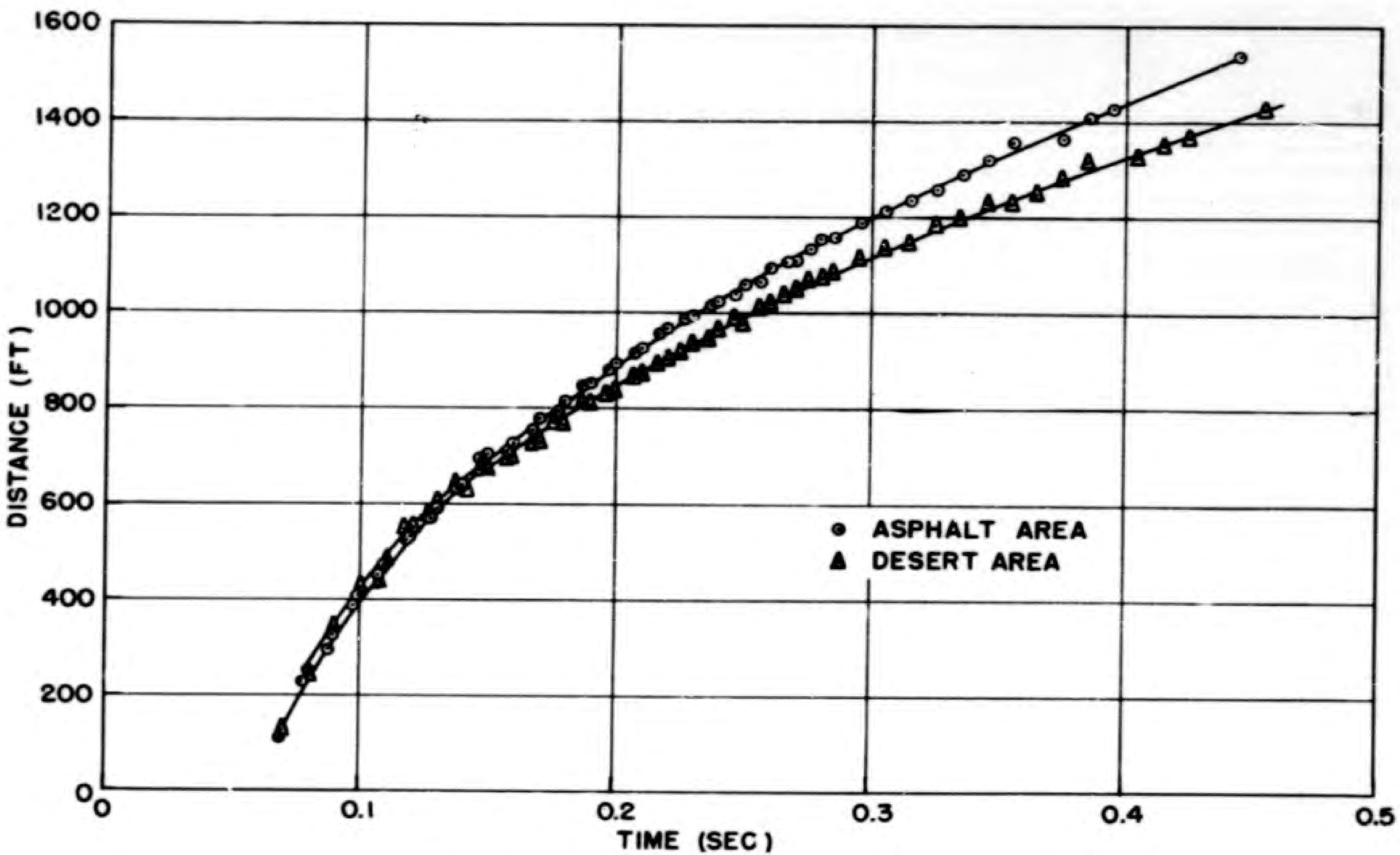

Figure 3.19 Shot 6, Time of Arrival of Precursor along the Ground over Asphalt and Desert Areas.

TABLE 3.8 - Shot 6, Time of Arrival of the Initial Disturbance Along the Ground

Asphalt Ground Range (ft)	Desert Ground Range (ft)	Time (sec)	Asphalt Ground Range (ft)	Desert Ground Range (ft)	Time (sec)
	Film 28081				
230.1	--	0.07774	1,426.1	--	0.39473
299.7	--	0.08765	--	1,329.1	0.40474
390.6	--	0.09755	--	1,349.8	0.41455
453.5	438.1	0.10746	--	1,371.2	0.42445
524.4	548.5	0.11737	1,534.4	--	0.44426
571.9	588.6	0.12727		1,426.8	[illegible]
635.4	638.8	0.13718			
699.0	678.9	0.14708		Film 28[illegible]4	
711.0	698.3	0.15699			
754.5	729.8	0.16690	111.1	125.2	0.06920
792.0	770.6	0.17680	253.8	248.3	0.07924
848.2	808.0	0.18671	328.9	342.4	0.08927
883.6	830.8	0.19661	408.0	424.5	0.09931
916.4	864.9	0.20652	473.6	479.1	0.10934
956.5	896.3	0.21643	531.6	550.7	0.11937
988.0	916.4	0.22633	593.2	606.7	0.12941
1,015.4	939.8	0.23624	641.3	630.8	0.13944
1,040.1	984.0	0.24614	708.8	675.8	0.14948
1,064.9	1,008.0	0.25605	727.9	700.8	0.15951
1,103.7	1,034.1	0.26596	776.9	733.4	0.16954
1,133.6	1,066.9	0.27586	816.0	768.4	0.17958
1,155.9	1,086.3	0.28577	856.0	807.0	0.18961
1,185.3	1,111.0	0.29567	897.6	837.5	0.19965
1,212.0	1,134.4	0.30558	925.6	870.5	0.20968
1,231.4	1,143.8	0.31549	968.7	901.1	0.21971
1,254.2	1,182.6	0.32539	995.2	932.1	0.22975
1,287.6	1,196.0	0.33530	1,024.2	965.2	0.23978
1,317.1	1,224.8	0.34520	1,059.3	978.7	0.24982
1,355.9	1,229.4	0.35511	1,073.8	1,020.7	0.25985
--	1,250.8	0.36502	1,107.8	1,044.2	0.26988
1,361.2	1,283.0	0.37492	1,154.4	1,068.8	0.27992
1,407.4	1,314.4	0.38483			

TABLE 3.9 - Shot 6, Angle of the Precursor as a Function of Ground Range Over Asphalt and Desert Areas

Ground Range (ft)	Angle (Degrees)	Ground Range (ft)	Angle (Degrees)
Desert Area		Asphalt Area	
438.1	32.7	453.5	21.9
548.5	17.0	524.4	15.7
588.6	24.3	571.9	19.0
638.8	22.1	635.4	17.2
678.9	22.3	699.0	14.0
698.3	24.3	711.0	27.3
729.8	26.0	754.5	24.0
770.6	29.0	792.0	25.2
808.0	27.1	848.2	21.0
830.8	28.5	883.6	20.5
864.9	29.8	916.4	21.3
896.3	29.2	956.5	22.0
916.4	30.8	988.0	23.0
939.8	34.3	1,015.4	24.0
984.0	30.6	1,040.1	25.5
1,008.0	32.0	1,064.9	26.6
1,034.1	33.6	1,103.7	27.0
1,066.9	34.3	1,133.8	27.8
1,086.3	34.3	1,155.9	28.4
1,111.0	37.1	1,185.3	28.6
1,134.4	38.8	1,212.0	29.8
1,143.8	43.9	1,231.4	30.9
1,182.6	38.4	1,254.2	32.5
1,196.0	42.5	1,287.6	31.5
1,224.8	39.0	1,317.1	31.3
1,229.4	46.0	1,355.9	30.8
1,250.8	53.4	1,361.2	32.5
1,283.0	46.8	1,407.4	32.8
1,314.4	40.5	1,426.1	35.0
1,329.1	56.5	1,534.4	40.5
1,349.8	57.0		
1,371.2	51.3		

[redacted]

the asphalt area obscured all shock formations near the ground. Figure 3.21 is a plot of the height of the triple point as a function of ground range over the desert, and these data are listed in Table 3.10.

3.5 SHOT 8

The arrival-time data for the free-air incident shock for this shot were measured in the vertical direction on Films 28282 and 28284. (See Fig. 3.22 for the planes of measurement for these films.) The photographic details for these films may be found in Table 2.2. Absolute time for the film records was again determined by plotting the first data point from the NOL films on the curve representing fireball-growth data supplied by EG&G (see Fig. 3.23). The arrival-time data are plotted in Fig. 3.24 and listed in Table 3.11. The statistical fit to the arrival-

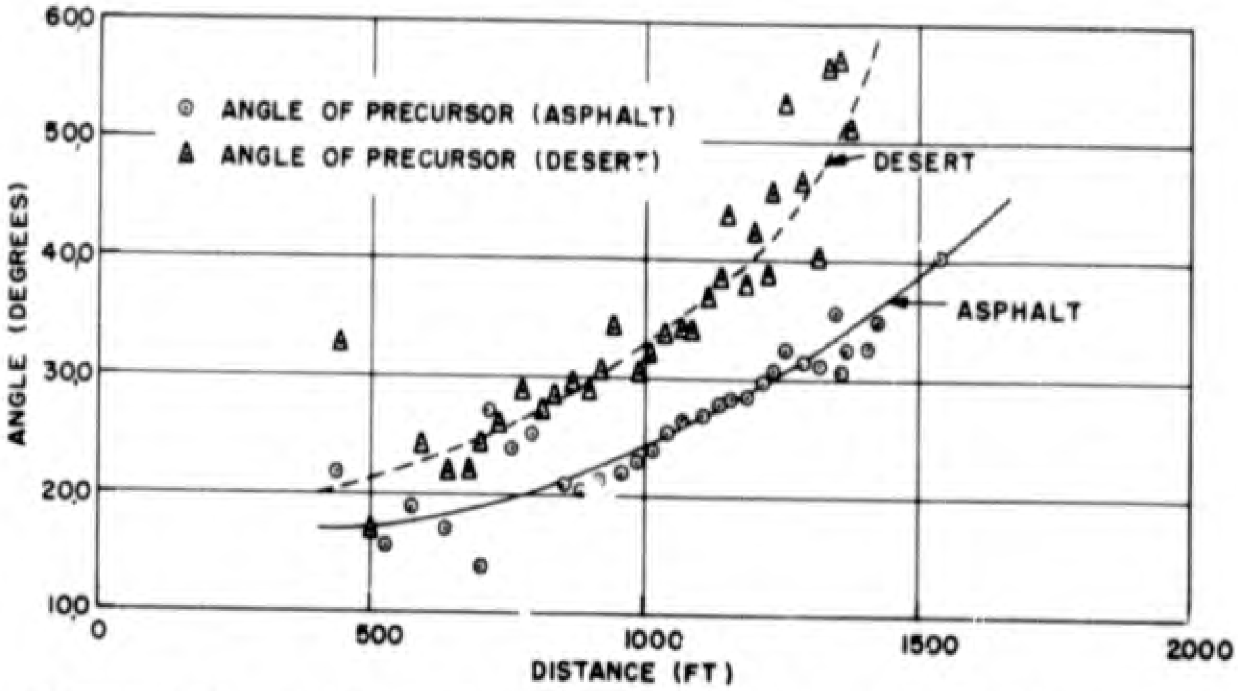

Figure 3.20 Shot 6, Angle of the Precursor versus Ground Range.

time equation over the range from 300 to 2,500 ft was found by the method described in Section 1.2, and the resulting constants are:

$$a = 980.185$$

$$b = 1{,}171.669$$

$$c = -0.005927$$

For the free-air shock the instantaneous shock velocity equation is thus

$$U = 980.2 \left[1 + \left(\frac{1171.7}{R} \right)^{1.5} \right] \qquad (3.2)$$

Figure 3.25 is a plot of these shock velocities as a function of distance.

The peak shock overpressures at various distances were calculated using the shock velocities obtained from Equation 3.2 and the ambient

(Continued on Page 60)

[redacted]

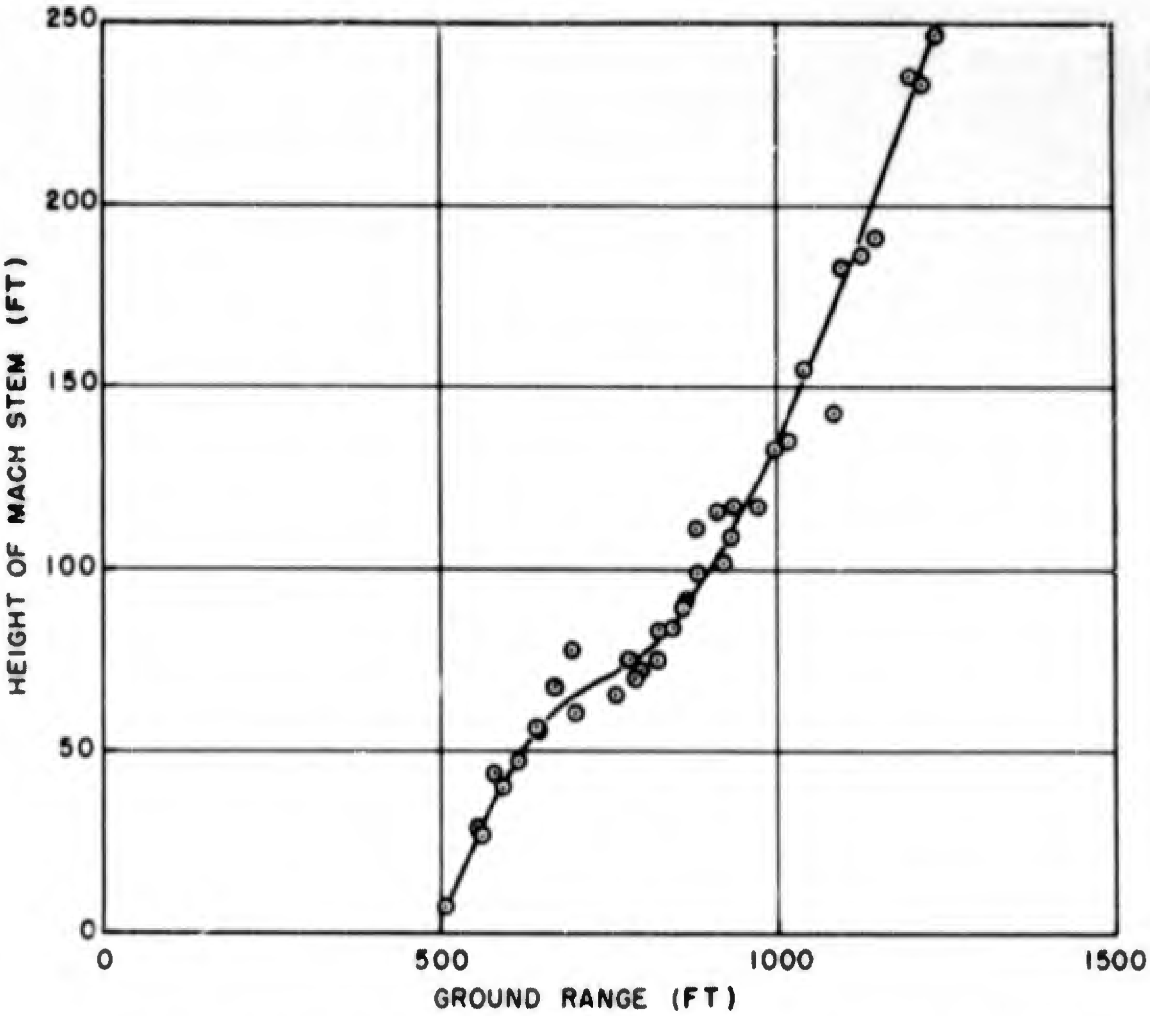

Figure 3.21 Shot 6 - Height of the Triple Point as a Function of Ground Range (Desert Area).

TABLE 3.10 - Shot 6, Height of the Triple Point as a Function of Ground Range Over the Desert Area

Ground Range (ft)	Height (ft)	Ground Range (ft)	Height (ft)
Film 28081		Film 28084	
555.2	28.7	507.1	7.5
616.0	46.8	560.7	27.0
645.5	56.2	580.2	44.0
700.3	60.2	595.2	40.0
781.9	74.9	643.3	56.6
801.3	72.2	669.8	67.6
822.7	83.6	693.8	77.6
862.9	89.6	760.9	65.1
881.6	99.0	789.9	70.1
911.0	115.7	823.5	75.1
931.1	108.4	844.0	84.1
971.2	117.1	868.0	91.6
998.7	132.4	877.0	110.6
1,018.7	135.1	922.6	101.6
1,039.5	154.5	936.1	117.1
1,085.0	143.1		
1,097.7	182.6		
1,125.1	186.0		
1,145.8	190.6		
1,197.3	235.4		
1,212.0	232.8		
1,235.4	246.2		

[redacted]

BLANK PAGE

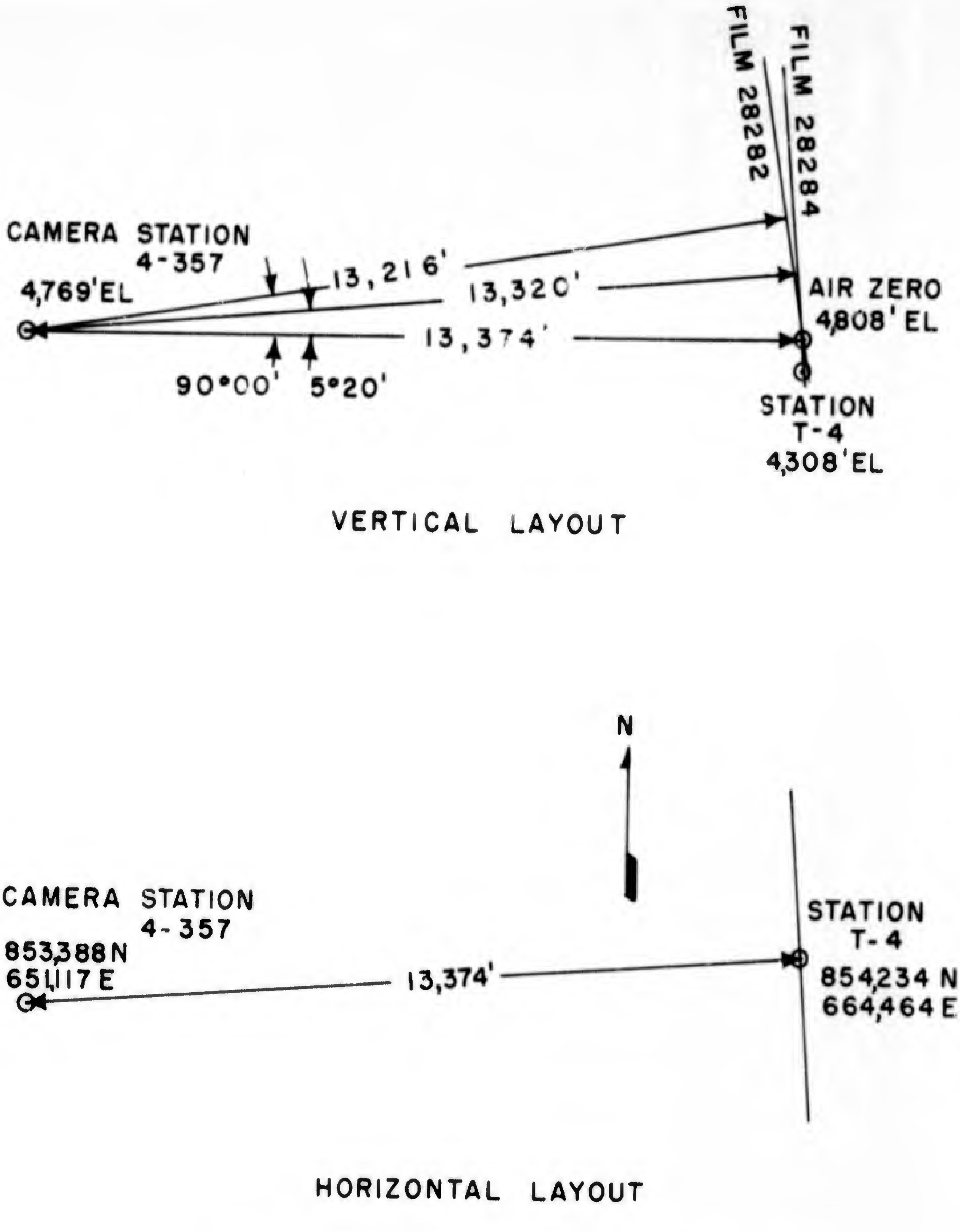

Figure 3.22 Shot 8, Planes of Measurement for Smoke Rocket Photography Films 28282, 28284.

[redacted]

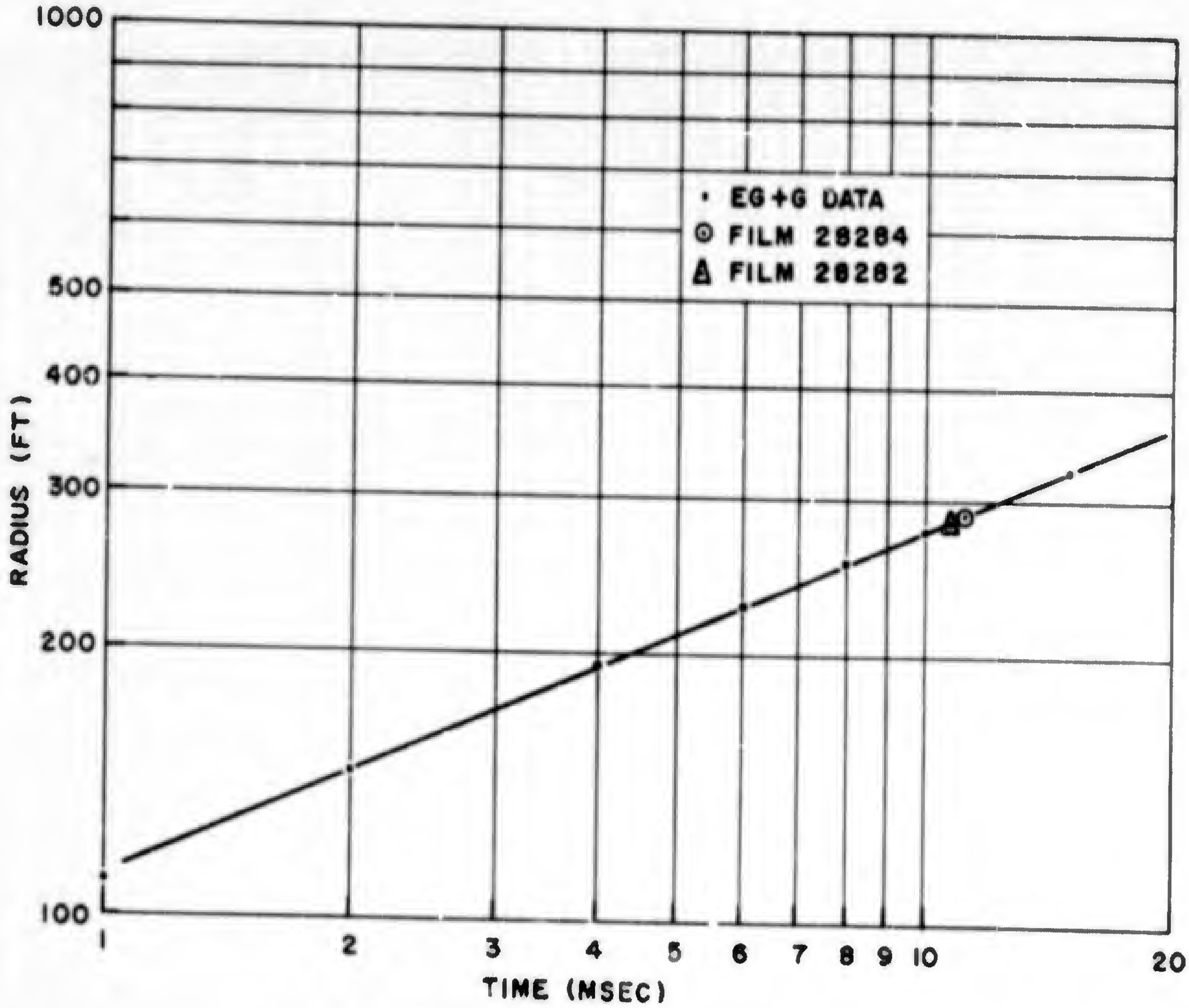

Figure 3.23 Shot 8, Fireball Radius versus Time.

TABLE 3.11 - Shot 8 - Time of Arrival of Incident Free-Air Shock in Vertical Direction from Air Zero

Distance (ft)	Time (sec)	Distance (ft)	Time (sec)
Film 28284		Film 28282	
289.6	0.01125	283.7	0.01070
372.5	0.02114	370.5	0.02062
450.7	0.03103	1,354.0	0.38747
498.2	0.04092	1,428.4	0.43704
538.3	0.05081	1,508.2	0.48662
719.0	0.10025	1,579.9	0.53620
833.5	0.13981	1,663.9	0.58577
952.7	0.18925	1,745.2	0.63534
1,055.2	0.23870	1,811.3	0.68492
1,163.2	0.28814	1,885.7	0.73450
1,253.5	0.33759	1,960.0	0.78407
1,342.9	0.38703	2,031.7	0.83364
1,427.7	0.43648	2,097.8	0.88322
1,513.4	0.48592	2,173.5	0.93280
1,595.3	0.53537	2,239.6	0.98237
1,674.5	0.58481	2,307.1	1.03194
		2,370.5	1.08152
		2,443.5	1.13110
		2,512.4	1.18067

[redacted]

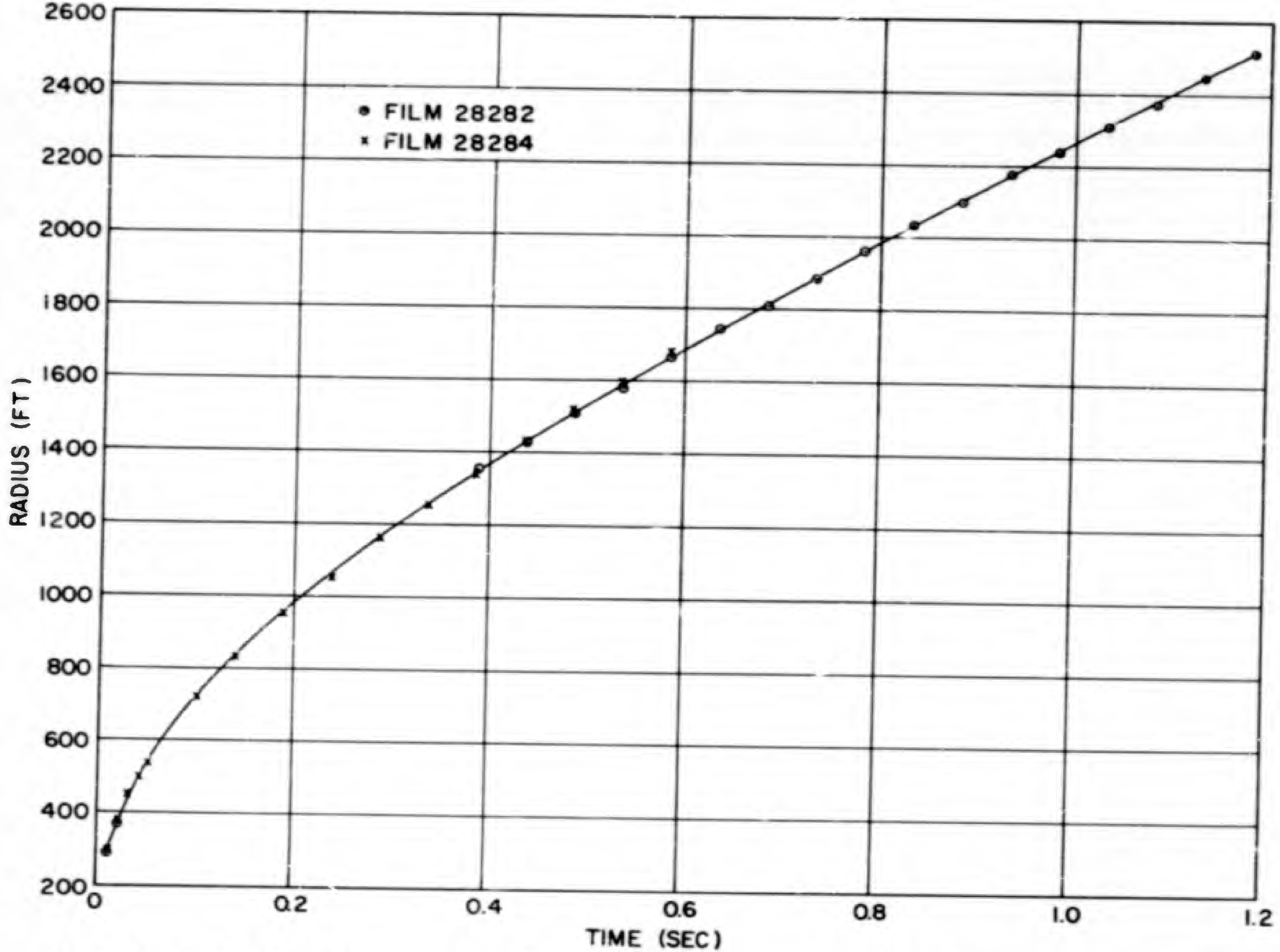

Figure 3.24 Shot 8, Time of Arrival of Incident Free-Air Shock in Vertical Direction.

atmospheric conditions (P_0 and C_0) existing at burst height (see Table 1.1 for values of P_0 and T_0). These data are given in Table 3.12 and plotted in Fig. 3.26. The change in slope of the pressure-distance curve below the 15-psi level is not thought to be real but is thought to be the result of the fitting function. (This is discussed in Sections 3.9 and 4.1.3).

Shot 8, like Shot 4, was instrumented with rocket-smoke photography to obtain data on the reflected wave in free-air and to determine the point of catch up of the reflected wave with the incident shock. However,

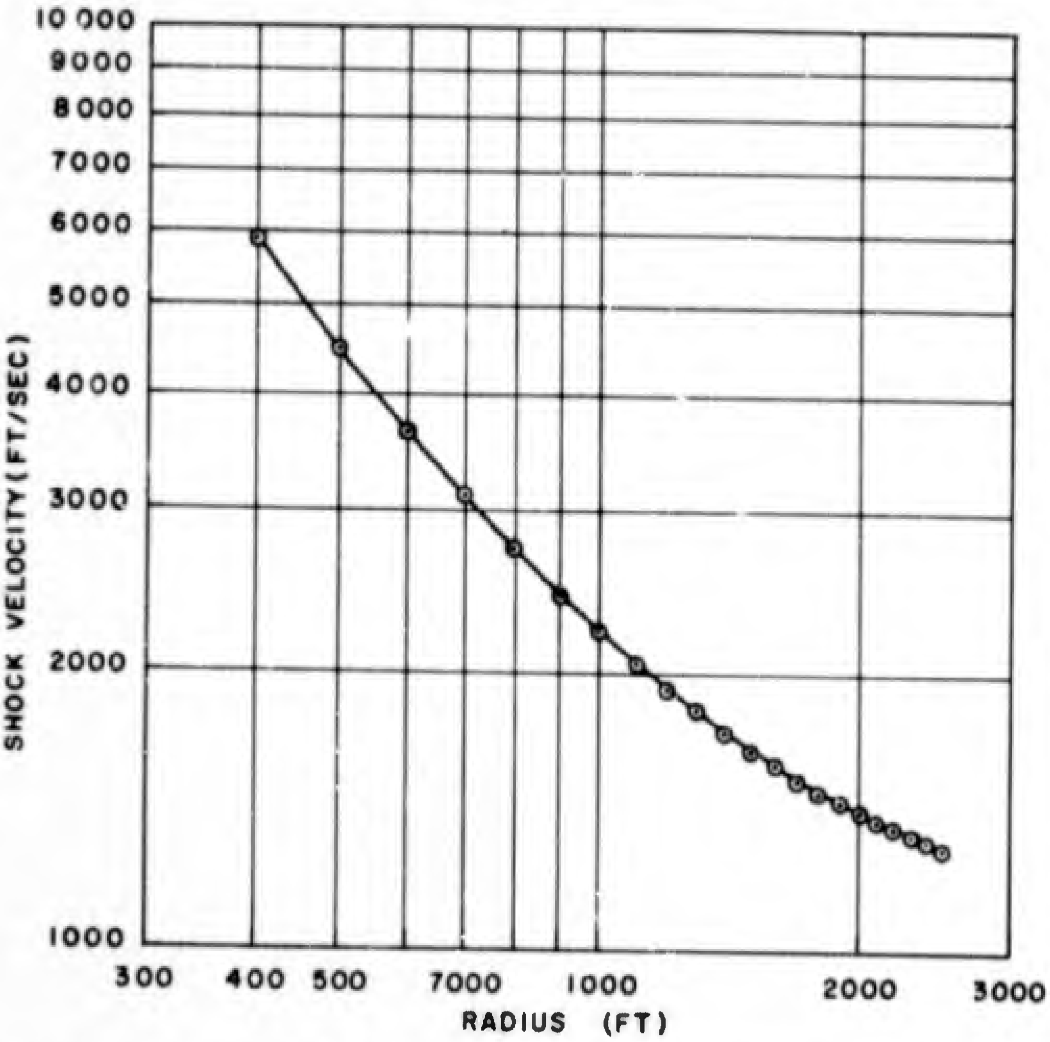

Figure 3.25 Shot 8, Free-Air Shock Velocity versus Distance.

the Shot 8 device detonated at a lower yield than was expected; because of its high effective height of burst, the desired data could not be obtained. Moreover no reflected wave could be detected above the fire-ball on the films.

Shock phenomena occurring near the ground were measured to the north side of ground zero on Shot 8 from Films 28280 and 28283 (See Fig. 3.27 for the planes of measurement). South of ground zero a rise in the foreground limited the measurements along the ground that could be made. A precursor was formed on this shot and was observed on both sides of ground zero. Its arrival time along the ground was measured

[redacted]

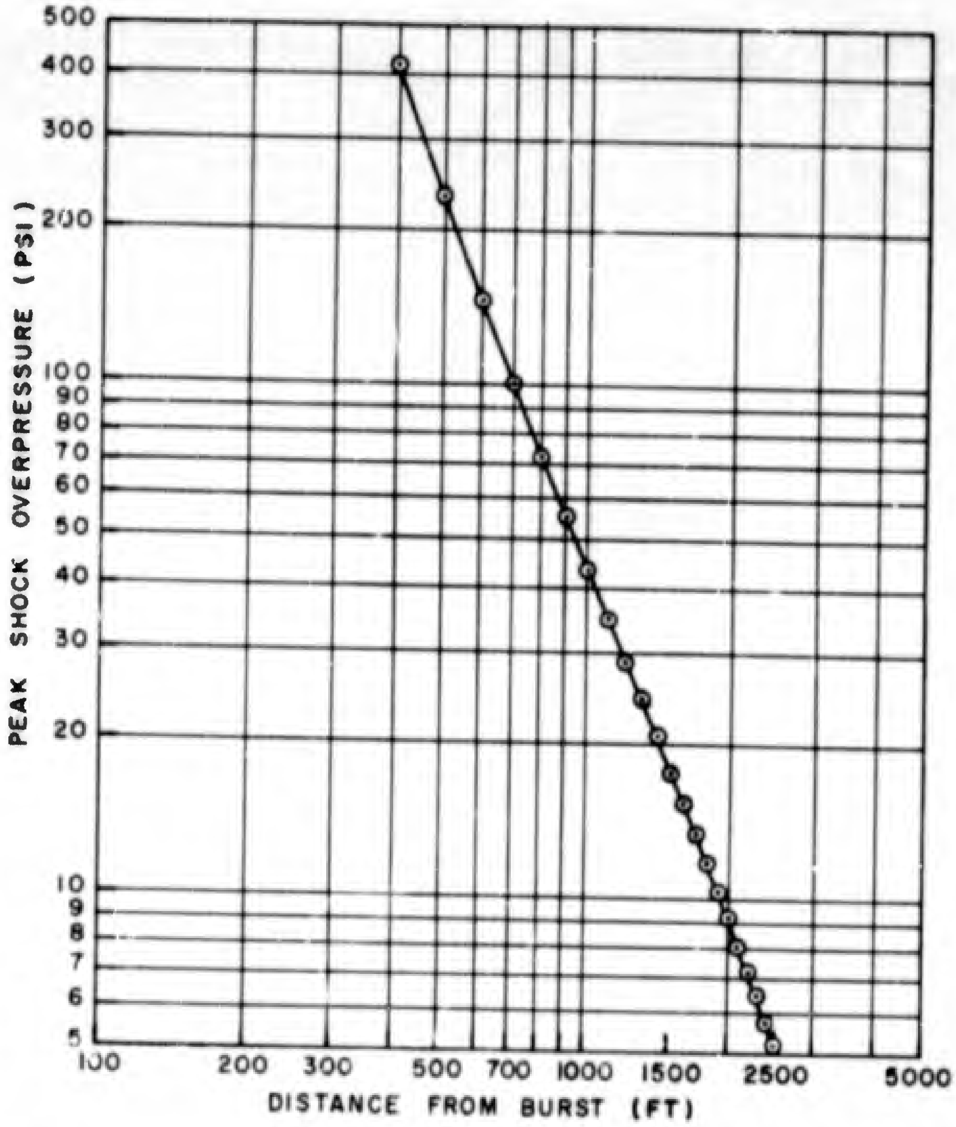

Figure 3.26 Shot 8, Free-Air Peak Shock Overpressure versus Distance.

TABLE 3.12 - Shot 8, Pressure, Shock Velocity, Distance Data in Free Air

Distance R (ft)	Shock Velocity U (ft/sec)	Shock Overpressure P(psi)
400	5,894.1	415.1
500	4,496.3	231.7
600	3,655.0	145.0
700	3,102.8	100.4
800	2,717.5	72.0
900	2,436.2	55.1
1,000	2,223.3	43.4
1,100	2,057.7	35.1
1,200	1,925.9	28.9
1,300	1,818.9	24.3
1,400	1,730.6	20.7
1,500	1,656.9	17.6
1,600	1,594.4	15.3
1,700	1,541.0	13.3
1,800	1,494.9	11.7
1,900	1,454.8	10.3
2,000	1,419.7	9.2
2,100	1,388.7	8.1
2,200	1,361.1	7.2
2,300	1,336.6	6.5
2,400	1,314.5	5.8
2,500	1,294.7	5.2

[redacted]

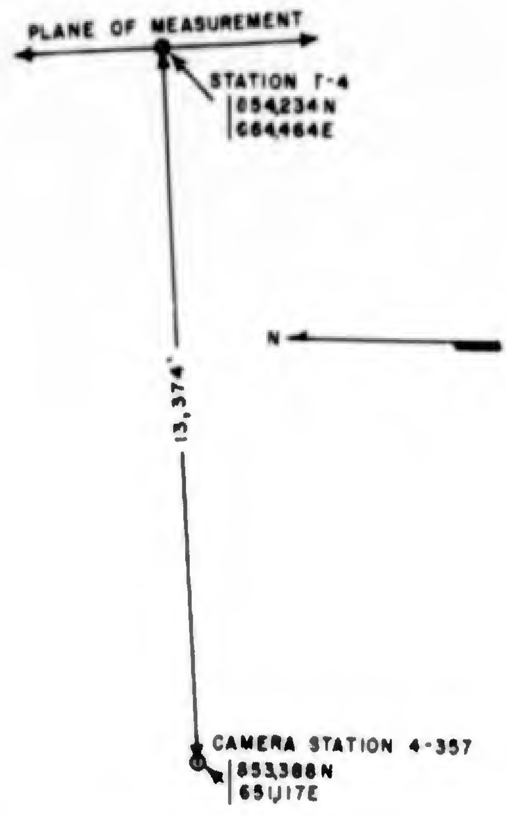

Figure 3.27 Shot 8, Plane of Measurement for Direct Shock Photography Films 28280 and 28283.

north of ground zero. These data are listed in Table 3.13 and plotted in Fig. 3.28. No attempt has been made to measure the angle that the precursor front made with the surface, since such data would have contained a large uncertainty.

The height of the Mach stem as a function of ground range was also measured on Shot 8 on the north side of ground zero. These measurements

TABLE 3.13 - Shot 8 - Time of Arrival of Precursor Along the Ground North of Ground Zero

Ground Range (ft)	Time (sec)	Ground Range (ft)	Time (sec)
Film 28283		Film 28280	
702.8	0.14950	361.6	0.07823
877.1	0.19988	433.9	0.08813
1,029.2	0.25025	474.0	0.09803
1,170.4	0.30062	518.6	0.10803
1,294.9	0.35100	561.5	0.11803
1,420.8	0.40138	603.4	0.12793
1,523.1	0.45175	642.1	0.13803
1,618.6	0.50212	690.0	0.14773
1,709.9	0.55250	730.5	0.15763
1,826.1	0.60288	765.5	0.16743
1,900.8	0.65325	794.5	0.17723
		829.1	0.18723
		856.7	0.19753
		893.6	0.20683
		925.8	0.21683
		957.6	0.22673
		979.2	0.23663
		1,006.9	0.24643

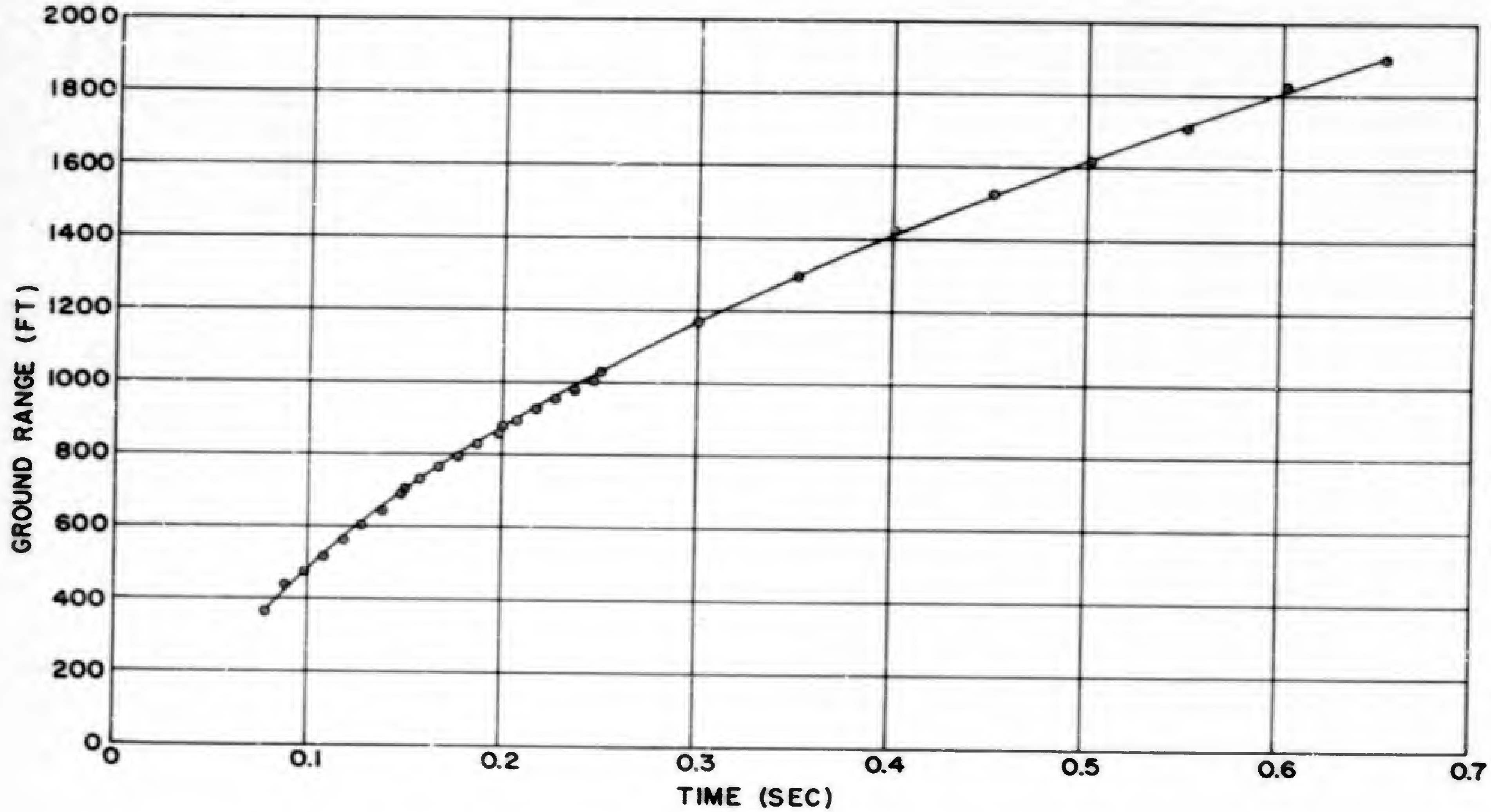

Figure 3.28 Shot 8, Time of Arrival of Precursor along the Ground North of Ground Zero.

TABLE 3.14 - Shot 8 - Height of Triple Point as a Function of Ground Range

Ground Range (ft)	Height of Triple Point (ft)
345.4	2.8
459.7	10.6
509.0	15.2
550.4	22.6
590.5	21.6
622.7	27.2
655.0	35.5
684.0	39.6
719.0	45.1
752.6	49.3
792.2	57.6
825.8	65.4
859.5	68.2
884.4	65.9
912.4	69.1
947.4	75.5
981.1	83.8

were obtained over a ground range of from 300 to 1,000 ft and are plotted in Fig. 3.29 and given in Table 3.14.

3.6 SHOT 9

The results of Shot 9 were similar to those of Shot 1; however, a precursor was observed to form on both sides of ground zero at approxi-

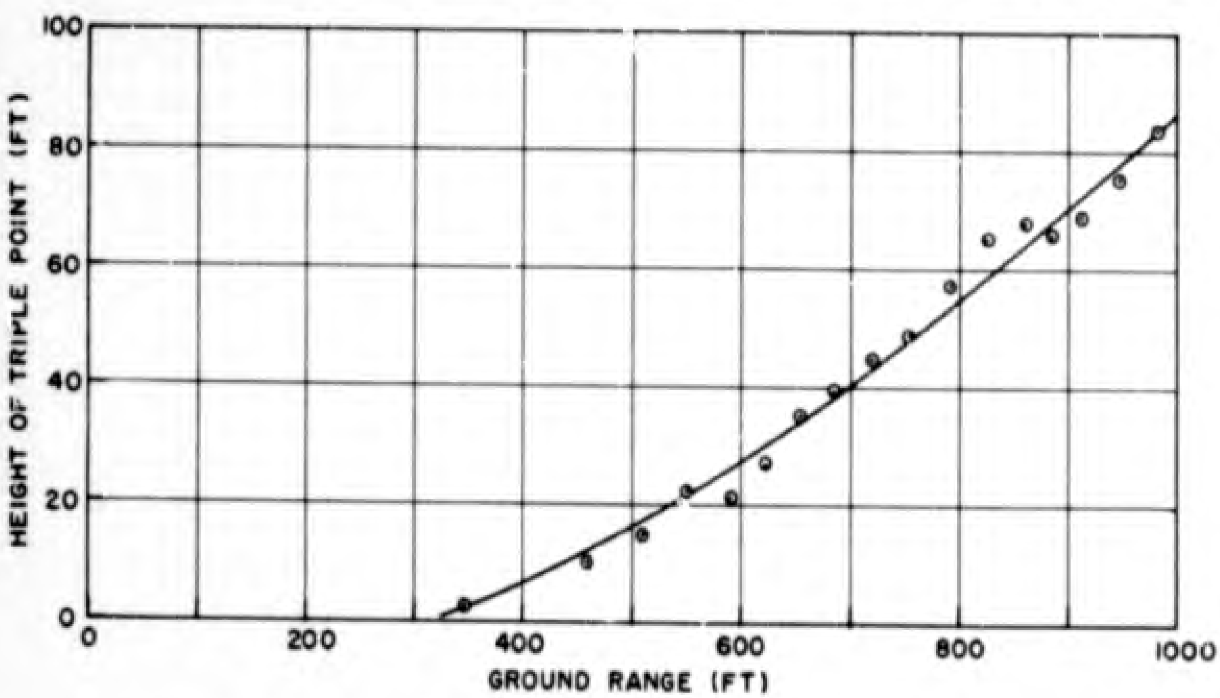

Figure 3.29 Shot 8, Height of the Triple Point as a Function of Ground Range.

mately 300 ft ground range. Measurements of the time of arrival of the precursor to the southwest (out to 1,150 ft) and to the northeast (out to 1,000 ft) of ground zero were made on Film 29384. These data are presented in Table 3.15 and plotted in Fig. 3.30. As on Shot 1, the propagation of the precursor to the northeast side of ground zero over

[redacted]

TABLE 3.15 Shot 9 - Arrival Time of Precursor Along the Ground Northeast and Southwest of Ground Zero

	Northeast	Southwest
Time (sec)	Ground Range (ft)	Ground Range (ft)
0.21663		190.2
0.22650		232.7
0.23638	317.6	302.8
0.24625	390.4	377.2
0.25612	439.8	426.6
0.26599	472.8	460.6
0.27586	515.3	495.1
0.28574	556.7	536.0
0.29561	594.9	562.0
0.30548	630.5	596.0
0.31535	668.2	633.2
0.32522	706.5	662.9
0.33510	740.0	690.6
0.34497	768.6	708.6
0.35484	798.9	738.4
0.36471	825.5	761.7
0.37458	857.9	786.2
0.38446	882.8	810.1
0.39433	909.4	823.4
0.40420	942.3	851.0
0.41407	965.7	867.4
0.42394	972.1	889.8
0.43382	995.5	905.2
0.44369		919.0
0.45336		937.6
0.46343		953.0
0.47330		975.8
0.48318		989.6
0.49305		996.0
0.50292		1,024.2
0.51279		1,034.8
0.52266		1,057.1
0.53254		1,081.0
0.54241		1,086.8
0.55228		1,107.6
0.56215		1,118.2
0.57202		1,142.1
0.58190		1,158.0

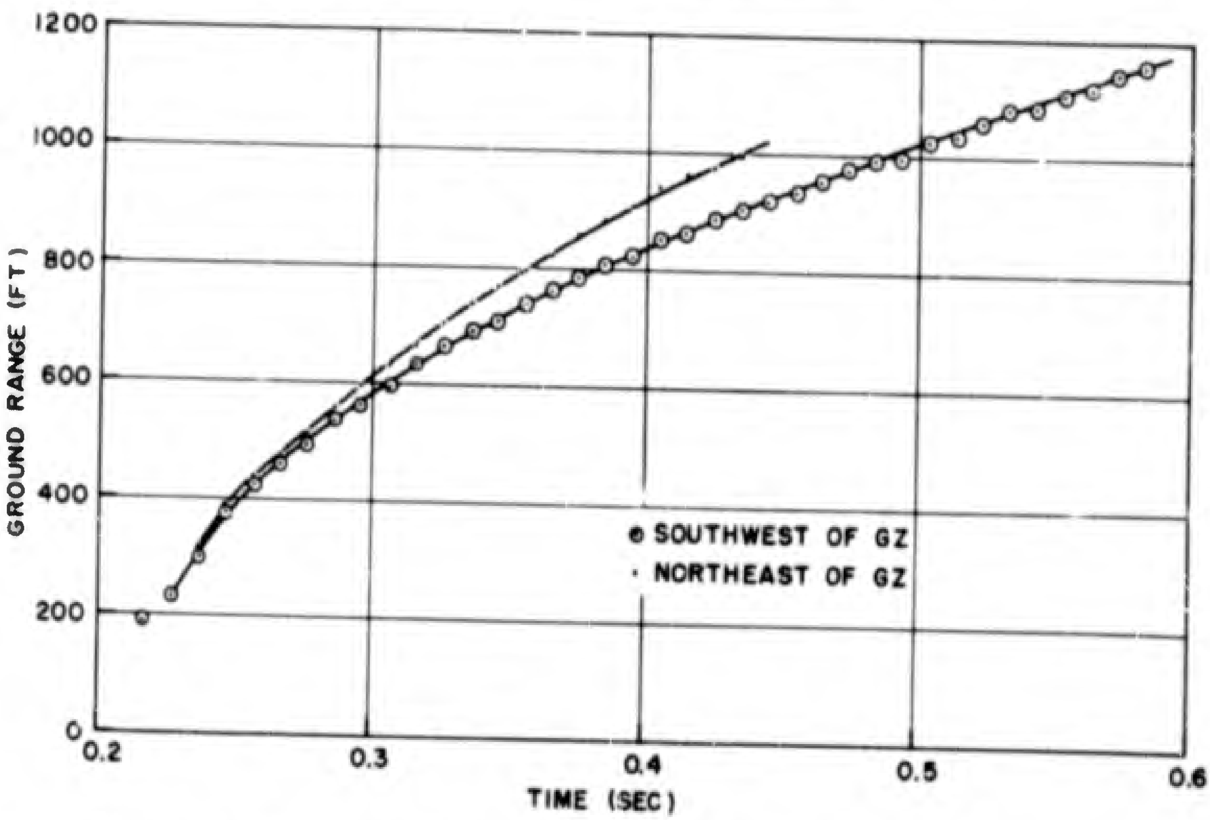

Figure 3.30 Shot 9, Time of Arrival of Precursor Northeast and Southwest of Ground Zero along the Ground.

[redacted]

the asphalt surface was faster than to the southwest, where there was only the natural desert surface. Other than this asymmetry, no unusual phenomena were observed. The reflected wave data that could be obtained were limited to the point of insignificance.

3.7 SHOT 10

Arrival-time data were measured on Film 28980 taken by the high-speed (500 frames/sec) Fastax camera (see Table 2.2 for the film calibration constants). These data are presented in Table 3.16 and plotted in Fig. 3.31. A comparison of these data with the arrival-time data measured by the two nearest AFCRC canisters (Project 1.1) shows good

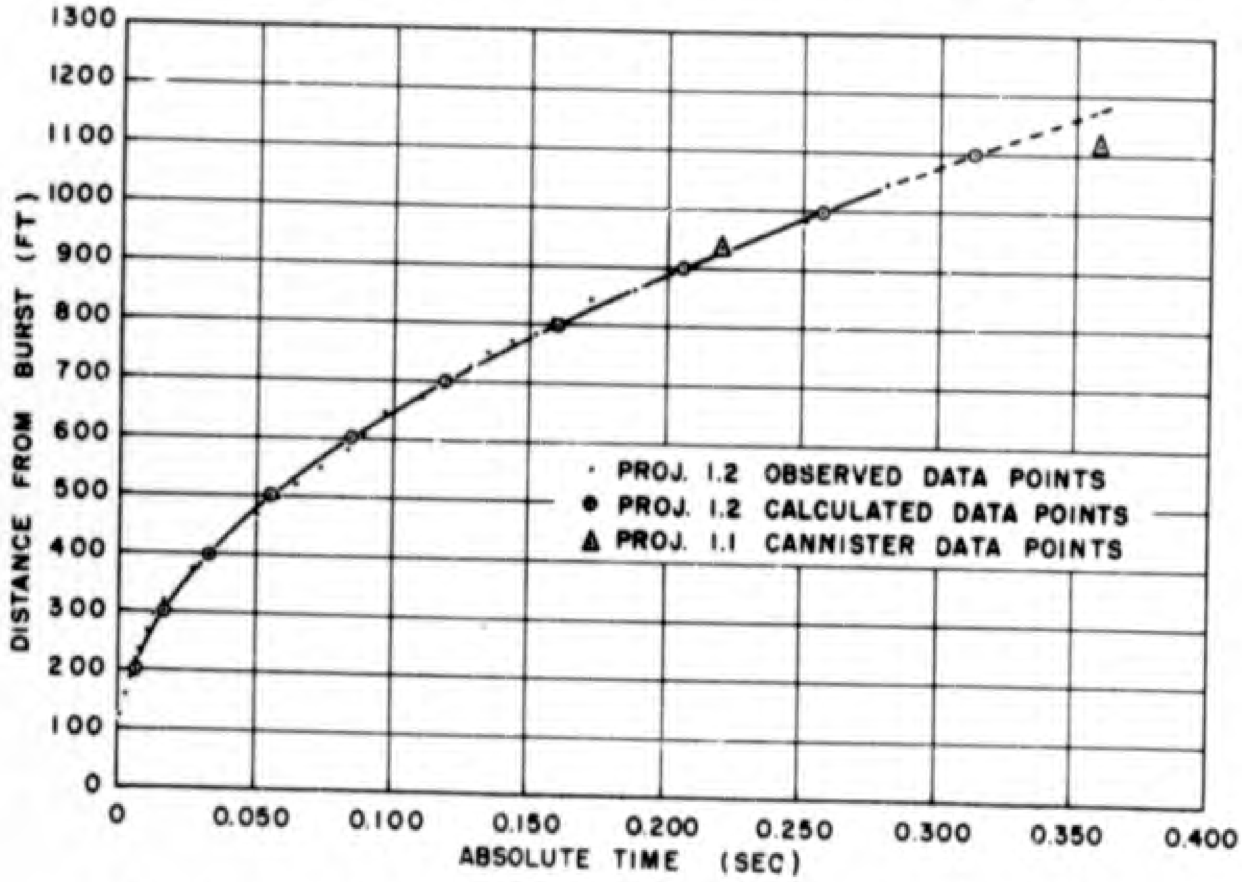

Figure 3.31 Shot 10 - Time of Arrival of Free-Air Shock.

agreement; however, the accuracy of the canister positions is given as ± 45 ft, reference 23. Figure 3.32 shows actual photographs taken from Films 28980 and 28982.

The arrival-time data were fitted to Equation 1.1, as described in Section 1.2, and the constants obtained are:

a = 763.736

b = 1,277.816

c = 0.000043

These constants are valid over the entire range of from 200 to 1,050 ft. Substitution of the constants a and b into Equation 1.2,

TABLE 3.16 - Shot 10 - Time of Arrival of Free Air Shock

Radius (ft)	Time (sec)
123.400	0.001550
157.700	0.003150
188.500	0.004750
215.300	0.006400
235.200	0.007950
267.400	0.011050
295.916	0.012590
318.365	0.017290
372.446	0.026940
467.343	0.050440
496.935	0.058240
520.404	0.064490
551.016	0.073890
581.628	0.081890
609.179	0.089540
646.934	0.097390
671.423	0.111290
690.811	0.119090
725.504	0.128440
749.994	0.134590
770.402	0.143890
785.708	0.151590
810.198	0.159290
842.850	0.172340
861.218	0.188740
914.278	0.219440
981.625	0.251440
1,044.890	0.280940

TABLE 3.17 - Shot 10 - Pressure, Velocity, Distance Data in Free Air

Radius (ft)	Shock Velocity (ft/sec)	Peak Overpressure (psi)
200	13,098	712
300	7,478	225
400	5,124	104
500	3,884	55.7
600	3,137	34.5
700	2,647	23.5
800	2,306	16.8
900	2,056	12.7
1,000	1,867	9.8
1,100	1,720	7.7

TABLE 3.18 - Shot 10 - Weapon Yield Versus Distance

Radius (ft)	Yield (kt)
407	3.51
447	3.51
505	3.51
615	3.51
719	3.44
787	3.38
884	3.24
950	3.18
1,046	3.11
1,111	3.11

[redacted]

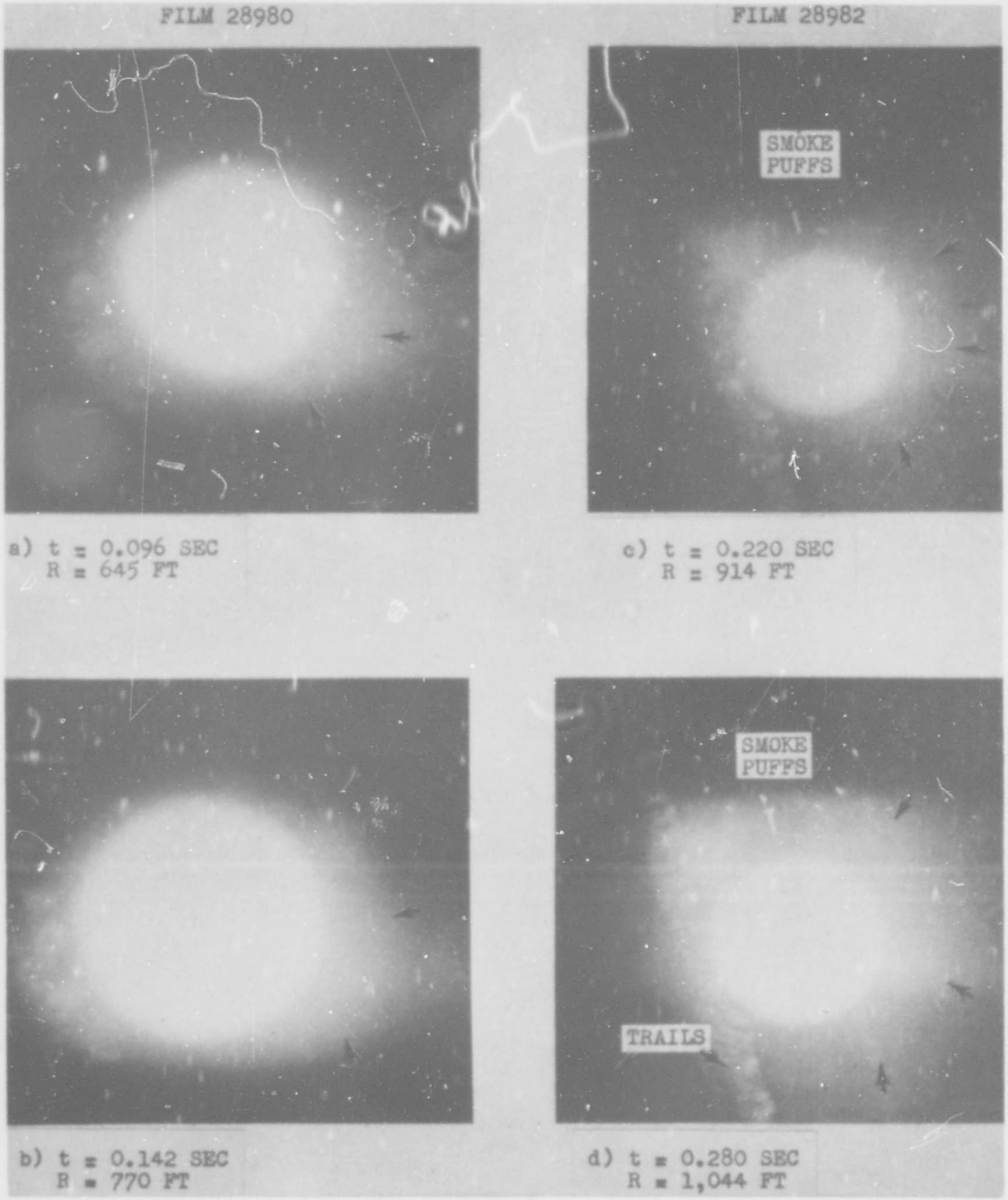

Figure 3.32 Shot 10, Photographs of Free-Air Shock Taken from Films 28980 and 28982.

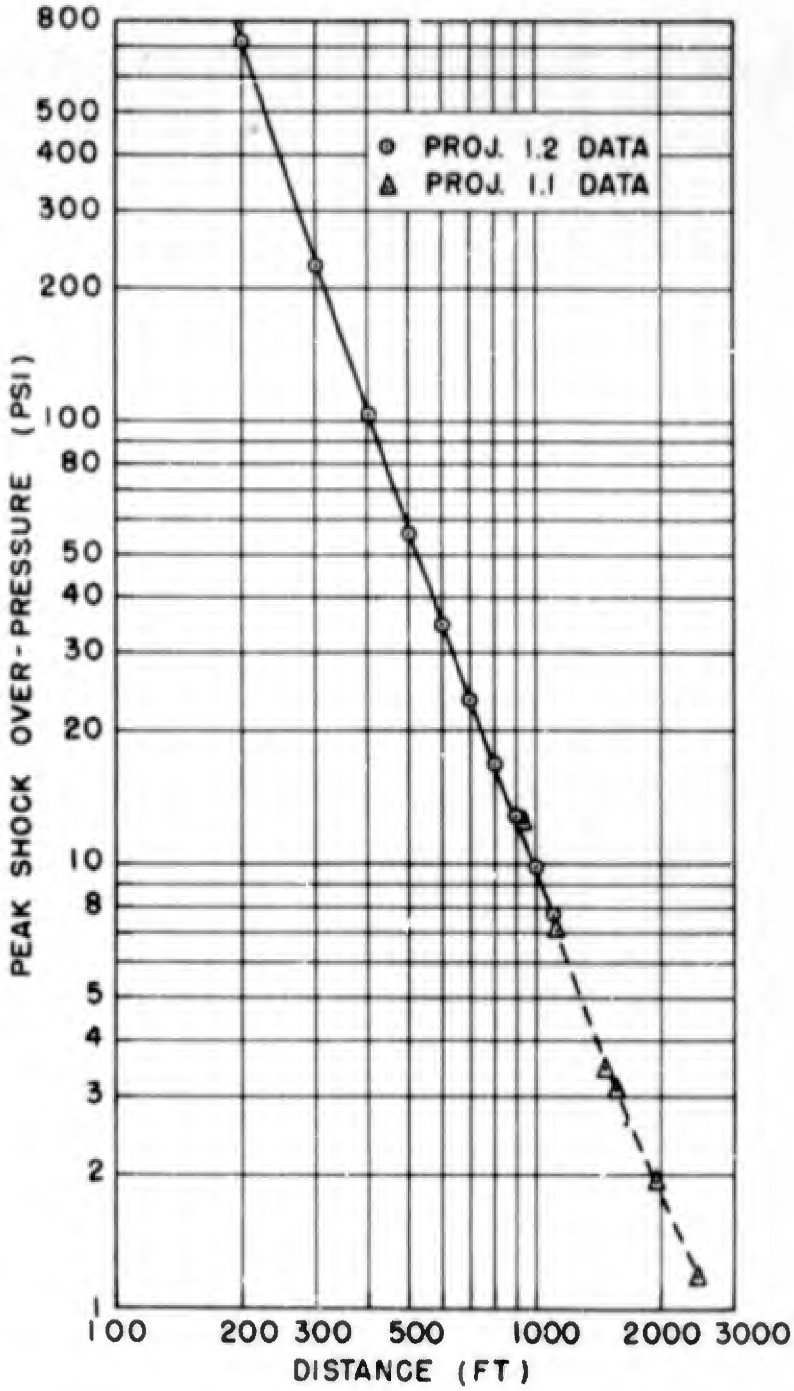

Figure 3.33 Shot 10 - Peak Shock Overpressure as a Function of Distance.

Section 1.2, gives the instantaneous velocities as a function of distance. This equation is

$$U = 763.7 \left[1 + \left(\frac{1277.8}{R} \right)^{1.5} \right] \tag{3.3}$$

where R is given in feet and U is given in ft/sec.

By substitution of the instantaneous velocities into the Rankine-Hugoniot equation (Equation 1.3) the peak shock overpressures were calculated. Table 3.17 lists the peak overpressures and velocities as a function of distance. The ambient atmospheric conditions ahead of the shock were taken as those at burst height (see Table 1.1). Figure 3.33 is a plot of the peak shock overpressures as a function of distance. Also plotted in Fig. 3.33 are the pressure-distance data obtained by the AFCRC canisters (from Reference 23), and there is excellent agreement between the two sets of data. The weapon yield as a function of

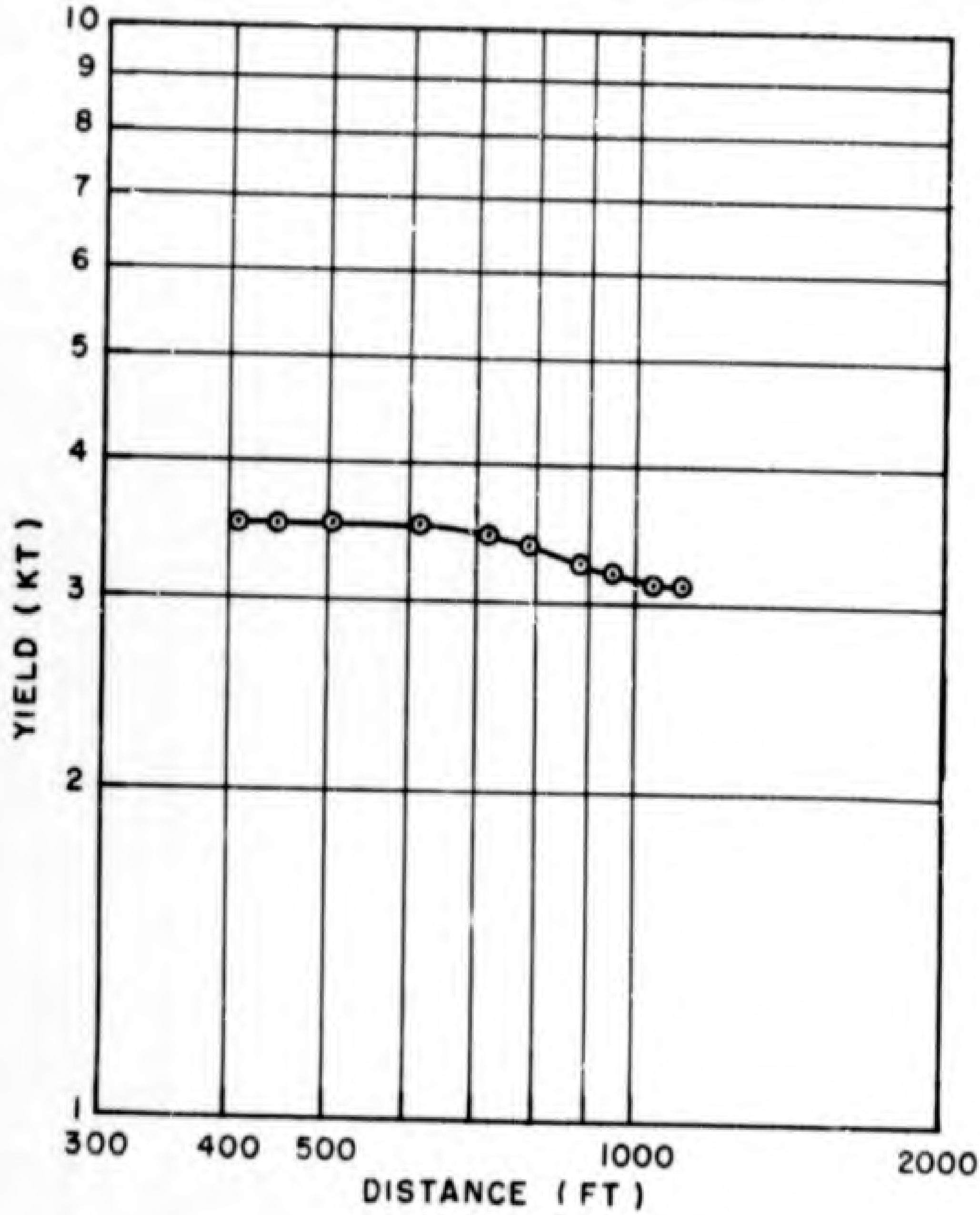

Figure 3.34 Shot 10 - Weapon Yield as a Function of Distance Obtained from Free-Air Pressure-Distance Data.

distance was calculated in the same manner as on Shot 4 (see Section 3.3) and the results are presented in Table 3.18 and plotted in Fig. 3.34.

It is difficult to determine a figure of accuracy for the data obtained by the method used on this shot. However, it is thought that the distances measured are within ± 10 ft and the timing is accurate to about 0.1 percent. Although the dispersion of the arrival-time data about the fitted curve is greater than usual, a calculation of the

[redacted]

accuracy of the pressure-distance curve indicates that the pressures may be in error by as much as 2 to 3 percent from 400 psi to 8 psi.

3.8 SHOT 12

3.8.1 Free-Air Data

Arrival-time data for the incident free-air shock were measured in the vertical direction directly above air zero on Films 28389 and 28390 over a range of from 250 to 3,000 ft (see Fig. 3.35

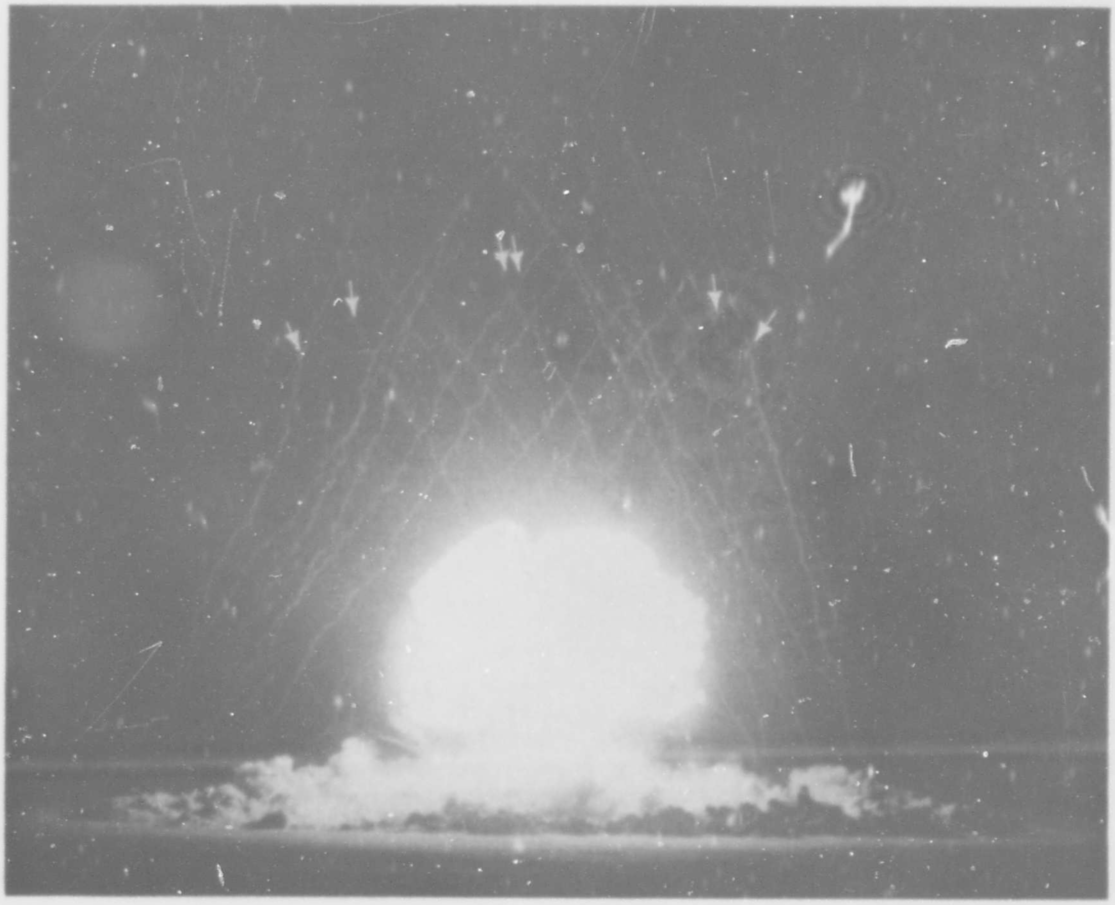

Figure 3.35 Shot 12, Photograph of Free-Air Shock 2,330 ft from Air Zero at t = 0.946 Sec (Film 28389).

for actual photographs of the free-air shock). These data are listed in Table 3.19 and plotted in Fig. 3.36. Distance and time scaling factors were determined as explained in Section 2.2, and the film calibration constants for these films are listed in Table 2.2. The absolute time for each film was found by plotting the first data point from the NOL films on the data supplied by EG&G for fireball radius

TABLE 3.19 - Shot 12 - Time of Arrival of Incident Shock in Free Air in Vertical Direction Above Air Zero

Film 28389

Radius (ft)	Time (sec)	Radius (ft)	Time (sec)
264.728	0.007420	2,035.758	0.745870
361.354	0.017266	2,074.144	0.765562
1,446.738	0.391414	2,099.293	0.785254
1,461.298	0.401260	2,131.060	0.804946
1,475.859	0.411106	2,162.828	0.824638
1,490.419	0.420952	2,187.977	0.844330
1,524.833	0.430798	2,222.392	0.864022
1,555.277	0.450490	2,303.134	0.923098
1,568.513	0.460336	2,329.606	0.946192
1,580.426	0.470.82	2,375.934	0.965884
1,606.899	0.480028	2,403.730	0.985576
1,622.783	0.489874	2,409.025	1.005268
1,657.197	0.509566	2,448.734	1.024960
1,684.994	0.529258	2,461.970	1.044652
1,733.968	0.548950	2,495.061	1.064344
1,747.205	0.568642	2,520.210	1.084036
1,786.914	0.588334	2,571.832	1.103728
1,817.358	0.608026	2,587.716	1.123420
1,847.801	0.627718	2,623.454	1.143112
1,879.569	0.647410	2,706.844	1.231726
1,910.012	0.667102	2,766.408	1.280956
1,941.780	0.686794	2,867.004	1.330186
1,978.842	0.706486	2,902.742	1.379416
2,013.[illegible]6	0.726178	2,955.688	1.428646

Film 28390

Radius (ft)	Time (sec)	Radius (ft)	Time (sec)
603.447	0.067675	1,427.172	0.384315
649.242	0.077570	1,444.563	0.394210
690.979	0.087465	1,461.953	0.404105
724.600	0.097360	1,481.662	0.414000
760.540	0.107255	1,502.531	0.423895
797.060	0.117150	1,521.060	0.433790
828.942	0.127045	1,538.471	0.443685
858.506	0.136940	1,556.441	0.453580
885.171	0.146835	1,573.831	0.463475
910.098	0.156730	1,589.483	0.473370
934.444	0.166625	1,609.771	0.483265
961.109	0.176520	1,626.582	0.493160
986.615	0.186415	1,644.552	0.503055
1,014.440	0.196310	1,664.261	0.512950
1,044,583	0.206205	1,678.174	0.522845
1,067.771	0.216100	1,699.042	0.532740
1,086.300	0.225995	1,717.012	0.542635
1,109.508	0.235890	1,730.345	0.552530
1,134.434	0.245785	1,746.576	0.562425
1,156.462	0.255680	1,762.227	0.572320
1,176.750	0.265575	1,776.139	0.582215
1,194.720	0.275470	1,795.269	0.592110
1,212.691	0.285365	1,827.731	0.611900
1,239.356	0.295260	1,864.251	0.631690
1,263.123	0.305156	1,898.452	0.651480
1,281.672	0.315050	1,929.175	0.671270
1,302.341	0.324945	1,965.695	0.691060
1,321.670	0.334840	1,998.157	0.710850
1,336.162	0.344735	2,023.663	0.730640
1,360.509	0.354630	2,059.603	0.750430
1,382.537	0.364525	2,099.021	0.770220
1,406.304	0.374420	2,124.527	0.790010

[redacted]

[redacted]

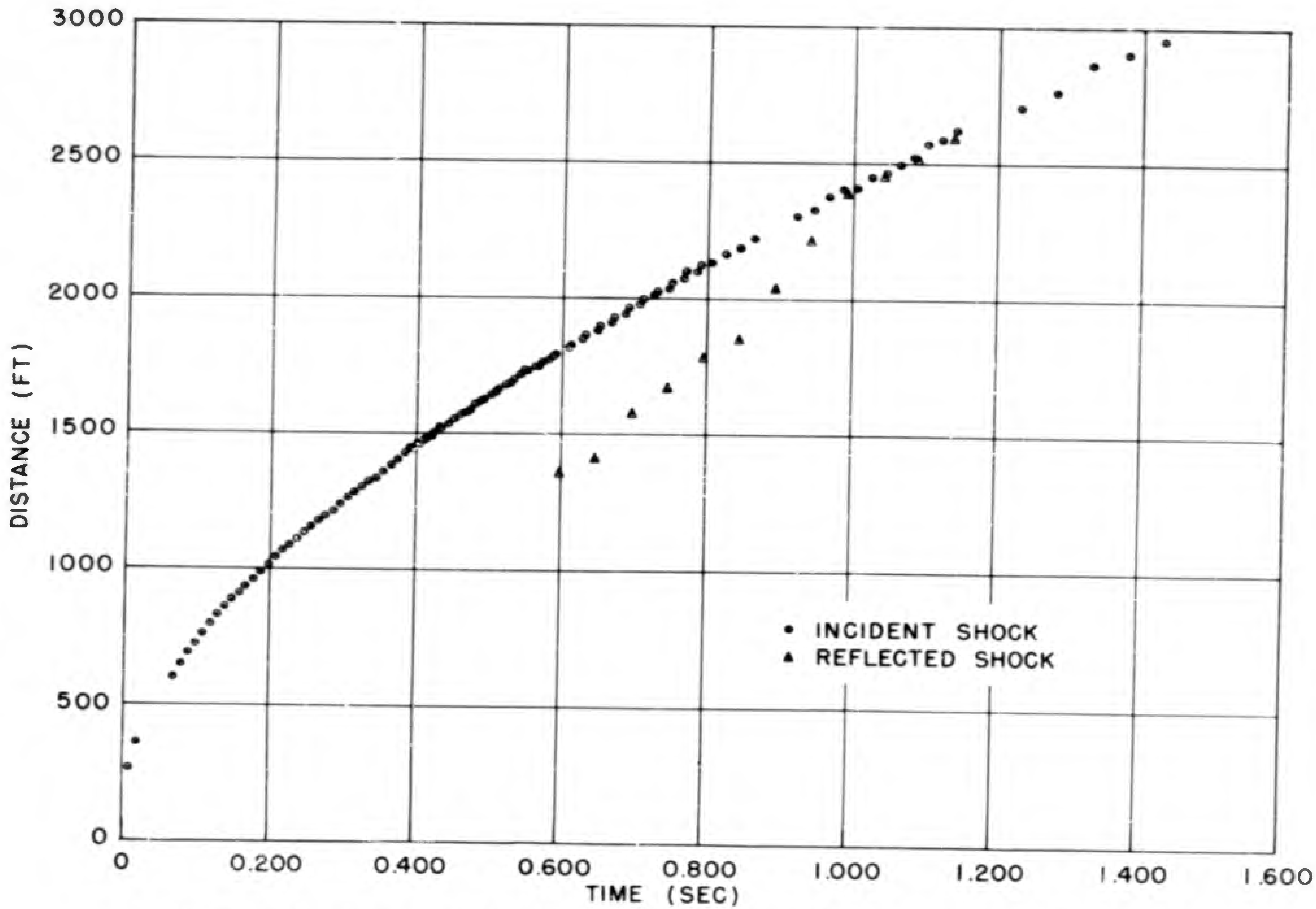

Figure 3.36 Shot 12, Time of Arrival of Free-Air Incident and Reflected Shocks.

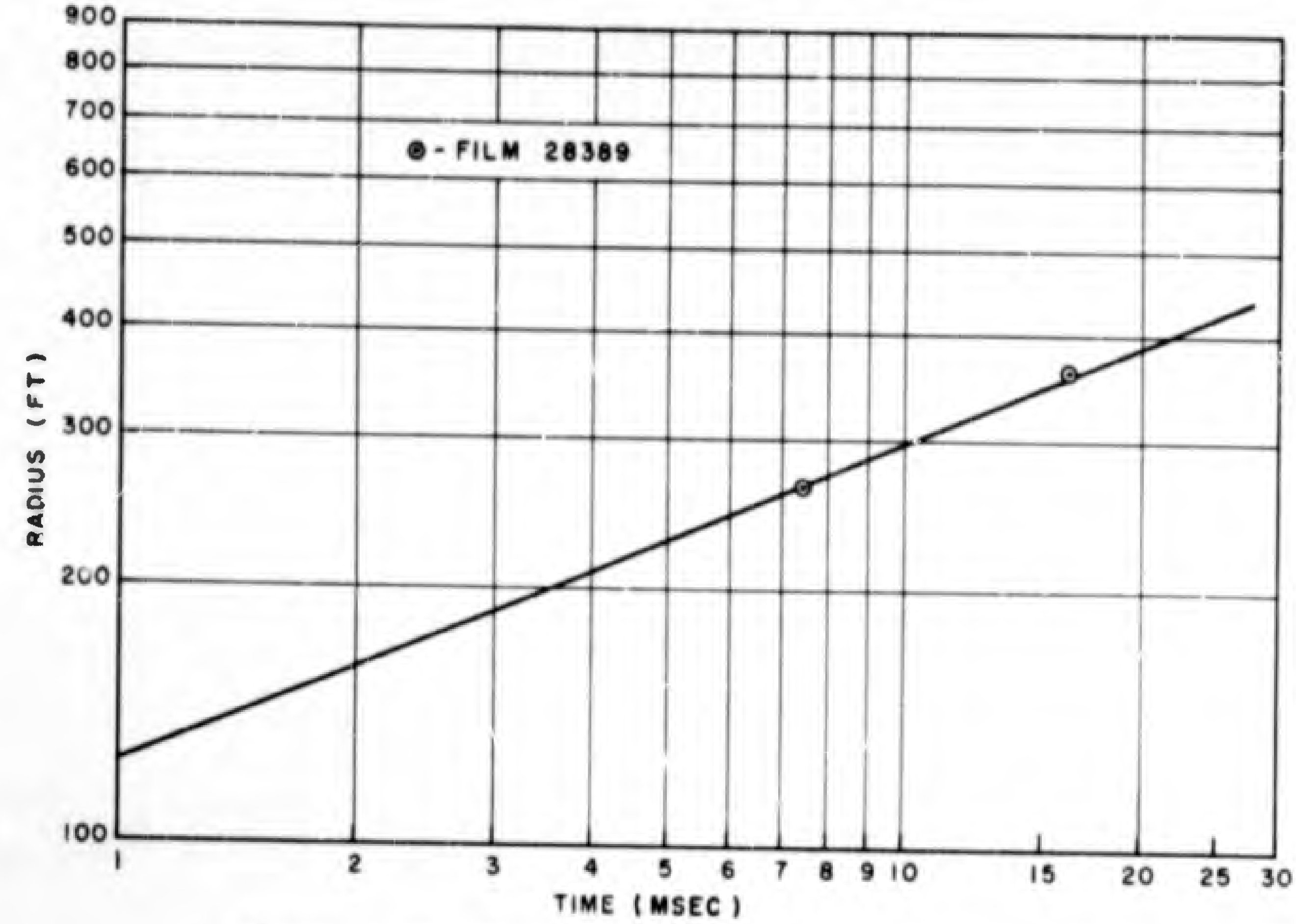

Figure 3.37 Shot 12, Fireball Radius versus Time.

TABLE 3.20 - Shot 12 - Pressure, Velocity, Distance
Data in Free Air

Distance R (ft)	Shock Velocity U (ft/sec)	Sound Velocity C_o (ft/sec)	Ambient Pressure P_o (psi)	Shock Overpressure (psi)
600	4508.2	1116.1	12.07	223.3
700	3777.1	1115.4	12.03	150.4
800	3266.9	1114.8	11.98	109.0
900	2894.3	1114.1	11.94	81.2
1,000	2612.5	1113.5	11.89	63.6
1,100	2393.2	1112.8	11.85	50.2
1,200	2218.6	1112.2	11.80	41.0
1,300	2076.9	1111.5	11.76	34.2
1,400	1960.1	1110.9	11.72	28.9
1,500	1862.4	1110.2	11.68	24.8
1,600	1779.7	1109.6	11.63	21.4
1,700	1709.0	1109.0	11.59	18.6
1,800	1648.0	1108.3	11.55	16.3
1,900	1594.9	1107.7	11.51	14.4
2,000	1548.4	1107.0	11.46	12.8
2,100	1507.3	1106.4	11.42	11.4
2,200	1470.8	1105.8	11.38	10.2
2,300	1438.3	1105.1	11.34	9.2
2,400	1409.1	1104.5	11.30	8.3
2,500	1382.8	1103.9	11.25	7.5
2,600	1359.0	1103.2	11.21	6.8
2,700	1337.4	1102.6	11.17	6.1
2,800	1317.7	1102.7	11.13	5.6
2,900	1299.7	1101.4	11.09	5.1
3,000	1283.2	1100.8	11.04	4.6

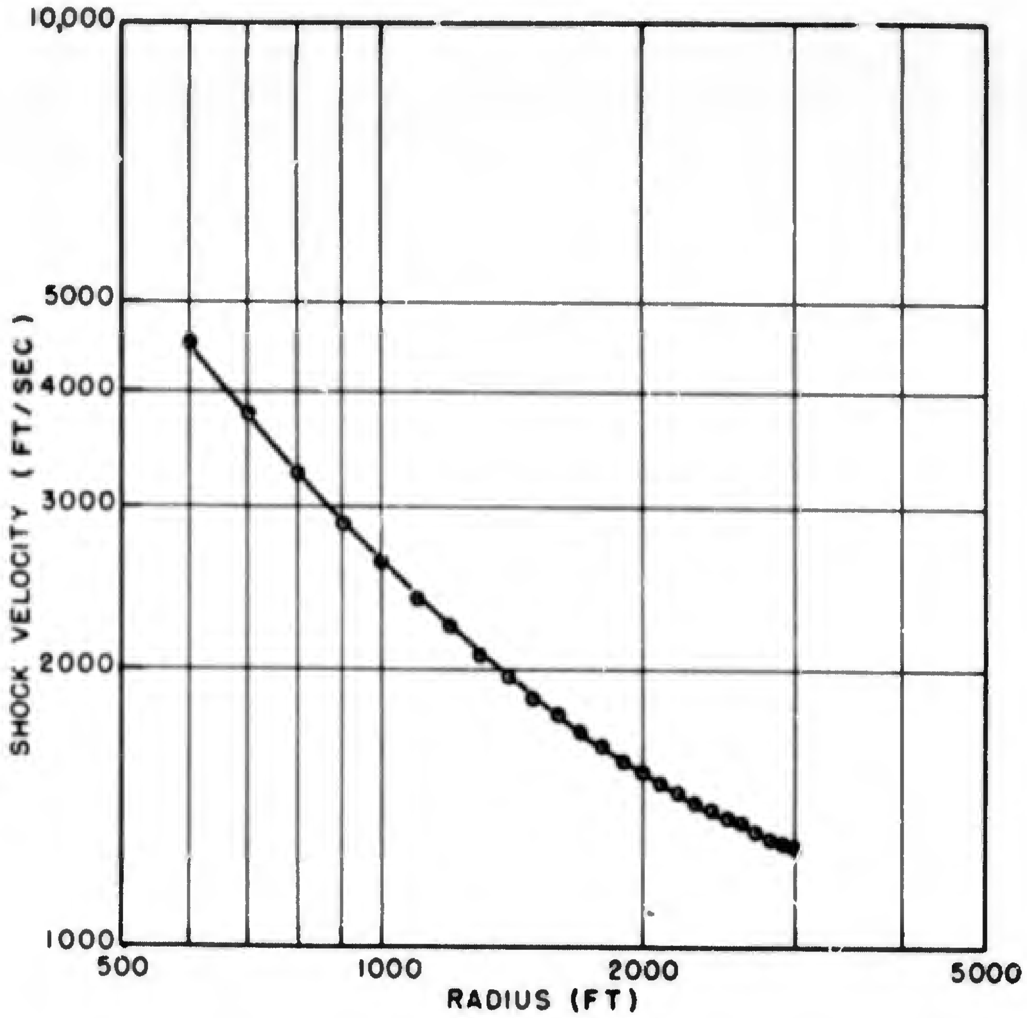

Figure 3.38 Shot 12, Free-Air Shock Velocity versus Distance.

versus time (see Fig. 3.37). The arrival-time data were then fitted to Equation 1.1, Section 1.2, and the constants obtained by this fitting process are:

$$a = 966.374$$

$$b = 1426.296$$

$$c = 0.010475$$

The constants are valid over the entire range of from 600 to 3,000 ft.

Substitution of the constants a and b into Equation 1.2, Section 1.2, gives the instantaneous shock velocities as a function of distance. This equation is

$$U = 966.4 \left[1 + \left(\frac{1426.3}{R} \right)^{1.5} \right] \tag{3.4}$$

where R is given in feet and U is given in ft/sec. The velocities obtained from Equation 3.4 are reported in Table 3.20 and plotted in Fig. 3.38 as a function of distance. Using Equation 1.3, the peak

[redacted]

shock overpressures were then calculated. The ambient atmospheric conditions ahead of the shock (P_o and C_o) were determined by the same method used on Shot 4, Section 3.3. The ambient pressure, P_o, and sound velocity, C_o, used to calculate the peak overpressure at each distance are given in Table 3.20 and plotted in Fig. 3.39. Peak shock overpressures as a function of distance for Shot 12 are listed in Table 3.20, and Fig. 3.40 is a plot of pressure versus distance for the free-air incident shock.

The pressure-distance curve changes curvature at the lower pressure levels (below 10 psi); i.e., the pressure appears to have decayed at a

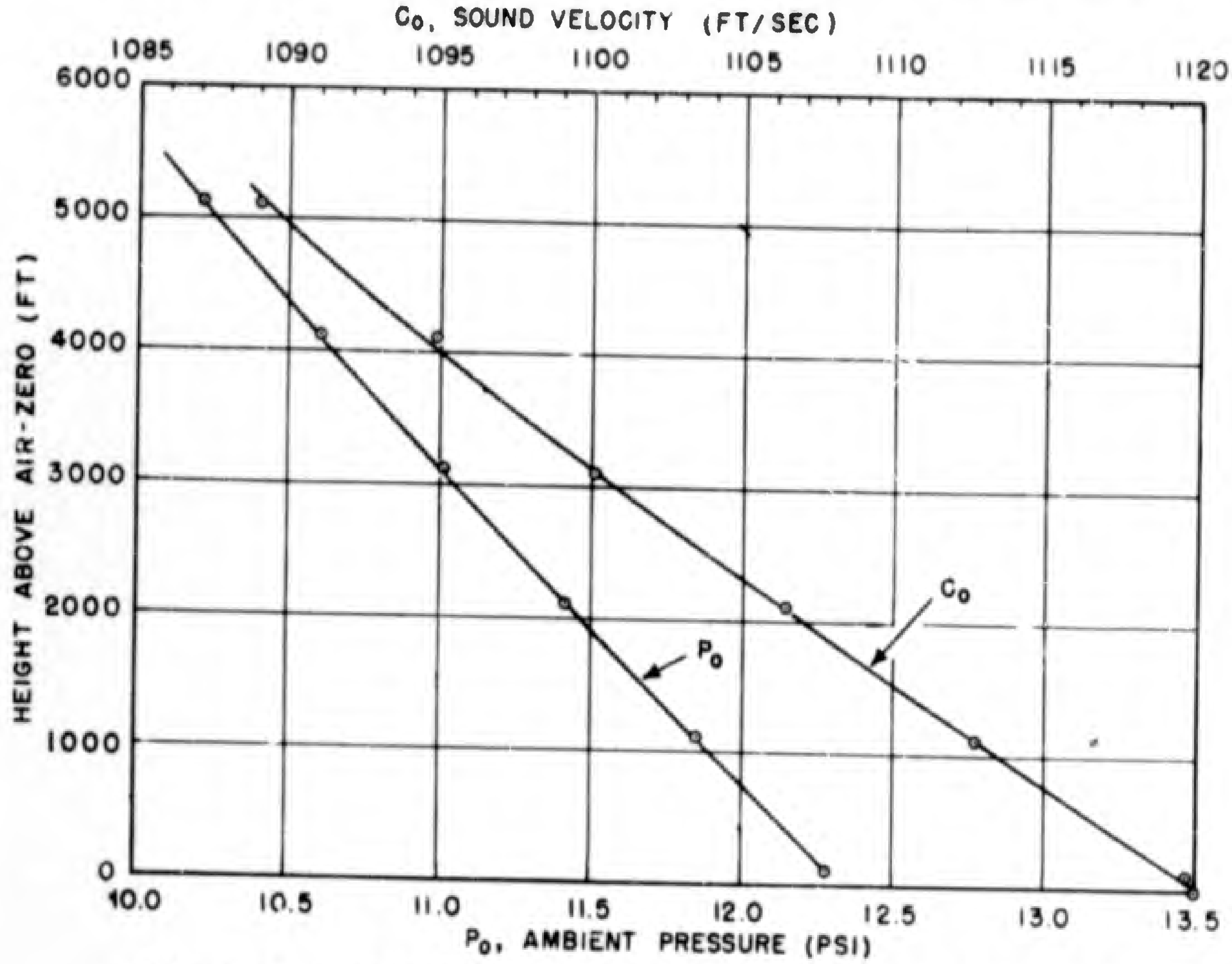

Figure 3.39 Shot 12, Sound Velocity and Ambient Pressure versus Altitude.

greater rate at the lower pressure levels, as was the case on Shot 8, Section 3.5. This is contradictory to what one might expect, since the incident shock should be reinforced by the coalescence of the reflected shock at these pressure levels. It has been noted in the past (Reference 6) that the fitting function could cause such an inflection to occur and is probably the cause in this case (see Sections 3.9 and 4.1.4).

Also measured on Film 28389 were the arrival-time data for the reflected wave. Hooks and breaks were observed in the trails on Shot 12, indicating the position of the reflected wave. These data are given in Table 3.21 and plotted in Fig. 3.36. The arrival-time data for the reflected wave were measured over a range from 1,350 ft to 2,600 ft, where coalescence of the incident and reflected shocks was observed. The reflected wave on Shot 12 was similar to that on Shot 4, although it was slower. The average velocity of the observed reflected

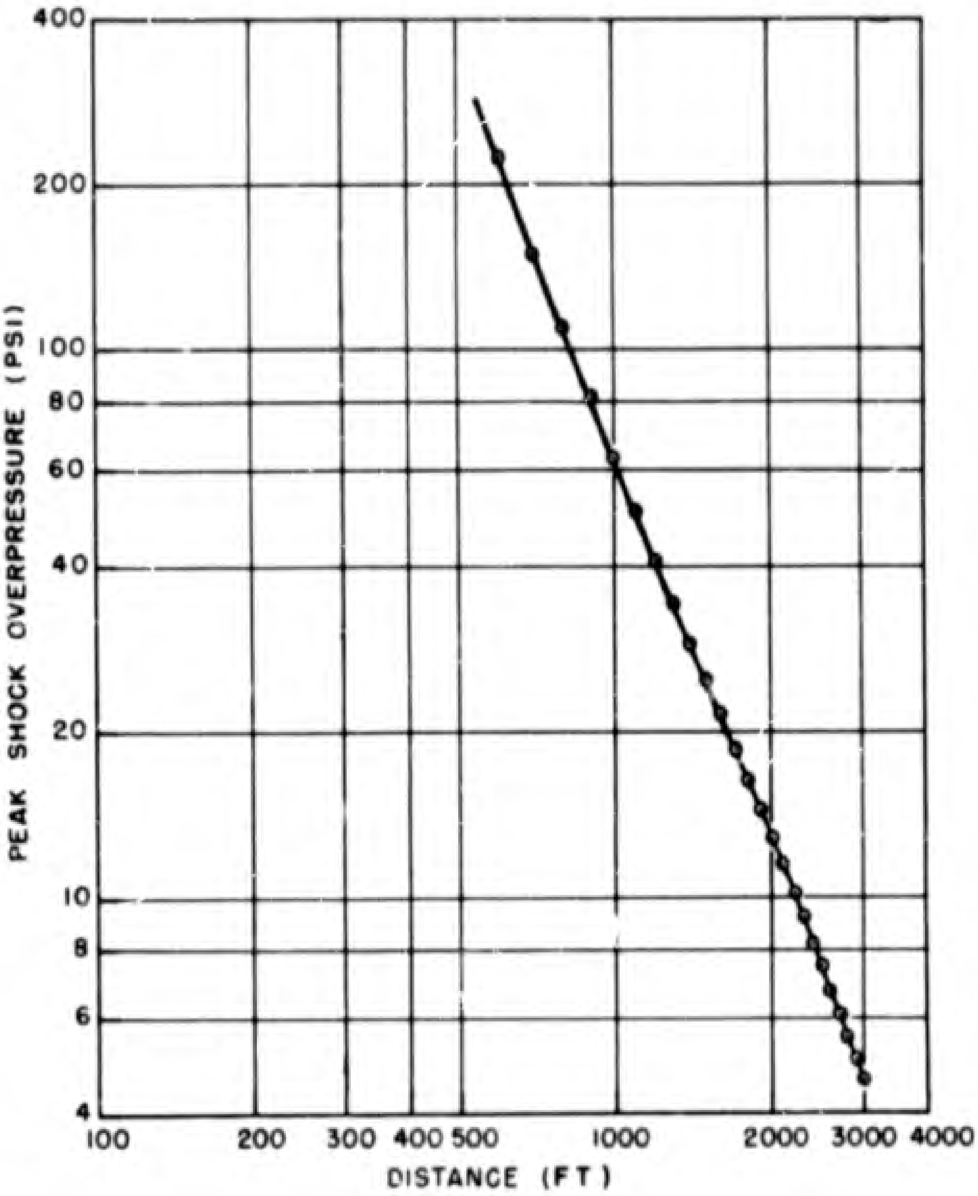

Figure 3.40 Shot 12, Free-Air Peak Shock Overpressure versus Distance.

wave as it approached the incident wave and just prior to coalescence was approximately 2,500 to 3,000 ft/sec. The center portion was greatly accelerated while passing through the region containing the hot gases from the fireball. The shock front contours at the point of catch up are shown in Fig. 3.11. Coalescence occurred over a radius of approximately 1,000 ft horizontally to either side of the vertical.

The reflected wave beneath the fireball was not observed directly, except near the triple point and near the ground just after the incident

[redacted]

shock wave had reached the ground. Just prior to striking the ground, the incident shock appeared to be very flat, almost assuming the shape of a horizontal plane wave in the vicinity of ground zero. Based on past experience, it is impossible to believe that the observed distortion was due to an optical effect alone. This flatness of the incident shock of course affected the reflected wave but to what extent

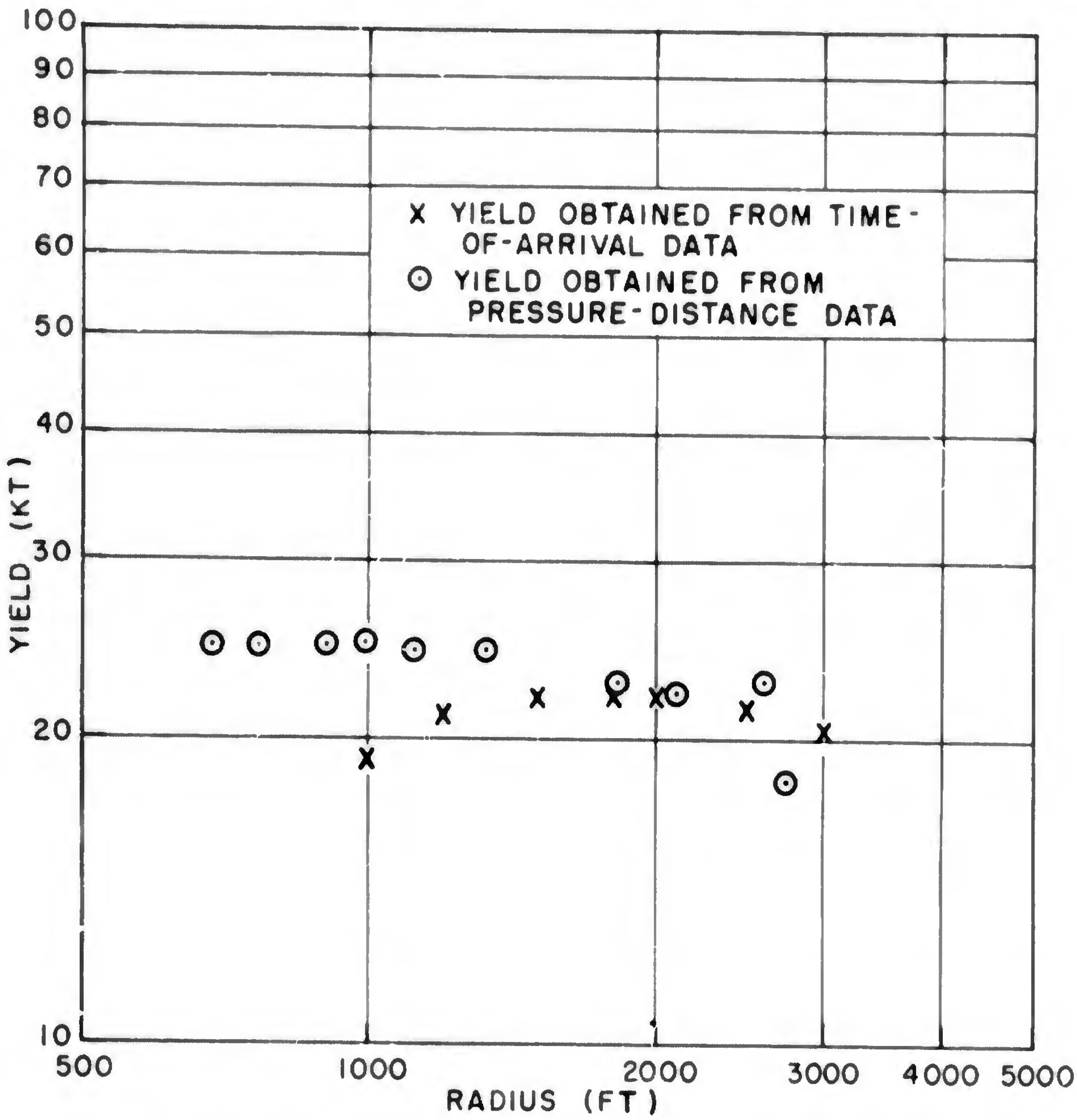

Figure 3.41 Shot 12, Weapon Yield as a Function of Distance from Burst Point.

cannot be determined. Furthermore, how this may have affected shock coalescence above the fireball is equally uncertain.

Closure of the reflected and incident shocks took place at approximately 2,600 ft from air zero (7-psi level). As was noted above, no indication of a reinforcement of the incident shock pressure was observed in this region; therefore, no effective increase in yield, such as that on Shot 4, can be justified for Shot 12. However, the effective yield of the Shot 12 device was determined by the same method employed on Shot 4 (see Section 3.3) and these results are presented in Table 3.22 and plotted in Fig. 3.41.

3.8.2 Direct Shock Photography Data Near the Surface

Measurements of the shock phenomena occurring near the surface were made over all three areas --- desert, water, and asphalt. These

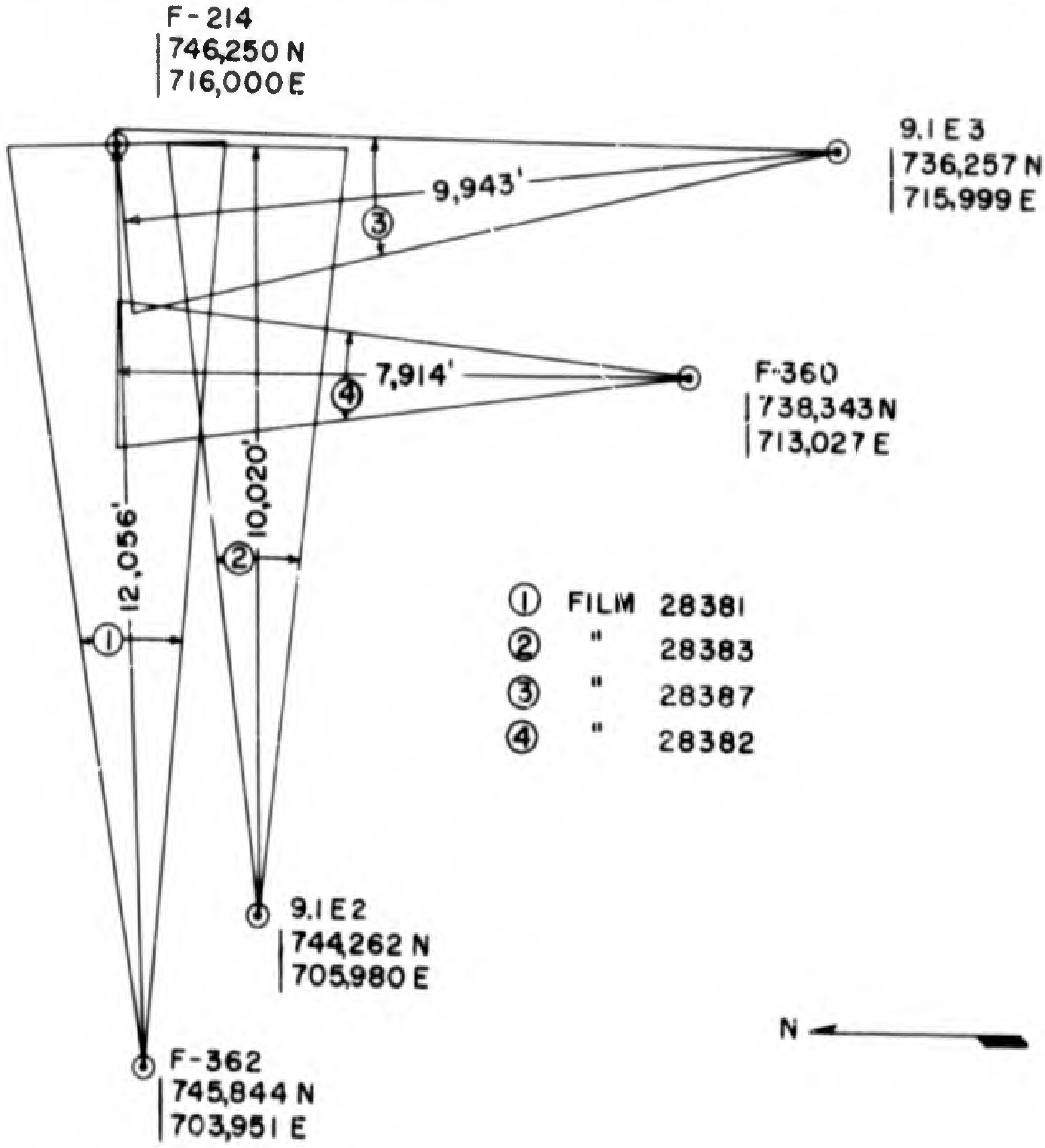

Figure 3.42 Shot 12, Planes of Measurement for Direct Shock Photography.

data were obtained from Films 28381, 28382, 28383, and 28387. The planes of measurement for these films can be found in Fig. 3.42. The results obtained for each area are presented below.

Asphalt Area. A precursor formed over the asphalt area at a ground range of approximately 300 ft and persisted well beyond 3,000 ft

Figure 3.43 Shot 12, Photograph of Shock Along Asphalt 1,430 ft from Ground Zero at t = 0.213 sec (Film 28381).

from ground zero. It was visible on Film 28381 out to a ground range of approximately 1,600 ft and is plainly evident in the photograph taken from this film (Fig. 3.43). Table 2.2 gives the calibration constants for this film. The precursor was also observed from 1,200 to 2,900 ft on Film 28383, although not as clearly as on Film 28381. A dark streak across each frame of Film 28383 masked out all of the wave fronts near the surface; however, the propagation of the dust or smoke following the precursor front was readily observable. This dense cloud of material was lifted and carried by the flow behind the precursor, and its makeup was quite different from that over the desert and water areas. A comparison showed that the data for the arrival time of the initial disturbance, as indicated by the SRI gages (Project 1.10), agreed closely with the data for the arrival time for the dust, as determined from the photographs, i.e., the respective arrival-time curves were nearly identical. Thus the arrival-time data for the precursor along the surface over the asphalt area are given as a continuous set of data from 300 ft to 2,900 ft in Table 3.23 and plotted in Fig. 3.44. In some cases, where structures or other obstructions prevented observation of the precursor or dust front to ground level, the fronts were extrapolated to that level. This was necessary in only a few frames of the film record, and the data are considered highly reliable. Also shown in Fig. 3.44 is the arrival time of the initial disturbance over the asphalt, as measured by Projects 1.10 and 1.12, and there is good agreement for all sets of data (less than 5 percent difference at the maximum).

Measurements of the angle that the precursor front made with the asphalt surface were also obtained, and these data are given in Table 3.24 and plotted in Fig. 3.45. A method for determining the temperature

[redacted]

TABLE 3.21 - Shot 12 - Time of Arrival of Reflected Shock in Free Air

Radius (ft)	Time (sec)
Film 28389	
1,352.760	0.598180
1,409.677	0.647410
1,576.455	0.696640
1,667.786	0.745870
1,781.619	0.795100
1,850.499	0.844330
2,035.758	0.893560
2,213.126	0.942790
2,387.847	0.992020
2,448.734	1.041250
2,512.269	1.090480
2,593.011	1.139710

TABLE 3.22 - Shot 12 - Weapon Yield Versus Distance

Yield Obtained From Pressure - Distance Data		Yield Obtained From Time of Arrival Data	
Distance from Burst (ft)	Weapon Yield (Kt)	Distance from Burst (ft)	Weapon Yield (Kt)
684	24.6	1000	19.0
768	24.6	1200	21.0
905	24.7	1500	22.0
995	24.8	1800	22.0
1,116	24.3	2000	22.0
1,334	24.3	2500	21.5
1,840	22.8	3000	20.5
2,102	22.2		
2,603	22.9		
2,733	18.5		

TABLE 3.23 - Shot 12 - Time of Arrival of the Initial Disturbance Along the Ground (Asphalt Area)

Ground Range (ft)	Time (sec)	Ground Range (ft)	Time (sec)
Films 28381 and 28383			
285.6	0.03675	1,304.9	0.18388
491.7	0.05637	1,345.9	0.19369
586.3	0.06617	1,385.0	0.20350
570.7	0.07598	1,431.0	0.21331
766.6	0.08579	1,470.1	0.22312
812.6	0.09560	1,507.9	0.23293
843.5	0.10541	1,555.2	0.24274
877.8	0.10789	1,586.2	0.26336
895.2	0.11522	1,736.2	0.31194
930.1	0.11760	1,864.3	0.36053
952.5	0.12503	2,020.1	0.40911
988.6	0.12732	2,115.8	0.45770
1,015.6	0.13484	2,215.6	0.50628
1,043.0	0.13704	2,331.4	0.55487
1,087.4	0.14465	2,413.5	0.60345
1,084.3	0.14676	2,486.6	0.65204
1,143.5	0.15446	2,559.3	0.70062
1,109.9	0.15647	2,636.2	0.74921
1,188.3	0.16426	2,698.4	0.79779
1,167.9	0.16619	2,779.4	0.84638
1,225.5	0.17407	2,819.7	0.89496
1,209.7	0.17691	2,891.3	0.94355

[redacted]

[redacted]

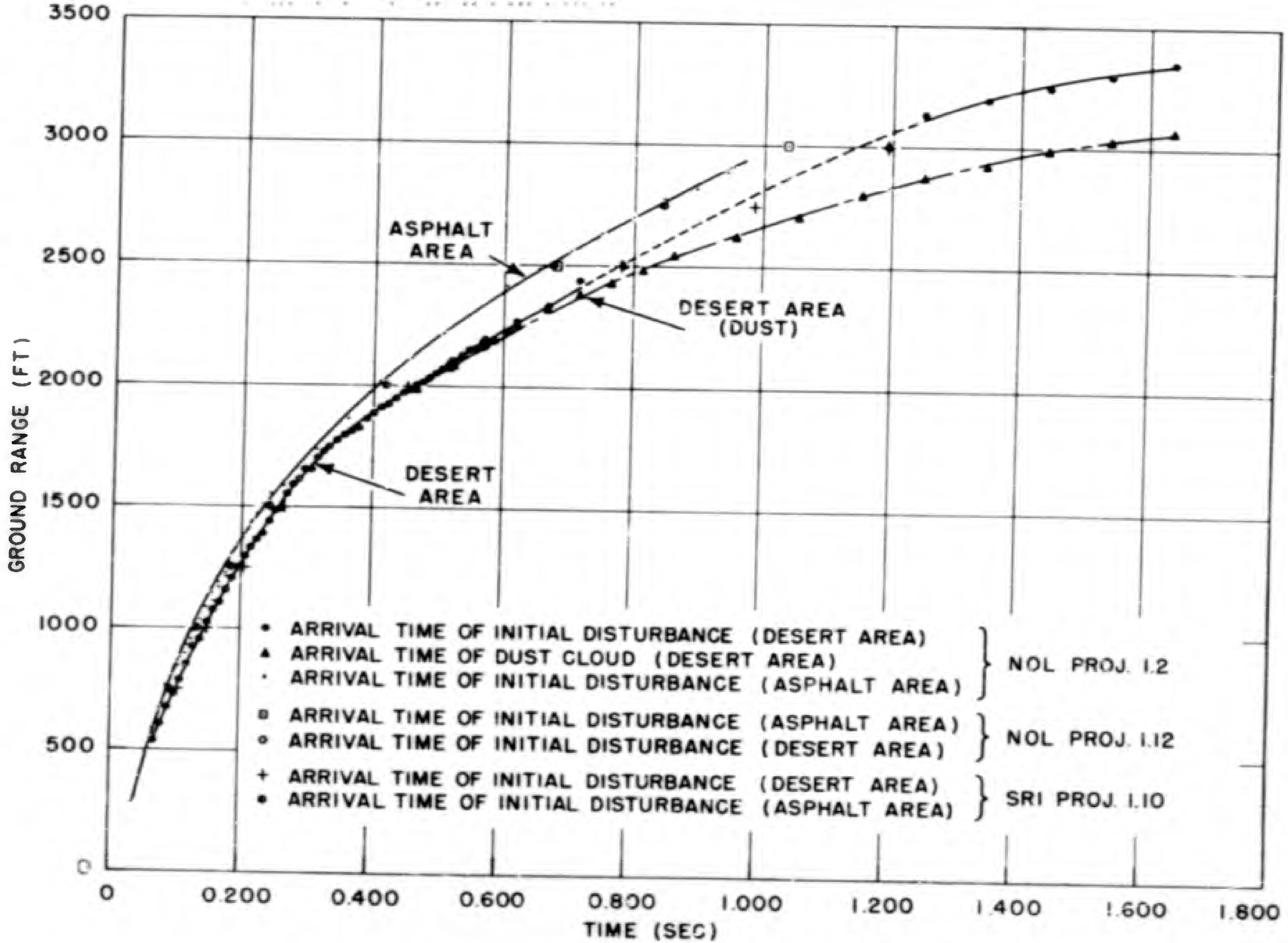

Figure 3.44 Shot 12, Time of Arrival of Initial Disturbance Along the Ground (Asphalt and Desert Areas).

TABLE 3.24 - Shot 12 - Angle of the Precursor as a Function of Ground Range over Asphalt and Desert Areas

Desert		Asphalt	
Angle of Precursor (degrees)	Ground Range (ft)	Angle of Precursor (degrees)	Ground Range (ft)
26.0	545	23.0	646
26.5	679	24.0	764
22.0	852	23.6	942
23.0	963	22.0	1,067
27.8	1,095	24.4	1,210
27.2	1,188	25.0	1,304
29.5	1,306	25.6	1,435
27.9	1,390	26.5	1,519
29.6	1,494	27.9	1,634
28.2	1,575	29.0	1 664
30.5	1,647		
31.0	1,700		
36.0	1,766		
39.5	1,808		
38.5	1,887		
41.5	1,924		
40.5	1,967		
43.8	2,001		
49.5	2,049		
50.0	2,084		
54.5	2,143		
57.5	2,1[illegible]		

of the thermal layer from the angle of the precursor was given in Reference 6. The temperature was calculated from the following equations:

$$\sin \Theta = \frac{C_o}{C_1} \qquad (3.5)$$

where Θ is the angle formed by the precursor front and the surface, and

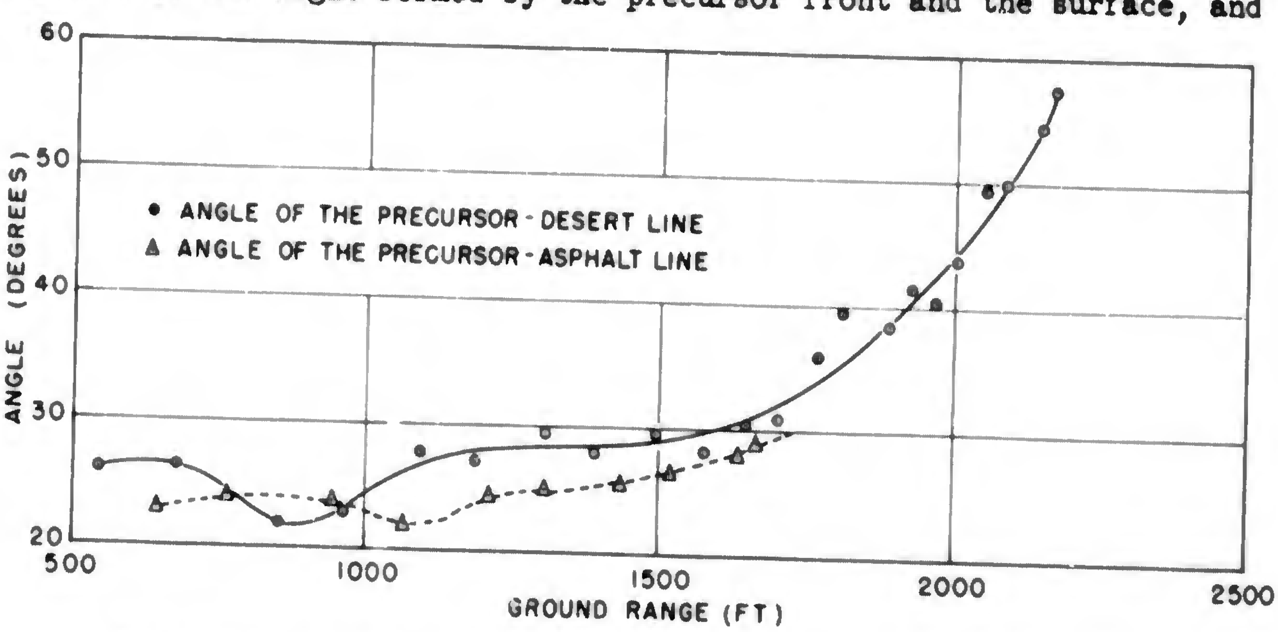

Figure 3.45 Shot 12 - Angle of the Precursor as a Function of Ground Range.

[redacted]

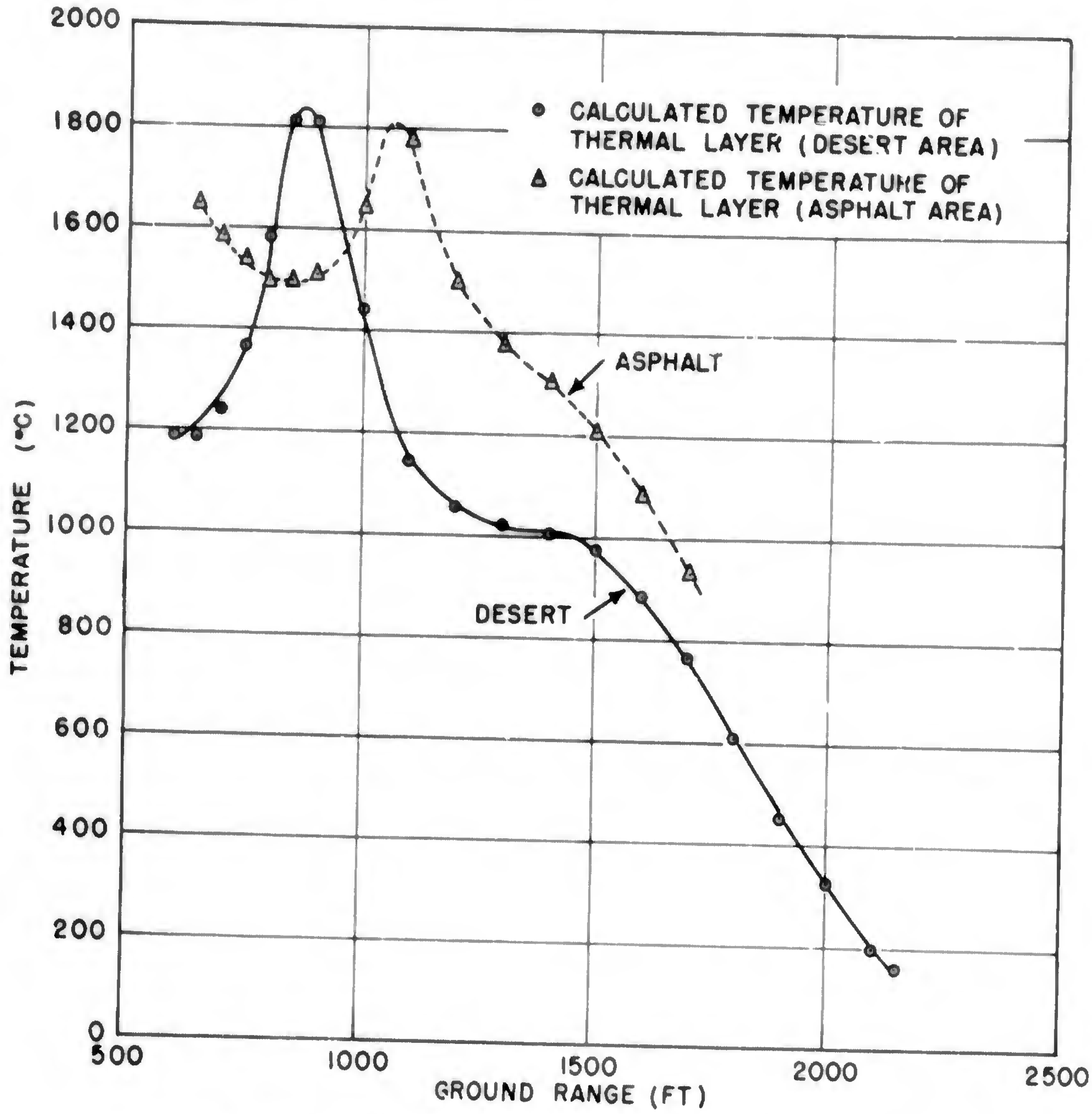

Figure 3.46 Shot 12 - Calculated Temperature of the Thermal Layer as a Function of Ground Range.

C_0 and C_1 are ambient sound velocities existing in the nonheated and heated mediums, respectively. Since,

$$C_1 = C_0 \left(1 + \frac{T_1}{273} \right)^{1/2} \tag{3.6}$$

then T_1 may be calculated by the use of Equations 3.5 and 3.6. This was done, and the resulting temperatures as a function of ground range over the asphalt area are presented in Table 3.25 and plotted in Fig. 3.46. It should be pointed out here that, although the experiments conducted by Projects 8.4e and 1.5 to measure temperature and sound velocities over the three areas on Shot 12 were not conclusive, the differences between the temperatures and sound velocities measured by these projects and those obtained by calculations from the Project 1.2 measurements of the angle of the precursor are extremely large (the calculated temperatures are from four to five times those measured). This may indicate a necessary revision of the method for calculating temperatures from the angle of the precursor.

The triple-point trajectory over the asphalt area was observed over a ground range of from 650 to 1,900 ft. The extension of the triple-point measurements was greatly aided by the rocket smoke grid in the field of view of Film 28383. The height of the Mach stem could be

TABLE 3.25 - Shot 12 - Temperature of Thermal Layer Calculated From Angle of the Precursor Over Asphalt and Desert Areas

Desert		Asphalt	
Ground Range (ft)	Temp of Thermal Layer (°C)	Ground Range (ft)	Temp of Thermal Layer (°C)
600	1,186	650	1,643
650	1,186	700	1,581
700	1,238	750	1,537
750	1,365	800	1,495
800	1,581	850	1,495
850	1,811	900	1,509
900	1,811	1,000	1,643
1,000	1,441	1,100	1,776
1,100	1,146	1,200	1,495
1,200	1,054	1,300	1,377
1,300	1,020	1,400	1,305
1,400	1,003	1,500	1,206
1,500	971	1,600	1,081
1,600	883	1,700	933
1,700	763		
1,800	607		
1,900	453		
2,000	325		
2,100	199		
2,150	161		

measured to over 900 ft, because of this fact. These data are plotted in Fig. 3.47 and listed in Table 3.26.

Water Area. Within the field of Film 28381, the shock propagating over the water area could not be observed all the way to surface level. The precursor and the dust cloud over the desert area obscured the shock over the water area to the extent that it was impossible to determine from the photographs alone whether a precursor formed over the water surface or not. The Mach stem which developed over the water area was clearly visible, and behind it a column of material was observed to reach a height of approximately 200 ft.

The photographs of this material indicate that it was definitely not associated with the desert area (see Fig. 3.48 for an actual photograph taken from Film 28381). The column appears to be composed of a fairly dense material (although not as dense as the dust along the desert line) such as water droplets or smoke. This column lagged farther and farther behind the Mach front as it propagated outward from ground zero. Since the dust obscured the lower part of the Mach front, over a ground range from 500 to 750 ft, that portion of the Mach stem which was visible was extrapolated to the surface. Beyond 750 ft a precursor was observed to precede the Mach stem. This precursor front was then extrapolated to the surface level over a ground range of from 750 ft to 1,350 ft. It is not certain whether this precursor formed over the water or was forced in from adjacent desert areas (unfortunate-

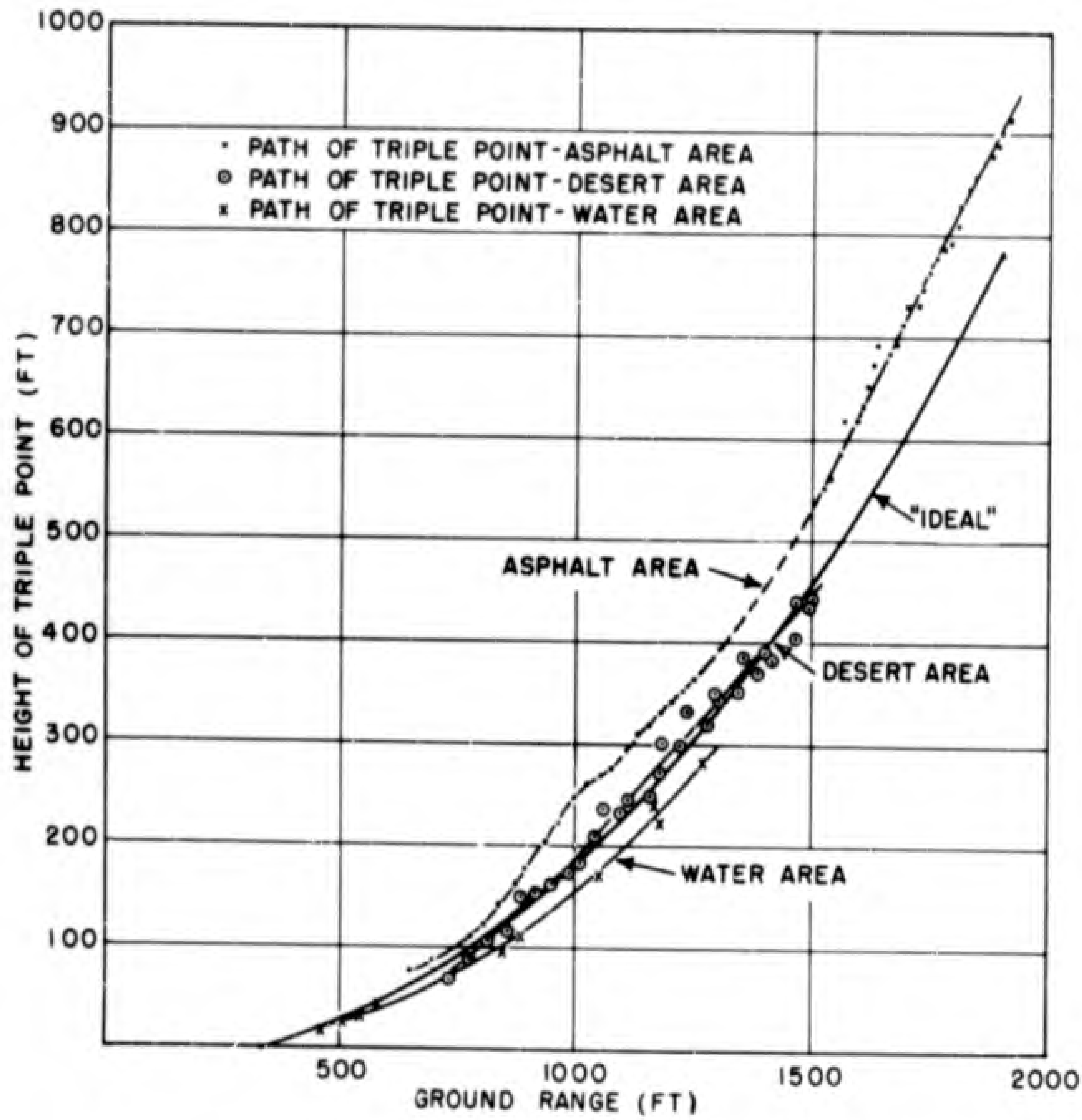

Figure 3.47 Shot 12 - Height of the Triple Point as a Function of Ground Range Over Asphalt, Water and Desert Areas.

ly the aerial films taken for this project were not able to resolve this uncertainty), but the extrapolated arrival-time data for the precursor observed are in good agreement with the measurements made by Project 1.10.

The arrival-time data of the initial disturbance along the water surface are given in Table 3.27 and plotted in Fig. 3.49 (this includes the extrapolated Mach wave from 500 to 750 ft and the extrapolated pre-

TABLE 3.26 - Shot 12 - Height of the Triple Point as a Function of Ground Range

Desert		Asphalt		Water	
Ground Range (ft)	Height (ft)	Ground Range (ft)	Height (ft)	Ground Range (ft)	Height (ft)
729.9	68.6	648.1	75.6	459.6	17.6
775.5	87.3	696.6	86.4	504.3	25.2
812.9	106.5	773.5	109.7	540.3	31.5
857.0	114.3	809.4	121.0	578.1	42.9
881.4	149.6	840.3	138.7	849.8	95.2
914.1	151.7	872.5	160.1	885.1	111.0
947.9	161.0	893.3	174.6	1,009.3	180.9
986.9	172.4	937.4	202.4	1,049.6	171.5
1,010.2	182.3	966.4	220.0	1,168.8	239.6
1,039.8	207.8	996.7	245.2	1,180.1	222.5
1,058.5	236.8	1,021.9	260.4	1,269.0	280.5
1,096.4	232.2	1,050.2	267.3		
1,108.4	245.7	1,076.7	273.6		
1,158.3	249.3	1,103.8	291.9		
1,174.9	271.6	1,129.0	308.9		
1,180.6	301.2	1,154.3	318.4		
1,220.6	298.6	1,178.2	330.2		
1,233.6	333.4	1,200.9	341.7		
1,277.7	319.4	1,229.3	349.2		
1,292.8	349.6	1,250.7	362.5		
1,303.2	341.8	1,521.9	550.0		
1,342.6	351.6	1,537.6	561.0		
1,354.1	385.4	1,554.3	584.5		
1,384.2	370.3	1,563.7	617.4		
1,400.8	391.1	1,590.4	616.9		
1,413.8	383.3	1,602.9	636.2		
1,464.7	405.1	1,614.4	650.4		
1,466.3	441.5	1,626.4	673.4		
1,493.3	436.3	1,633.8	691.7		
1,500.5	442.5	1,656.8	684.9		
		1,673.0	692.7		
		1,686.6	712.6		
		1,696.0	729.3		
		1,719.5	729.3		
		1,728.9	745.0		
		1,743.0	763.3		
		1,757.1	776.9		
		1,772.3	786.8		
		1,786.9	791.0		
		1,802.1	809.3		
		1,809.4	828.6		
		1,825.1	846.4		
		1,839.8	857.4		
		1,873.7	878.3		
		1,887.3	888.8		
		1,896.7	901.8		
		1,912.9	914.9		

cursor front from 750 to 1,350 ft). The photographic arrival-time data and those from Project 1.10 agree to within better than 5 percent.

The trajectory of the triple point over the water area was measured over a ground range of from 450 ft to 1,300 ft, and these data are presented in Table 3.26 and shown in Fig. 3.47.

Beyond a ground range of 1,350 ft, no data were obtained over the water surface. The film which was designed to cover this area was badly

TABLE 3.27 - Shot 12 - Time of Arrival of the Initial Disturbance Along the Ground (Water Area)

Ground Range (ft)	Time (sec)	Ground Range (ft)	Time (sec)
	Film 28381		
475.3	0.05637	997.9	0.16426
507.5	0.06617	1,038.9	0.17407
604.6	0.08579	1,070.4	0.18388
684.0	0.09560	1,096.3	0.19369
690.3	0.10541	1,131.6	0.20350
733.8	0.11522	1,178.8	0.21331
784.8	0.12503	1,200.9	0.23293
865.5	0.13484	1,257.0	0.24274
914.1	0.14465	1,298.6	0.25255
958.2	0.15446	1,328.3	0.26235
		1,362.3	0.27216

streaked with light over the regions of interest. The overexposure masked out all the shock phenomena occurring near the surface.

Desert Area. Propagation of the shock near the ground over the desert area was observed on Films 28387 and 28382 (see Table 2.2 for the film calibration constants). As was expected, a precursor formed over this area that resembled the precursor formed during Shot 10 of Operation UPSHOT-KNOTHOLE to a remarkable degree (see reference 6). The precursor over this area was first observed from approximately 500 ft; it persisted out to a ground range well beyond 3,000 ft. It was markedly different from that formed over the asphalt area. Figure

Figure 3.48 Shot 12, Photograph of Shock Along Water 1,000 ft from Ground Zero at t = 0.164 sec (Film 28381).

3.50 shows an actual photograph (taken from Film 28387) of the precursor propagating over the desert area. The front of the precursor over the desert area was steeper and its propagation along the ground slower than the precursor over the asphalt area (lagging by approximately 35 msec at 1,500 ft). The arrival-time data of the initial disturbance along the desert surface over a range of from 500 to 3,350 ft are presented in Table 3.28 and plotted in Fig. 3.44. On Film 28382 it was impossible to detect the shock front from a ground range of 2,450 to 3,100 ft. At 3,100 ft the shock front passed a smoking blast-line pole and was again detectable out to 3,350 ft ground range. The arrival-time curve

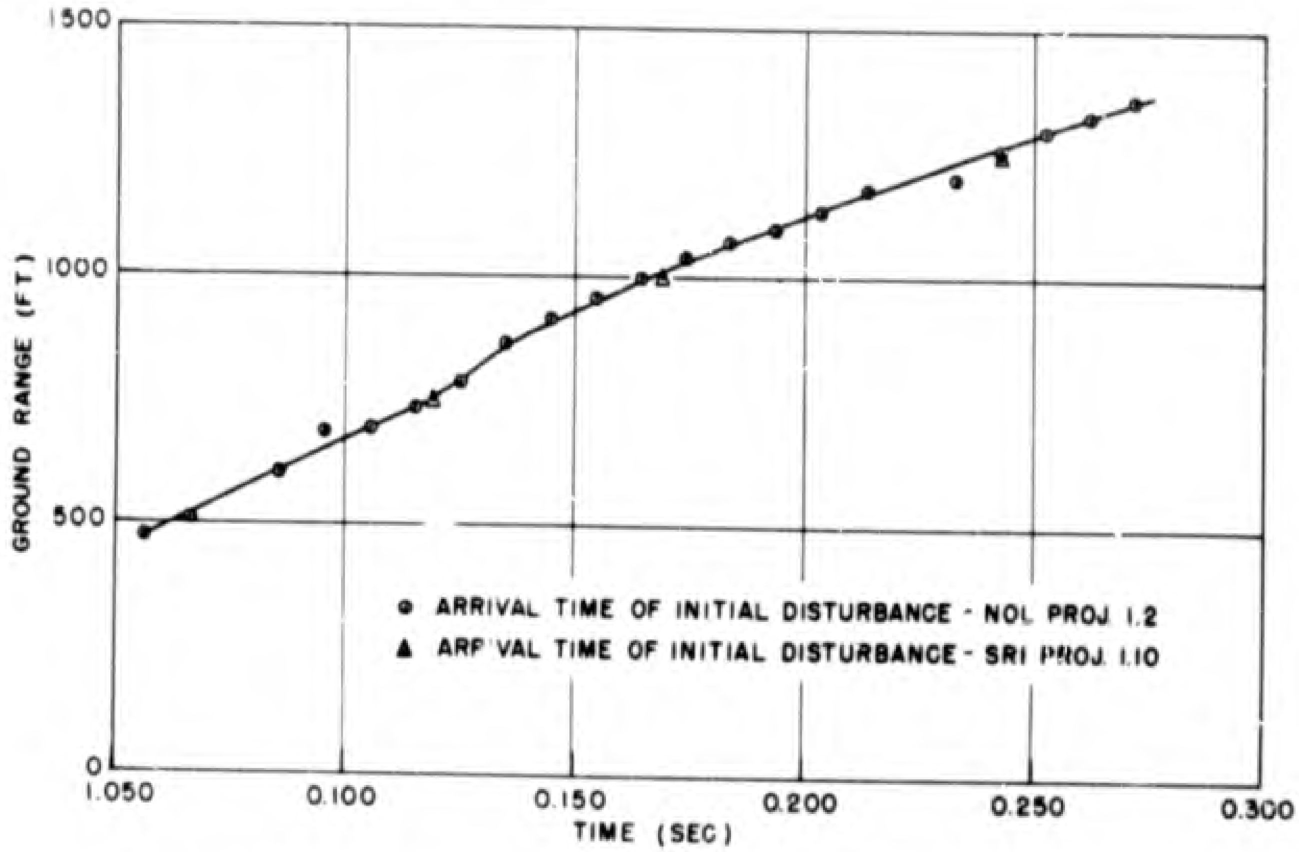

Figure 3.49 Shot 12, Time of Arrival of the Initial Disturbance Along the Ground (Water Area).

shown in Fig. 3.44 was extrapolated over the interval where the shock front could not be detected. Also plotted in Fig. 3.44 are the arrival-time data of the initial disturbance over the desert area, as measured by Projects 1.10 and 1.12. Out to a ground range of 2,500 ft the agreement is exceptionally good (less than 5 percent difference in all cases). However, beyond this region the agreement, though not as good, is within the range of difference that could possibly be accounted for by the asymmetry of the precursor observed throughout the region. Following the precursor, a dust cloud rose to a height of approximately 250 ft and was apparently coincident with the arrival time of the precursor out to a ground range of 1,900 ft. Beyond this ground range, the dust cloud began to lag behind the precursor front, and it ceased to propagate horizontally at about 3,100 ft. A plot of the dust arrival-time data beyond 1,900 ft is presented in Fig. 3.44.

The angle that the precursor front made with the surface over this area was also measured, and these data are presented in Table 3.24 and plotted in Fig. 3.45. Temperatures calculated from these data in the

TABLE 3.28 - Shot 12 - Time of Arrival of the Initial Disturbance Along the Ground (Desert Area)

Ground Range (ft)	Time (sec)	Ground Range (ft)	Time (sec)
Film 28387			
537.6	0.06707	1,889.0	0.40061
607.7	0.07739	1,912.4	0.41201
675.2	0.08735	1,927.0	0.42341
732.4	0.09731	1,950.3	0.43481
784.3	0.10727	1,972.2	0.44621
852.8	0.11723	1,985.7	0.45620
924.5	0.12717	2,007.5	0.46619
956.7	0.13715	2,019.4	0.47618
1,023.2	0.14711	2,037.1	0.48617
1,075.2	0.15707	2,055.8	0.49616
1,106.3	0.16703	2,072.4	0.50615
1,155.7	0.17622	2,091.6	0.51614
1,206.6	0.18541	2,106.2	0.52613
1,251.8	0.19460	2,128.5	0.53612
1,295.9	0.20379	2,151.9	0.54611
1,334.3	0.21298	2,159.1	0.55610
1,366.0	0.22217	2,177.3	0.56609
1,390.4	0.23136	2,183.6	0.57608
1,441.3	0.24055	2,190.8	0.58607
1,485.5	0.24974	2,228.2	0.60605
1,495.9	0.25893		
1,558.2	0.26809	Film 28382	
1,590.9	0.27725		
1,616.4	0.28641	2,104.3	0.52400
1,654.3	0.29557	2,192.8	0.57048
1,653.2	0.30473	2,269.7	0.61856
1,702.1	0.31389	2,336.2	0.66744
1,729.1	0.32305	2,437.1	0.71592
1,749.3	0.33221	3,136.6	1.24920
1,774.8	0.34361	3,193.9	1.34616
1,799.2	0.35501	3,247.9	1.44312
1,815.3	0.36641	3,298.6	1.54008
1,828.3	0.37781	3,347.6	1.63704
1,864.6	0.38921		

same manner as described for the asphalt area results are listed in Table 3.25 and shown in Fig. 3.46.

The height of the Mach stem as a function of ground range over the desert area was also obtained. Table 3.26 lists these data, and Fig. 3.47 shows a plot of the trajectory of the triple point over this area.

<u>Comparison of Results of Asphalt, Desert, and Water Areas.</u> Over the asphalt and desert area, a precursor was observed to form at approximately 300 and 500 ft, respectively. Since the water area was obscured by the dust along the desert, it cannot be ascertained whether the observed precursor formed over this area or was the result of feed-in effects. A more complete discussion of this is presented in Chapter 4.

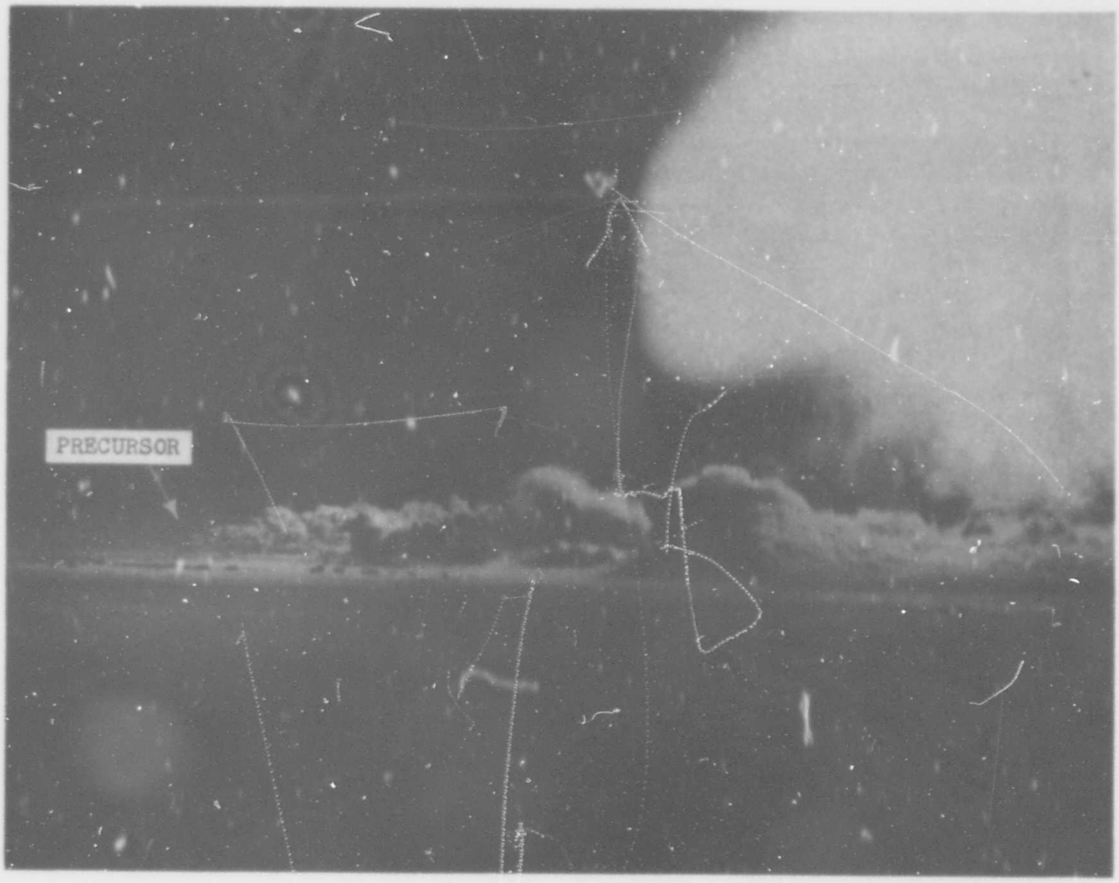

Figure 3.50 Shot 12, Photograph of Shock Along Desert 1,750 ft from Ground Zero at t = 0.332 sec (Film 28387).

The precursor formed over the desert propagated at a slower velocity along the ground and at a steeper angle than over the asphalt area. In all three areas near the ground, the blast was loaded with some material raised by the passage of the shock or precursor along the surface. Over the desert area this cloud was apparently composed of sand and dust particles. Although the water area could not be observed at ground level, it appears on the film that water particles rose to a considerable height behind the Mach stem; however, the extent of the water column is extremely small, compared to the dust cloud raised over the desert area. Over the asphalt area the cloud of material immediately behind the precursor appeared to be entirely different from that over either of the other two areas. Presumably, it was composed of a mixture of particles of smoke and dust. Temperatures calculated from the angle of the precursor show that the maximum temperatures over the asphalt and desert areas were approximately the same; however, for corresponding ground ranges, the temperatures were higher along the asphalt than along the desert line. Comparison of the path of the triple point over the three areas indicates that the Mach stem grew much faster over the asphalt area than over the other two areas.

The path of the triple point over the desert area, when plotted graphically, fell between those for the water and asphalt areas. The

TABLE 3.29 - Project 1.2 - Shock Photography Films

Shot	Film	
1	28881 28882 28883 28884 28885 28886 28887	No timing on any films. Precursor measurements made on Film 28881. Very good films showing shock phenomena near the ground. No free-air data can be obtained. Films 28885 and 28886 show cloud rise but no shocks can be observed.
3	28681 28682 28683 28684	All films were badly overexposed. Only qualitative information can be obtained from these films.
4	28180 28181 28182 28183 28184 28185 28186 28187	Free-air data obtained from 28183 and 28184. Reflected wave observed on Film 28184. Measurements along the ground obtained from 28183 and 28184. Films 28185, 28186, and 28187 show good detail of shock phenomena near ground zero. Film 28187 shows triple point out to end of rocket grid. Excellent films.
6	28080 28081 28082 28083 28084 28085 28086 28087	Precursor measurements made on Films 28081 and 28084. Free-air data in the fireball stage and the early stages of the shock after breakaway were obtained from Film 28080 although the speed of this film does not remain constant. Exposures of films 28082 and 28083 were too heavy to obtain measurements.
8	28280 28281 28282 28283 28284 28287	Shock phenomena in free-air and along the ground measured on Films 28282 and 28284. Film 28280 shows early shock formation in free-air and good detail of shock phenomena near the ground in the vicinity of ground zero.
9	29382 29383 29384 29385 29386	Shock phenomena near the ground were measured on Film 29384. All films were slightly overexposed but good detail of the shock near the ground could be observed. Films 29385 and 29386 show the early motion of the cloud.
10	28980 28981 28982 28985 28986 28987	Lack of contrast on all films makes the detection of the shock front very difficult. Films 28980 and 28982 are the best. All measurements were made from Film 28980.
12	28380 28381 28382 28383 28384 28385 28386 28387 28388 28389 28390 28391	Free-air measurements were made from Films 28389 and 28390. Film 28390 shows free-air shock best. Ground measurements made from Films 28381, 28382, 28383 and 28387. Film 28381 shows propagation of shock over asphalt and water areas. Film 28383 shows propagation of shock over asphalt, however a dark streak across center of frame obliterates most of shock fronts. Films 28387 and 28382 show shock propagating along the desert. Film 28387 appears to be slightly out of focus.

cause for these differences is not fully understood. Most likely, the differences in reflection coefficients for the three different surfaces and the large differences in the thermal layers above them gave rise to the differences in formation of the thermal Mach waves and their subsequent growth.

3.9 ACCURACY OF RESULTS

The sources of possible errors and the procedures for computing their magnitudes in the methods employed to find pressure as a function of distance by the smoke rocket shock velocity technique have been covered extensively in References 1 and 2.

The six major sources of error stem from (1) the static and dynamic resolution uncertainties associated with film measurements under optimum conditions, (2) failing to correct for foreshortening in the image plane, (3) improper scaling of distance on the film, (4) improper time calibration, (5) improper curve fitting, and (6) use of improper values of the atmospheric pressure, P_o, and sound velocity, C_o, for the region in front of the shock in pressure computations.

Throughout the analyses of the free-air data, care was taken to hold the above-listed errors to a minimum. Except for Shot 10, the distance measurements fell within a maximum uncertainty of ± 2.0 ft and measurements of time per frame to within a maximum uncertainty of ± 0.00005 sec. In the case of Shot 10, a different method had to be used to detect and measure the locus of the shock front, a method which leads inherently to greater uncertainties in the values of the time-of-arrival data than the method used for the other shots. The uncertainties associated with the Shot 10 data were estimated in Section 3.7.

The calculated pressures for all shots reported are considered to be accurate to 3 percent down to the 15-psi level. Below the 15-psi level, the pressure for Shot 4 is considered to be good to 5 percent. Pressures on Shots 8 and 12 below the 15 psi level may be in greater error but are estimated to be accurate to within 10 percent. (Note the discussion in Section 4.1.3.)

Uncertainties in the direct-shock-photography data are of the same order of magnitude as those for the free-air smoke-rocket data, except for the measurements of triple-point height and the measurements of the angle of the precursor. The uncertainty associated with these data is probably of the order of ± 5 percent.

Chapter 4
DISCUSSION

4.1 FREE-AIR SHOCK PHENOMENA

4.1.1 Shock-Wave Coalescence, Arrival-Time Data

Concerning the study of the coalescence of the reflected shock with the incident shock vertically above the burst, it was pointed out in Chapter 3 that on Shots 4 and 12 the reflected wave overtook the incident wave, but on Shot 8 the reflected wave was not observed above the fireball, because of the low quality of the film records (improper exposure because of the unexpectedly low yield of the Shot 8 device). A careful analysis of the vertical arrival-time data has shown that only on Shot 4 was there a distinct increase in the shock velocity following coalescence at approximately 2,550 ft from the burst point. On Shot 12, coalescence was clearly observed at approximately 2,600 ft from the burst point, but no corresponding increase in velocity could be detected. If at all, the change in velocity was negative. Similarly, on Shot 8, no distinct increase in velocity was observed out to the limit of the data at 2,520 ft. It is plausible to assume for Shot 8, however, that coalescence had not yet occurred, since it did not take place for the more-favorable conditions of Shot 12 (larger yield and lower burst height) until the distance of about 2,600 ft was reached.

In the analysis of the arrival-time data for these three shots, it was observed that, when the data were scaled to a common yield basis for comparison the Shot 4 data beyond the fireball region were consistently slightly higher than those for Shots 8 and 12, between which there was an apparent but insignificant difference. A small percentage difference between the actual yield and the stated yield would account for this. However, following the point of coalescence, the Shot 4 arrival-time data became markedly higher. Assuming the stated yields to be accurate and taking the extreme values for data uncertainty into consideration, the increased velocity of the coalesced wave on Shot 4 was found to be significant and is believed to be real. Why a similar increase was not detected in the Shot 12 data is difficult to understand, unless an actual increase that may have occurred was so small that it fell within the experimental error and could not be recognized.

Another fact to be considered in connection with the observed shock coalescence on Shots 4 and 12 is that, prior to coalescence, the reflected wave velocities ranged from 2,500 to 4,000 ft/sec. At coalescence on Shot 4, the velocity of the reflected wave was significantly greater than that of the incident wave, while on Shot 12 the respective velocities were approximately the same. This information is consistent with the remarks made above and may serve, in part, to explain the existence and nonexistence of the velocity increase in the respective cases of shock coalescence (see also Section 4.1.2).

A primary significant difference between these shots, and one which must certainly affect the behavior of the reflected wave, is that on Shot 4 the fireball intersected the ground plane, whereas this did not occur on Shots 8 or 12. Relatively little can be said quantitatively about shock transmission through the intensely heated fireball region. However, it is certain that the shock front accelerates upon entering this region*, and by this mechanism it is sometimes enabled to overtake the incident wave vertically above the burst. Therefore the initial conditions for the occurrence of coalescence must depend markedly, but not solely, on the scaled height of burst.

4.1.2 Shock-Wave Coalescence, Calculated Pressures

The foregoing remarks have been limited to a discussion of arrival-time and shock-velocity data for Shots 4, 8, and 12. These data are the fundamental results of the experiment and provide the basis for the calculation of the shock pressures as a function of distance. It was pointed out that the velocity of the reflected wave front is accelerated in passing through the intensely heated fireball region, but nothing was said about the pressure in the wave. Laboratory, field, and theoretical studies (References 6, 11, 12) have shown that, when a shock wave enters a region in which the local sound speed is equal to or greater than the shock velocity, the shock deteriorates; that is, the rise to peak pressure is no longer instantaneous but, rather, the rise time is increased and the pressure-time representation of the wave appears rounded. The wave front accelerates rapidly to acclimate itself, as it were, to its new surroundings. Shock-tube studies (Reference 12) have shown that weak shocks, upon passing into a region of heated gas, lose their ability to refract light to such an extent that they cannot be detected photographically. Pressure-gage records lend further support to the observation of wave-front deterioration described above.

Direct shock photography on full-scale nuclear tests has shown that the reflected wave is sufficiently strong to distort the spherical shape of the fireball, causing the lower portion to become concave

---

* Direct shock photography of many near-surface atomic bursts has shown that the reflected wave loses its normal sphericity in the region directly beneath the fireball and that this portion of the wave is accelerated upward. Rate of acceleration and nonsphericity increases as the burst height decreases. Acceleration of the central portion of the wave has been observed to start in many instances well below the actual fireball, indicating that sufficient radiation is absorbed by the air to cause it to heat up with a corresponding increase in local sonic speed. Such heating of the air is the only plausible explanation for the photographic evidence of reflected shock acceleration in this region well outside of the fireball.

inward with respect to the spherical surface (Reference 13). In the light of these observations, it is difficult to understand why the uppermost portion of the fireball is not also pushed out of shape as the reflected shock leaves the fireball region; yet little, if any such distortion has ever been detected on any atomic burst. It would appear as though the particle motion behind the reflected wave were almost completely attenuated during its passage through the fireball. The accelerated central portion of the wave front has been observed well within the fireball by direct shock photography, but it disappears before reaching the fireball center and is not detected again until it has passed well beyond the uppermost portion of the fireball. It has been detected in this latter region only with the aid of the rocket smoke trails, and even then the observed refraction of the smoke grid is extremely weak by comparison with that produced by the incident wave. In other words, the high-velocity front apparently is not accompanied by a correspondingly high pressure.

From these arguments it is possible to hypothesize that the reflected shock wave, although very strong at its origin, is rapidly distorted and weakened during its passage through the intensely heated fireball region, while at the same time its velocity is increased. Because the local sonic speed within the fireball exceeds the speed of the shock entering it, the "shock" cannot be considered to be more than a rapidly attenuated, slow-rising pressure pulse while it traverses this region. The pressure wave is confronted by new conditions as it leaves the fireball, and these are such as to cause it to "shock up" again, although slowly, since its peak pressure has decayed somewhat and the air through which it passes appears cooler to it gradually. Whether the wave becomes a shock before it overtakes the incident shock or not, so long as it is sufficiently positive with respect to P_o, the ambient atmospheric pressure, an increase in pressure in the coalesced shocks should result.

On Shot 4 the calculated pressures of the shock wave following coalescence were noticeably larger than those taken from the standard, composite free-air pressure-distance curve. This would follow logically from the observed velocity increase upon shock coalescence referred to in the previous section. On Shot 12, however, the reflected wave was observed to overtake the incident wave very gradually, and the difference in their respective velocities was negligible. Nevertheless, if the pressure in the reflected wave had been sufficiently greater than P_o, a net increase in the coalesced wave should have been detected. Since no jump in velocity was observed on Shot 12, it must be concluded that the pressure in the reflected wave was very low, i.e., almost atmospheric. (See also the remarks in the following section.)

4.1.3 Comparison of Pressure-Distance Data with the Standard Free-Air Curve

The pressure-distance data for Shots 4, 8, and 12 have been scaled to 1 KT (RC) at sea level (see Table 1.1 for the scaling factors) and are given in Tables 4.1, 4.2, and 4.3, respectively. Figures 4.1, 4.2, and 4.3 compare these scaled data with the composite free-air curve, (Reference 6).

It can be seen in Fig. 4.1 that Shot 4 exhibited the same effect that has been observed on certain previous tower shots such as UPSHOT-KNOTHOLE Shot 1, Reference 6, and GREENHOUSE Easy, Reference 1, namely, the appearance of above-average pressures at the larger distances. (The average pressure is taken as that indicated by the composite free-air pressure-distance curve.) On the other hand, Shots 8 and 12 exhibited below-average pressures at the larger distances, as shown in Figs. 4.2 and 4.3, respectively. Similar "low" results were also observed on Operation UPSHOT-KNOTHOLE. In Reference 6, these deviations from the composite curve - which, it should be noted, is based only on air-drop shots and not tower shots - were attributed to the statistical method used in fitting the basic shock-arrival-time data. Renewed examination of this problem has led to a reversal of opinion.

As Reference 6 points out, the shock velocity, taken as a function of distance, should approach a constant value asymptotically at the larger distances. This limiting value should be nearly that of the ambient speed of sound. In Equation 1.2, the constant *a* is the asymptote of the velocity function derived from the basic fitting function, Equation 1.1, and should therefore closely approximate the sonic speed value. At one time, several attempts were made to hold the value of *a* fixed and equal to the observed sonic speed, but it was found that when this was done, a good statistical fit to the basic arrival-time data could not be obtained. Since that time, the value of *a*, along with the values of *b* and *c*, all constants of the fitting function, has been allowed to vary to obtain the function best representing the measured data.

The point to be stressed here is that the value of *a* is controlled by the data, but when its value is about equal to or higher than the observed sonic speed, the shock velocities at large distances, and hence the shock pressures, are usually found to be higher than the average. Similarly, when *a* is somewhat lower than sonic speed, the resulting computed pressures are usually lower than average at the larger distances.

The values for *a* for Shots 4, 8, and 12 are given in Sections 3.3, 3.5, and 3.8, respectively. Compared to the ambient sonic speeds which obtained at the time of burst, these values are found to differ as follows: Shot 4 - 0.8 percent low; Shot 8 - 12 percent low; and Shot 12 - 14 percent low. If it is accepted that a difference between the value of *a* and that of the sonic speed of less than 1 percent is negligible, then the pattern outlined above is maintained*.

The reasons why various shots behave as they do in this manner is not understood. The question as to whether incident and reflected

---

* No explanation can be given for the fact that on Shot 10, the scaled pressures agreed well with those of the composite free-air curve despite the fact that *a* was 30 percent lower than sonic speed at altitude.

(Continued on Page 102)

TABLE 4.1 - Shot 4 - Scaled Free-Air Pressure-Distance Data

Data Scaled to Sea Level		Data Scaled to 1 kt at Sea Level	
Distance (ft)	Peak Overpressure (psi)	Distance (ft)	Peak Overpressure (psi)
562	421.9	160	421.9
655	288.1	187	288.1
748	205.6	214	205.6
841	155.8	239	155.8
933	122.1	266	122.1
1,024	98.4	293	98.4
1,116	82.3	318	82.3
1,208	69.0	344	69.0
1,299	58.6	371	58.6
1,390	51.2	396	51.2
1,482	44.9	422	44.9
1,571	40.0	449	40.0
1,661	35.7	473	35.7
1,752	32.2	500	32.2
1,842	29.3	526	29.3
1,932	26.8	550	26.8
2,022	24.5	576	24.5
2,111	22.6	603	22.6
2,201	20.9	629	20.9
2,290	19.4	652	19.4
2,379	18.2	679	18.2
2,468	17.0	705	17.0
2,556	16.0	728	16.0
2,645	14.9	754	14.9
2,730	14.1	780	14.1

TABLE 4.2 - Shot 8, Scaled Free-Air Pressure-Distance Data

Data Scaled to Sea Level		Data Scaled to 1 Kt at Sea Level	
Distance (ft)	Peak Overpressure (psi)	Distance (ft)	Peak Overpressure (psi)
377.2	492.3	156.0	492.3
471.5	274.8	195.0	274.8
565.8	172.0	234.1	172.0
660.1	119.1	273.1	119.1
754.4	85.4	312.1	85.4
848.7	65.3	351.1	65.3
943.0	51.4	390.1	51.4
1,037.3	41.7	429.1	41.7
1,131.6	34.3	468.1	34.3
1,225.9	28.8	507.1	28.8
1,320.2	24.5	546.1	24.[illegible]
1,414.5	20.9	585.2	20.9
1,508.8	18.2	624.2	18.2
1,603.1	15.7	663.2	15.7
1,697.4	13.9	702.2	13.9
1,791.7	12.2	741.2	12.2
1,886.0	11.0	780.2	11.0
1,980.3	9.6	819.2	9.6
2,074.6	8.6	858.2	8.6
2,168.9	7.7	897.2	7.7
2,263.2	6.8	936.2	6.8
2,357.5	6.2	975.2	6.2

[redacted]

TABLE 4.3 - Shot 12 - Scaled Free-Air Pressure-Distance Data

Data Scaled to Sea Level		Data Scaled to 1 Kt at Sea Level	
Distance (ft)	Peak Overpressure (psi)	Distance (ft)	Peak Overpressure (psi)
561.8	272.0	200.5	272.0
654.8	183.8	233.7	183.8
747.3	133.7	266.7	133.7
839.7	100.0	299.7	100.0
931.7	78.6	332.5	78.6
1,023.8	62.3	365.3	62.3
1,115.3	51.1	398.0	51.1
1,206.8	42.8	430.7	42.8
1,298.2	36.2	463.3	36.2
1,389.3	31.2	495.8	31.2
1,479.8	27.0	528.2	27.0
1,570.5	23.6	560.5	23.6
1,661.0	20.7	592.7	20.7
1,751.2	18.4	625.1	18.4
1,840.8	16.4	657.0	16.4
1,930.5	14.7	689.0	14.7
2,020.0	13.2	720.9	13.2
2,109.3	11.9	752.8	11.9
2,198.4	10.8	784.6	10.8
2,286.8	9.8	816.0	9.8
2,375.4	8.9	847.9	8.9
2,463.8	8.1	879.4	8.1
2,551.9	7.4	910.8	7.4
2,639.9	6.7	942.2	6.7
2,727.0	6.2	973.2	6.2

TABLE 4.4 - Shot 10 - Scaled Free-Air Pressure-Distance Data

Data Scaled to Sea Level		Data Scaled to 1 Kt at Sea Level	
Distance (ft)	Peak Overpressure (psi)	Distance (ft)	Peak Overpressure (psi)
180.8	1,027.1	121.5	1,027.1
241.1	474.8	162.0	474.8
301.4	254.3	202.4	254.3
361.7	157.5	242.9	157.5
422.0	107.3	283.4	107.3
482.2	76.7	323.9	76.7
542.5	58.0	364.4	58.0
602.8	44.7	404.9	44.7
663.1	35.2	445.4	35.2

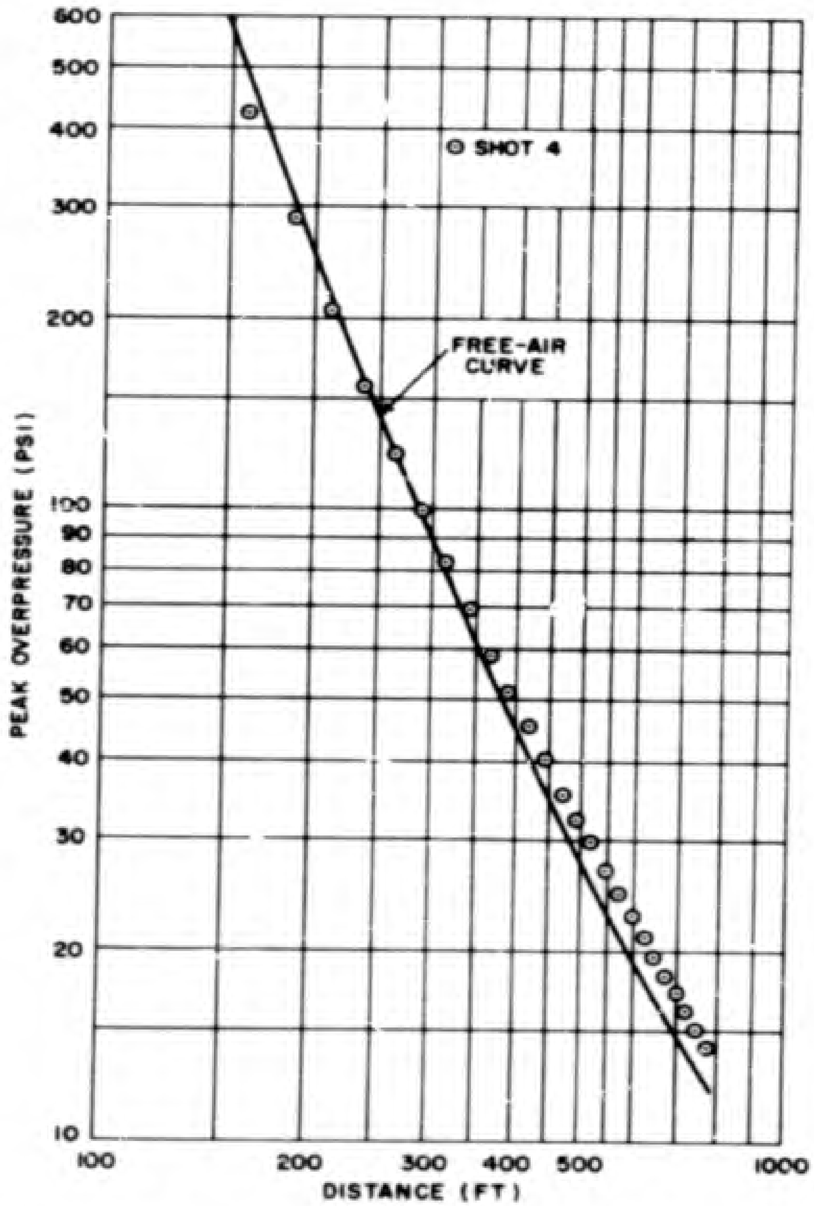

Figure 4.1 Shot 4, Pressure versus Distance Reduced to 1 KT (RC) at Sea Level.

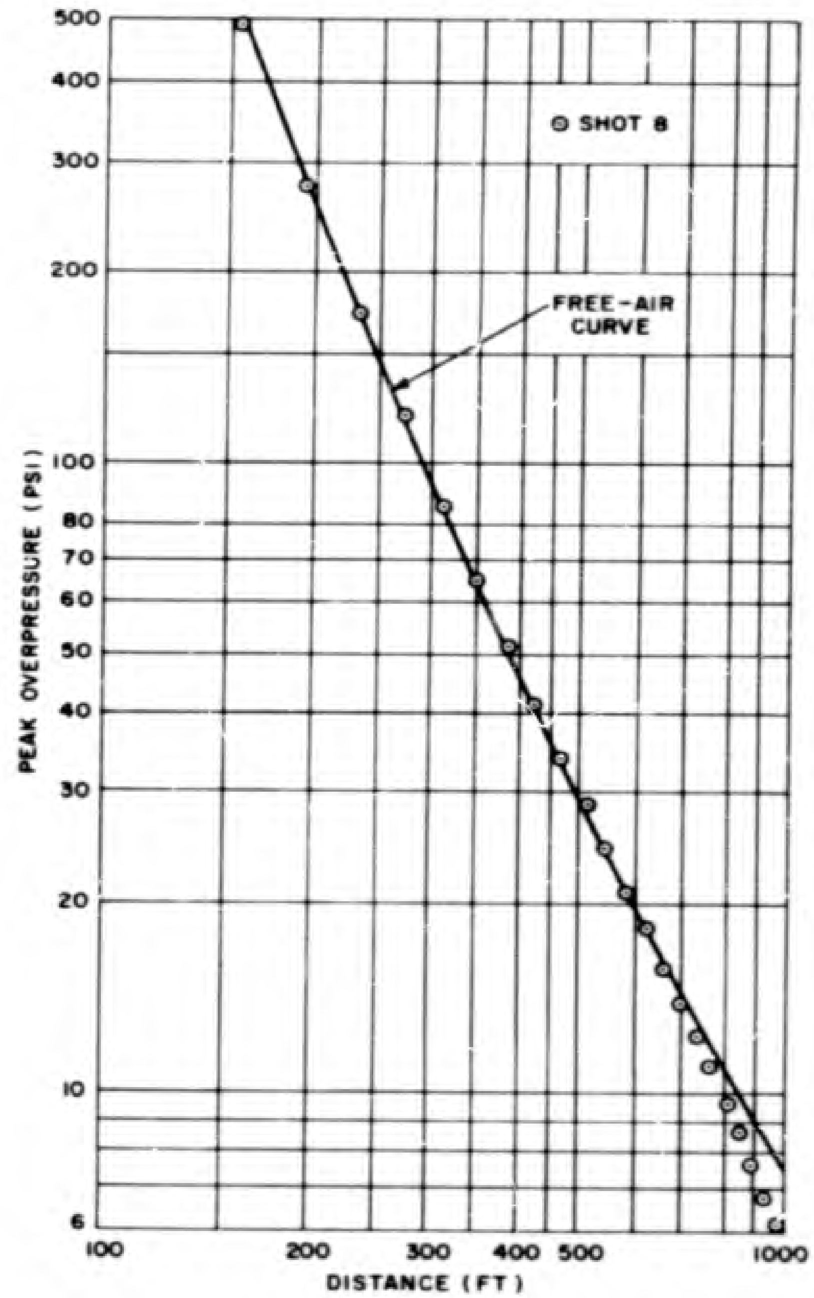

Figure 4.2 Shot 8, Pressure versus Distance Reduced to 1 KT (RC) at Sea Level.

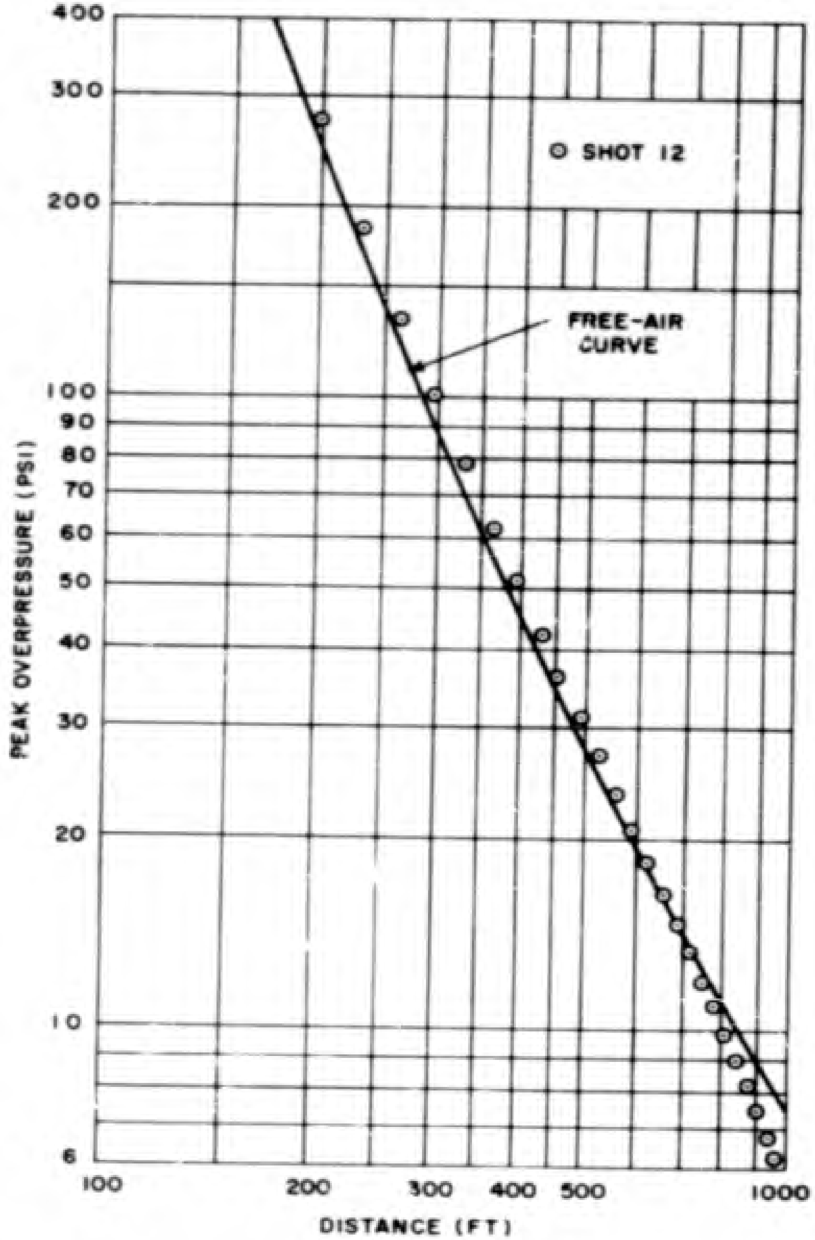

Figure 4.3 Shot 12, Pressure versus Distance Reduced to 1 KT (RC) at Sea Level.

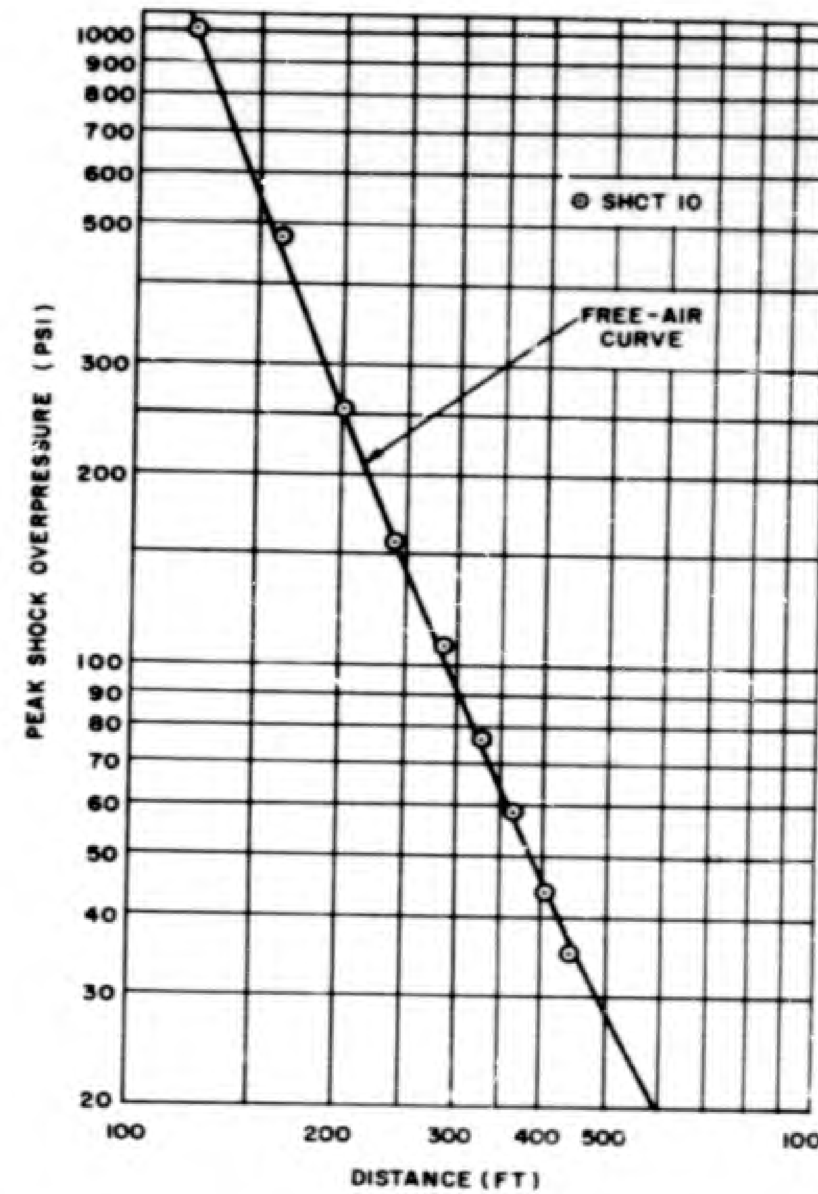

Figure 4.4 Shot 10, Pressure versus Distance Reduced to 1 KT (RC) at Sea Level.

shock wave coalescence is involved cannot be answered with certainty. Whether it can be attributed to some form of "mass effect"* is equally uncertain. Whatever the reasons, it is believed that the pressure anomalies observed are real and are not introduced through a quirk in the mathematics employed. Further investigation is obviously warranted.

4.1.4 High-Altitude Scaling Effects

The pressure-distance data obtained by Projects 1.1 (AFCRC) and 1.2 (NOL) on the high-altitude shot, Shot 10, are in good agreement (see Fig. 3.33). The NOL data have been scaled to 1 KT (RC) at sea level by the Sachs scaling technique (see Table 1.1 for the scaling factors) and are presented in Table 4.4. Figure 4.4 shows a comparison of the scaled Shot 10 data with the composite free-air curve (Reference 6). The good agreement noted in this figure appears to indicate that the useful range over which Sachs scaling techniques are applicable may be extended to at least 36,600 ft MSL with reliability. This result lends strong support to the blast prognostications of Shelton, Reference 14, who predicted that Sachs scaling techniques would be applicable under the Shot 10 burst conditions to within an accuracy of a few percent. This would imply that essentially the same distribution of energy among the forms of blast, thermal radiation, and nuclear radiation would hold for bursts at altitudes of the order of 35,000 ft MSL as for those at much lower altitudes. The small deviations from the composite curve at the data extremes, Fig. 4.4, do not exceed 6 percent, which is well within the experimental error of 10 percent assigned to the data. Thus the data do not provide a rigorous proof of Shelton's arguments, but they do appear to uphold them to a reasonable extent.

Somewhat contrary to these results, it is worth noting that a greater amount of energy in the form of thermal radiation escaped the fireball prior to shock breakaway on Shot 10 than on Shot 9**, the companion shot involving the burst of an identical weapon at about 5,000 ft MSL. Furthermore, the initial nuclear radiation, or more exactly - the normalized total gamma exposure, was about 50 percent greater (uncorrected) for Shot 10 than for Shot 9***. Both of these observations tend toward the

---

* The "mass effect" is an effect which has been recognized to account for variations observed in the rate of growth of the shock wave early in the history of a nuclear explosion, chiefly during the fireball phase. These variations are observed when large masses of metal and other materials are present in the vicinity of the exploding bomb. In certain respects it can be likened to the "case effect" in HE explosions. One of the predominant features of such explosions is that they produce higher-than-average pressures at larger distances as compared to bare-charge explosions.

** Deduced from preliminary information reported in Reference 15.

*** Stated in Reference 15.

same conclusion, namely, that less energy was available during the period of shock formation and development on Shot 10 than on Shot 9.

In view of the good agreement between the scaled blast pressure-distance measurements and the composite free-air curve it can only be said that if the partition of energy on Shot 10 was different, the difference was less than a few percent. If the available energy on Shot 10 were much less than that for lower burst heights, it would have produced noticeably lower pressures at the larger distances. Since such low pressures were not observed, it can only be concluded that energy losses to the shock were small and that the distribution of energy was about the same as for bursts of lower altitudes.

4.2 SURFACE PHENOMENA

4.2.1 Thermal Effect on Mach-Stem Growth

It was noted in References 4 and 6 that the existence of the thermal layer near the surface affected the normal point of inception and subsequent growth of the Mach stem, and hence, the trajectory of the triple point. On Shot 9 of Operation UPSHOT-KNOTHOLE (Reference 6) the Mach stem became established at a closer distance to ground zero than would have been predicted, assuming the absence of a thermal layer. Reference 6 also suggested that whenever a precursor formed, a "thermal Mach" wave was produced prior to formation of the precursor.

On each of the shots of Operation TEAPOT for which triple-point (Mach stem height) data were obtained (Shots 4, 6, 8, and 12), precursors were observed and the effect on the early growth of the Mach stem was again observed as on previous tests. Particular attention was given to the data obtained over the three areas, water, asphalt, and desert, on Shot 12, where considerable differences in the triple-point trajectories were observed (see Fig. 3.47).

The rate of growth of the Mach stem over the asphalt area was much more rapid than over the other two areas, and the rate of growth over the desert was faster than that over the water. The maximum heights of the precursors observed over these areas followed the same relative pattern. Since the shock wave reflection coefficients for these three surfaces are but slightly different, it is believed that the radical differences in the precursors and triple-point trajectories resulted directly and solely from the differences in the corresponding thermal layers. Some laboratory work done at NOL which supports this contention is given in Reference 12. The rapid formation of a thermal Mach wave in the presence of a thermal layer and the subsequent smoothing out of the path of the triple-point above the layer is clearly demonstrated.

To the observed data for Shot 12 shown in Fig. 3.47 there has been added the semi-empirical, "ideal" path of the triple-point based on the method derived by Hesse and Kelso (Reference 16). As can be seen in the figure, the "desert" data fit this curve best. Most of the data used in the construction of the "ideal" curve were obtained over desert surfaces and the agreement noted in Fig. 3.47 is deemed significant. However, Reference 16 states that the ideal prediction curves exclude thermal effects. It would appear from Fig. 3.47 that such is not strictly the case inasmuch as the Mach stem over the water surface, for which thermal effects were minimal, rose less rapidly than when strong thermal effects prevailed.

Prior to TEAPOT, a precursor had never been observed over a water surface, so this surface was considered to be "ideal", i.e., since precursors were not observed it was assumed that a thermal layer did not

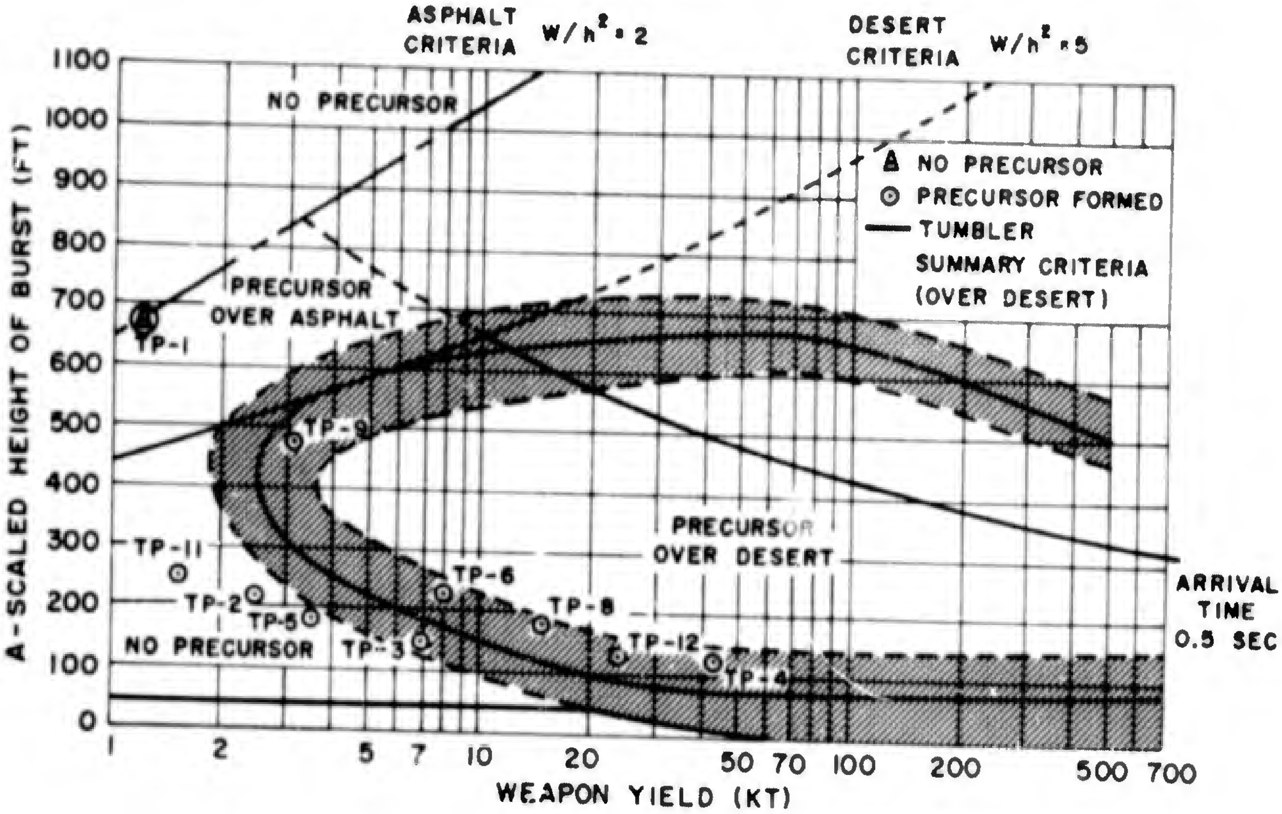

Figure 4.5 TEAPOT Shots Plotted on Precursor Chart from Reference 24.

form over a water surface and therefore did not give rise to the formation of nonideal shock phenomena. Now a precursor was not observed to form over the water surface on Shot 12 (as will be discussed further in Section 4.2.2), so the path of the triple point over this surface might well be considered to be more nearly that for the "ideal" case than that observed over the desert surface.

Since strong precursor and thermal Mach effects were observed over both the asphalt and desert surfaces and the calculated path of the triple point corresponds to that for the desert surface, it is suggested that thermal effects are included to at least a small extent in the rather elegant Hesse-Kelso prediction method for the height of the Mach wave.

4.2.2 Precursor Formation over the Water Area on Shot 12

The question of whether a precursor formed over the water surface on Shot 12 or was simply the result of feed-in effects cannot be fully resolved from the film records obtained for Project 1.2. The aerial films were particularly disappointing, having been obtained from an aircraft located in the wrong quadrant to show the desired detail.

The net results of an examination of (1) the arrival-time data of SRI, Project 1.10, and similar NOL data, Project 1.12; (2) the pressure-time data of BRL, Project 1.14b; (3) the flow-direction data of WADC, Project 5.5; and (4) the triple-point-trajectory data of this project, Project 1.2, lead to the conclusion that the precursor effects observed over the water area were predominantly the result of feed-in from the adjacent desert areas.

It should in no way be inferred from this conclusion that the blast wave over this area was ideal, for it will be noted, Reference 15, that water loading and associated nonideal dynamic pressures were observed. Rather, it is to be concluded on the basis of all available data, that a sufficiently intense thermal layer for precursor formation over the water area itself did not develop; the rounded pressure waveforms resulted from feed-in effects and water-loading of the shock presumably would have occurred even if the water area had been of infinite extent.

4.2.3 Precursor Criteria

Of the several shots chosen for precursor studies by direct shock photography, Shots 1, 3, 4, 6, 8, 9, and 12, the ones which shed the most light on existing precursor criteria were Shots 1, 2, 5, 6, 11, and 12. Photographic records were not obtained specifically for Project 1.2 on Shots 2, 5, and 11, but it was ascertained that precursors were formed by examination of the cloud study films of Project 9.4 and the pressure-time records of Project 1.14b.

Figure 4.5 shows the superposition of two charts used for predicting precursors. (These two charts were first presented in this manner for purposes of comparison in Reference 24.) The shaded portion of the chart represents the prediction criterion proposed by Shelton (Reference 17) and was derived from empirical information and a theoretical analysis. According to this prediction method only those shots falling in the shaded area should produce a precursor. The AFSWP-NOL precursor-prediction scheme, developed shortly after Operation TUMBLER, (References 18 and 19), is the entire area bounded by the lines representing: (1) $W/h^2 = 5$ (W is the yield in KT and h is the actual height of burst in thousands of feet); (2) shock arrival time at ground zero = 0.5 sec; and (3) A-scaled height of burst = 50 ft for yields up to 20 kt. TEAPOT Shots 1 through 12, Shots 7 and 10 excepted, have been spotted in Fig. 4.5 for comparison.

As noted above, precursors were observed on Shots 2, 5, and 11, in keeping with the AFSWP-NOL prediction, whereas all the other

[redacted]

precursor-producing shots were covered by both methods, with one significant omission. Neither chart predicted the precursor which was observed to occur during Shot 1.

Shot 1, a relatively high burst of a low-yield device, produced a very weak precursor over an asphalt area in the vicinity to one side of ground zero (see Fig. 3.3). On the other side of ground zero, over the desert surface, no precursor was observed. On Shots 6 and 12, where asphalt surfaces were also involved, much larger precursors were observed over the asphalt than over the desert area. Presumably, a smaller thermal input is required over a more-absorbing surface, such as asphalt, than over the more-reflecting desert surface to produce a sufficiently intense thermal layer for precursor formation.

Based on this information an extension of the AFSWP-NOL chart has been made. Since the Shot 1 precursor over the asphalt was so weak, it is considered reasonable to use this point as a lower limit on the prediction chart, for it corresponds to minimum-energy-input conditions over a highly absorbing surface capable of causing the formation of a sufficiently intense thermal layer for precursor development. Thus it is proposed that the area bounded by lines representing $W/h^2 = 2$ and shock-arrival time = 0.5 sec be added to the AFSWP-NOL chart as in Fig. 4.5 to take into account the relative thermal absorptivities of various solid surfaces.

4.2.4 Temperature Calculations from Shock Contours

Calculations of the temperatures in the thermal layer, based on the angle of the precursor front, are generally high when compared to actual thermal and sonic speed measurements (References 20 and 21). These calculations are based on the equation (Reference 6):

$$\sin \theta = \frac{c_1}{c_2} \tag{4.1}$$

where θ is the angle between the precursor front and the surface and c_1 and c_2 are the ambient sonic speeds of the unheated and heated regions, respectively.

However, this pre-supposes that the thermal layer contains no temperature gradient with respect to height above the ground and that the transmitted wave front referred to as the thermal Mach in Reference 6 is propagated normal to the boundary separating the heated and unheated regions. This is probably not the case, since it is thought that the thermal layer contains a fairly large gradient in temperature. Thus the transmitted wave front should not remain normal to this boundary, but should form an acute angle with it. Therefore, when the transmitted wave propagates across the boundary, it should be refracted; and if one measures the angle of this refracted front and applies Equation 4.1, then the temperatures calculated would be in error.

[redacted]

If the acute angle that the transmitted wave front makes with the boundary is called ϕ and the acute angle that the precursor front makes with the boundary is called θ and all other assumptions listed in Reference 6 are the same, then application of Snell's law across the boundary gives:

$$\frac{U_2}{\sin \phi} = \frac{U_1}{\sin \theta} \tag{4.2}$$

where U_2 is the velocity of the transmitted wave in the heated region and U_1 is the velocity of the precursor front in the unheated region.

TABLE 4.5 - Shot 6 - Temperature Calculations Using the Angle of the Precursor Front

Ground Range (ft)	θ (degrees)	ϕ (degrees)	Calculations made using Eq. 4.1		Calculations made using Eq. 4.4	
			Temp. (°C)	Sound Vel. (ft/sec)	Temp. (°C)	Sound Vel. (ft/sec)
		ASPHALT SURFACE				
532	13.4	24.3	4829	4699	591	1934
777	19.4	33.0	2211	3278	463	1785
969	21.2	37.5	1822	3011	503	1833
1,108	26.4	42.6	1113	2449	361	1658
		DESERT SURFACE				
551	17.8	22.7	2659	3562	163	1377
733	25.8	33.6	1173	2502	170	1387
901	28.1	34.3	962	2312	119	1304
1,044	31.5	41.3	731	2084	164	1378

Also from Reference 6 we have

$$\frac{U_1}{c_1} = \frac{U_2}{c_2}\,. \tag{4.3}$$

Therefore,

$$\frac{\sin \theta}{\sin \phi} = \frac{c_1}{c_2}\,. \tag{4.4}$$

It is evident that Equation 4.4 will lead to lower calculated temperatures provided $\theta < \phi$.

On Shot 6 this difference in the angles θ and ϕ could be observed to some extent. However, the height of the thermal layer was observed to be from 3 to 5 ft, which made it difficult to detect the change in angle. For this reason, the data in support of the argument are not conclusive. Temperatures calculated by the use of Equation 4.4 over both the asphalt and desert surfaces were obtained at several distances. Table 4.5 presents the measured angles θ and ϕ and the temperatures calculated by both Equations 4.1 and 4.4. Also listed in Table 4.5 are the sound speeds of the thermal layer calculated from Equations 4.1 and 4.4.

Unfortunately, these data cannot be compared directly with any measured data. The results of Project 8.4e (Reference 21) and 1.5 (Reference 20) on Shot 12 are inconclusive at this time. Therefore, it is impossible to conclude that Equation 4.4 would lead to the proper temperature calculations because of the lack of actual temperature data, the limited amount of θ and ϕ data, and the relatively poor accuracy of these angle measurements. However, it is suggested that the large differences observed between the shock-calculated and indirectly measured temperatures on Shot 12 may be at least partially accounted for by this argument.

Chapter 5
CONCLUSIONS and RECOMMENDATIONS

5.1 INSTRUMENTATION

The rocket-smoke-grid instrumentation used on Shots 4, 8, and 12 operated successfully and made possible the detection of the locus of the incident and reflected shock waves in free air and the shock phenomena along the surface. On Shot 12 the grid was of particular value in facilitating the measurement of the precursor where it was difficult to distinguish it from the dust front. The criss-cross grid form, used for the first time on this operation, was found more useful than the vertical or fan grid form used on previous tests in the close inspection of that area directly above the burst.

The smoke grid produced by jet aircraft on Shot 10, including one B-47 guide plane and seven jet-fighter craft of the F-84, F-86 class, was of little or no value for the purposes of the project. Their use in any future high-altitude test is not recommended unless significant improvements can be made. Fin-stabilized rockets of the Deacon variety, launched from aircraft suitably spaced, would appear to be more feasible according to present thinking.

The photographic instrumentation for smoke-grid and direct shock photography was operated in excellent fashion and produced useful and reliable data. This technique is recommended for use in future tests where free air peak pressures, incident- and reflected-wave-coalescence studies, and surface shock-precursor phenomena observations are desired.

5.2 PRESSURE VERSUS DISTANCE IN AIR

Peak shock overpressure versus distance vertically above the burst was obtained on Shots 4, 8, and 12. On Shots 4 and 12, one of the primary objectives of the project was met in determining the value of the peak pressure subsequent to coalescence of the incident and reflected shock waves. On Shot 4, the pressure was apparently increased following coalescence at 2,550 ft (12-psi level), while on Shot 12 no pressure enhancement was detected when coalescence occurred at 2,600 ft (7-psi level). It must be concluded that, when the reflected shock traverses the fireball region, it encounters conditions which cause its velocity to increase greatly and its pressure and associated mass motion to decrease markedly. Its ability to "shock-up" beyond this region appears to depend critically on the extent of pressure attenuation experienced and the ambient conditions of the medium into which it propagates. All of these factors depend predominantly on yield and

[redacted]

height of burst, the more extreme conditions resulting from large yield and low burst heights, mainly tower shot conditions.

When these observations are correlated with measurements made on previous tower shots wherein pressures have been found to deviate from the standard composite free-air curve (which is based solely on air-drop data), it is suggested that these deviations may have resulted from reflected shock coalescence with the incident wave, accompanied by pressure enhancement or deterioration. For military purposes the standard composite free-air curve, as published in Reference 6, should not be altered in any respect as a result of new information gained on this operation; however, it is recommended that in a handbook such as the "Capabilities of Atomic Weapons", Reference 25, it should be pointed out that pressure enhancement or deterioration may occur directly above the burst of medium to large-yield weapons detonated near the surface. Further investigation of the problem is required before more-specific information can be given.

For weapons burst at altitudes up to approximately 40,000 ft MSL, Sachs scaling of shock pressures has been found to be reasonably justified. Shock pressures of from 8 to 800 psi determined on Shot 10 scale well with the standard composite free-air curve. A small uncertainty in the use of the Sachs scaling may be said to exist at the upper extremes of this 40,000 ft range, however, because of the peculiarities observed in connection with the comparative thermal and nuclear measurements of Shots 9 and 10 (see Section 4.1.4).

Further attempts to modify the fitting function employed in the determination of pressure versus distance from shock-arrival-time data should be made in an effort to obtain an equation which will fit the data and, at the same time, contain constants which can be interpreted in the light of prevailing ambient conditions

Unexpectedly high blast effects along the surface were measured on Shot 7, the underground shot, and no attempt was made to instrument the test to obtain airblast-pressure-distance measurements. An effort will be made to obtain such information from existing films, but it is questionable whether such data will be sufficient to establish blast prediction criteria for underground bursts. Such data are considered to be vital from the standpoint of safety in weapon delivery, and where high accuracy is demanded. It is recommended that free-air pressures be obtained on any future underground burst until such criteria are established or the proposed delivery procedures are modified significantly in this respect.

5.3 COALESCENCE OF THE INCIDENT AND REFLECTED SHOCK WAVES

The requirements of Project 5.1 (Destructive Loads on Aircraft in Flight) included the ascertainment of whether coalescence of the incident and reflected shock waves could be expected on Shot 12 and a prediction of the pressure in the coalesced shock. The information provided Project 5.1 by Project 1.2 was based solely on the results of

Shot 4 and some rather incomplete but indicative data obtained during Operation UPSHOT-KNOTHOLE. Shot 8 was instrumented to obtain additional data, but the unexpectedly low yield of the device defeated this attempt. On the strength of the Shot 4 results principally, coalescence was predicted for Shot 12 and an increase in pressure equivalent to a yield of 1.2 times the expected yield of Shot 12 was predicted. Coalescence was observed on Shot 12 but no pressure enhancement was detected. All that can be said generally and with reasonable certainty is that coalescence occurs under suitable conditions of yield and burst height and that it is reasonably extensive, the horizontal radius of the coalesced wave being equal roughly to 1 to 2 fireball radii. Pressed for an opinion as to whether pressure enhancement would or would not occur upon coalescence on a given shot, the reply would be affirmative only if the fireball were expected to intersect the ground, such as on Shot 4. On the basis of existing knowledge, it would be impossible to estimate the magnitude of the pressure difference in terms of an "equivalent weight" of charge.

5.4 PRECURSORS

A more-extensive and faster precursor wave will form over a black-asphalt (thermally absorbing) surface than over a desert (thermally reflecting) surface. Over a water surface it is believed that a precursor will not form. The precursor-like effects observed over the water surface on Shot 12 are believed to have resulted solely from feed-in from adjacent areas.

Although it is believed that a precursor will not form over water, a natural water surface should not be considered as "ideal" from the standpoint of blast effects along the surface. Knowledge gained during Operations CASTLE and TEAPOT indicates that water-loading of the blast wave will occur, leading to nonideal values of dynamic pressure and other parameters.

When thermal layers are produced over surfaces conducive to precursor formation, the Mach shock will form earlier and grow at a more-rapid rate to the height of the thermal layer than when no thermal layer is present. The triple point will remain at a more or less constant height above the ground (height of the thermal layer) until it reaches the range at which it would normally be expected rise above that elevation in the absence of a thermal layer. From that position onward, the triple point resumes its normal course and can be predicted with sufficient accuracy (± 10 percent) for military purposes.

The AFSWP-NOL precursor-prediction criteria should be adopted for general use with the addition of the new limit described (Section 4.2.3) to take into account the relative thermal absorptivities of various surfaces.

A change in the method of calculating gross temperatures from the angle made by the precursor front with the ground may be warranted. The change in the theory, based on the recognition of the existence of a temperature gradient n the thermal layer, would lead to lower calculated temperatures more in agreement with temperatures actually recorded, both directly and indirectly. At present there are insuffient data upon which to reach a sound decision in this regard. Since this problem seems to be primarily of academic interest, it is recommended that suitable decisive data be obtained only as a possible bonus from future atomic test data.

UNCLASSIFIED

[redacted]

REFERENCES

1. Moulton and Simonds, Peak Pressure vs Distance in the Free-Air and Mach Regions Using Smoke-Rocket Photography, Operation GREENHOUSE, WT-54, July 1951, SRD.

2. Hartmann, Lampson and Aronson, Blast Measurements Summary Report, Operation GREENHOUSE, WT-64, May 1952, SRD.

3. Moulton, Walthall and Hanlon, Peak Pressure vs Distance in Free-Air Using Smoke-Rocket Photography, Operation JANGLE, WT-389, June 1952, SRD.

4. Aronson, et al, Free-Air and Ground Level Pressure Measurements, Operation TUMBLER, WT-513, November 1952, SRD.

5. Moulton and Hanlon, Peak Overpressure vs Distance in Free-Air, Operation IVY, WT-613, March 1953, SRD.

6. Morris, et al, Air Blast Measurements, Operation UPSHOT-KNOTHOLE, WT-710, August 1955, SRD.

7. Hanlon, et al, Blast Pressures and Shock Phenomena Measurements by Photography, Operation CASTLE, WT-902, September 1955, SRD.

8. Milligan and Young, Operation TEAPOT - Underground Shot - Base Surge Analysis, AFSWP-876 (NAVORD 4153), 31 January 1956, SRD.

9. Hirschfelder and Curtiss, Thermodynamic Properties of Air, Vol. II, University of Wisconsin (NRL), 2 December 1948, Unclassified.

10. Rudlin, Notes on the Variation of the Mach Number - Shock Strength Relation with Ambient Conditions, NAVORD 4029, 1955, Unclassified.

11. Griffith and Bleakney, Diffusion Analogy for Shocks Interacting with Thermal Boundary Layers, Abstract of Fluid Dynamics, American Physical Society and paper presented at meeting of 22-24 November 1954. To be published in Journal of Aero. Sci., Unclassified.

12. Varwig and Zemel, The Interaction of Shock Waves with a Thermal Layer, NAVORD 4021 (AFSWP-266), 18 July 1955, Unclassified.

13. Richardson, Fireball Radii and Height of Burst, SC-3627(TR), 16 August 1955, SRD.

14. Shelton, Phenomenology of a High-Altitude Atomic Explosion, SC-3363(TR), 28 April 1954, SRD.

[redacted]

15. Doll and Gilbert, Preliminary Report - Summary Report of the Technical Director, Programs 1-9, Operation TEAPOT, ITR-1153, June 1955, SRD.

16. Hesse and Kelso, Mach Shock Formation from a Nuclear Detonation, AFSWP-510, 10 March 1955, SRD.

17. Shelton, The Precursor - Its Formation, Prediction and Effects, SC-2850(TR), 27 July 1953, SRD.

18. Aronson, Moulton, Hartmann and McClendon, NOL Reports Presented at TUMBLER Symposium, NAVORD 2801, 16 April 1953, SRD.

19. Scoville, et al, Final Summary Report - Operation TUMBLER, WT-514, May 1953, SRD.

20. McLoughlin, Preshock Sound Velocities Near the Ground in the Vicinity of an Atomic Explosion, Operation TEAPOT, ITR-1104, May 1955, CRD.

21. Inn, Air Temperature Measurements Over Several Surfaces, Operation TEAPOT, ITR-1149, May 1955, CRD.

22. Bartalsky, Airborne Smoke Trail Generators, AFSWC-TN-55-12, 15 September 1955, Unclassified.

23. Private communication to authors from Dr. N. A. Haskell, Project Officer, Project 1.1, Operation TEAPOT, of 18 August 1955, SRD.

24. Doll, et al, Summary Report of the Technical Director - Operation UPSHOT-KNOTHOLE, WT-782, March 1955, SRD.

25. Capabilities of Atomic Weapons, prepared by the Armed Forces Special Weapons Project, TM 23-200, 1 June 1955, SRD.

UNCLASSIFIED

BLANK PAGE